Spring 2017

Mold flux crystallization and mold thermal behavior

Elizabeth Irene Peterson

Department:

MOLD FLUX CRYSTALLIZATION AND MOLD THERMAL BEHAVIOR

by

ELIZABETH IRENE PETERSON

A THESIS

Presented to the Faculty of the Graduate School of the

MISSOURI UNIVERSITY OF SCIENCE AND TECHNOLOGY

In Partial Fulfillment of the Requirements for the Degree

MASTER OF SCIENCE IN MATERIALS SCIENCE AND ENGINEERING

2017

Approved by

Ronald J. O'Malley, Advisor
Jeffrey D. Smith, Co-advisor
Richard K. Brow

PUBLICATION THESIS OPTION

This thesis consists of the following two articles, formatted in the style used by Missouri University of Science and Technology:

Paper I: Pages 52-62 have been accepted by and presented at the 10th International Conference on Molten Slags, Salts, and Fluxes in Seattle Washington, May 2016.

Paper II: Pages 63-81 were submitted to and accepted for presentation at AISTech in May 2017.

ABSTRACT

Mold flux plays a small but critical role in the continuous casting of steel. The carbon-coated powder is added at the top of the water-cooled copper mold, over time it melts and infiltrates the gap between the copper mold and the solidifying steel strand. Mold powders serve five primary functions: (1) chemical insulation, (2) thermal insulation, (3) lubrication between the steel strand and mold, (4) absorption of inclusions, and (5) promotion of even heat flux. All five functions are critical to slab casting, but surface defect prevention is primarily controlled through even heat flux. Glassy fluxes have high heat transfer and result in a thicker steel shell. Steels with large volumetric shrinkage on cooling must have a crystalline flux to reduce the radiative heat transfer and avoid the formation of cracks in the shell. Crystallinity plays a critical role in steel shell formation, therefore it is important to study the thermal conditions that promote each phase and its morphology.

Laboratory tests were performed to generate continuous cooling transformation (CCT) and time-temperature-transformation (TTT) diagrams. Continuous cooling transformation tests were performed in an instrumented eight cell step chill mold. Results showed that cuspidine was the only phase formed in conventional fluxes and all observed structures were dendritic. An isothermal tin bath quench method was also developed to isothermally age glassy samples. Isothermal tests yielded different microstructures and different phases than those observed by continuous cooling. Comparison of aged tests with industrial flux films indicates similar faceted structures along the mold wall, suggesting that mold flux first solidifies as a glass along the mold wall, but the elevated temperature devitrifies the glassy structure forming crystals that cannot form by continuous cooling.

ACKNOWLEDGEMENTS

I would first like to thank my advisors Dr. O'Malley and Dr. Smith for their technical advice and guidance. I would also like to acknowledge the member companies of the Peaslee Steel Manufacturing Research Center (PSMRC) for funding this project. I would also like to extend my gratitude to the members of my industrial mentoring committee for their time, suggestions, and encouragement. I would especially like to thank Marc McClymonds, Steve Jauch, Darrell Sturgill, Sunday Abraham, Xiaoxu Zhou, and Bill Long for their personal support of this project. I would also like to thank my final committee member Dr. Brow for his time.

I am deeply indebted to Todd Sander for his expertise and encouragement through all aspects of this project. My appreciation also extends to the entirety of the MSE department especially Teneke Hill, Dr. Mary Reidmeyer, Dr. Eric Bohannan, Dr. Clarissa Wisner, Dr. JingJing Qing, Denise Eddings, Nicole Sikes, and Emily Dake. Also my co-graduate students who have helped me through this journey, especially Obinna Adaba, Andrew Russo, Dan Field, Parker Freudenburger, Eric Muskovin, Ryan Grohsmeyer, and Anna Mattione.

I am very thankful for the outstanding group of undergraduate students that helped throughout this project. Cassie Seamen, Kenneth Andrew Domann, Steven Ross, Griffin Johnson, Thairo Rangel Mafia, Travis Stuart, Evan Musterman, Chase Davis, Ransom Stamps, Andrew Artzer, Nicholas Anselmo, Logan Huddleston and Ashley Reisig, thank you. I couldn't have done it without your help.

Last but not least, I need to thank all those who helped me keep my sanity, enthusiasm, and a (mostly) positive attitude. My parents, Sue and Paul, who always made time for my frantic phone calls and always encouraged me to keep going. My sisters, Hannah and Paula, who keep me grounded and always make me smile. My friend Donna who keeps me laughing. Finally, a huge thank you to my husband, Daniel, for putting up with me, supporting me, and always believing in me.

TABLE OF CONTENTS

LIST OF ILLUSTRATIONS

LIST OF TABLES

1. INTRODUCTION

1.1. OVERVIEW

Mold flux is a carbon-coated, often spray dried, powder that is used in the continuous casting of steel. It serves five primary functions: (1) protect the steel from oxidation, (2) control heat removal and steel shell formation, (3) absorb inclusions, (4) lubricate the steel as it is drawn out of the mold, and (5) thermally insulate the steel. It is imperative to identify the proper mold flux for casting each steel grade as the powder regulates steel shell formation by controlling the heat transfer from the strand to the mold. High heat transfer is associated with a glassy morphology and can lead to longitudinal cracking on the steel surface. [1] Fluxes with a high degree of crystallinity can be problematic if the steel shell is not strong enough at the mold exit to withstand the ferrostatic pressure of the molten steel within. Since the crystallinity and crystal morphology play a large role in the control of the heat transfer between the steel shell and the water-cooled copper mold, it is imperative to understand the thermal history required to create desired morphologies in the mold flux film.

The mold gap between the mold and the steel shell is only 1 to 4 mm thick, [2-3] but has a thermal gradient ranging from steelmaking temperatures (~1600°C) on the steel side to approximately 400°C on the mold side. High temperatures and corrosive materials make it difficult to directly measure what is occurring in the mold gap during casting. Instrumented molds can provide thermal profiles of the mold gap that clarify differences in heat removal from various locations in the mold, but they cannot define the temperatures at various distances from the mold wall. If flux film structures can be replicated in the laboratory, the thermal history that produces these crystals can be better understood.

Studies presented in this thesis target the relationship between the crystal morphology and thermal history. In this introduction, a brief summary of the continuous casting process will be presented, followed by a study of the current state of mold flux research focused on compositional effects, kinetics of crystallization, and methodologies for developing continuous cooling transformation (CCT) curves and time temperature transformation (TTT) diagrams.

1.2. CONTINUOUS CASTING [4-5]

Mold flux powder plays a small but critical role in the production of continuously cast steel. Steelmaking has been developing for centuries, but continuous casting has only been in practice since it was introduced in the 1950s. This process can be used to make billets, blooms, or slabs for subsequent processing in rolling mills. The use of the mold is somewhat analogous to extrusion in ceramics processing, where only materials with constant cross-section can be cast (typically rectangular). However it is different from most ceramic extrusion because it is a molten liquid casting process. The schematic drawing in Figure 1.1 shows the basic steel making process, starting with either producing pig iron in a blast furnace and then melting in a basic oxygen furnace (BOF) or melting scrap in an electric arc furnace (EAF). After melting the steel is alloyed and temperature is maintained in the ladle metallurgy furnace (LMF) and the continuous casting machine (CCM). The subsequent sections will provide an overview of the EAF steelmaking process from scrap to slab for the purpose of clarifying the role of mold flux.

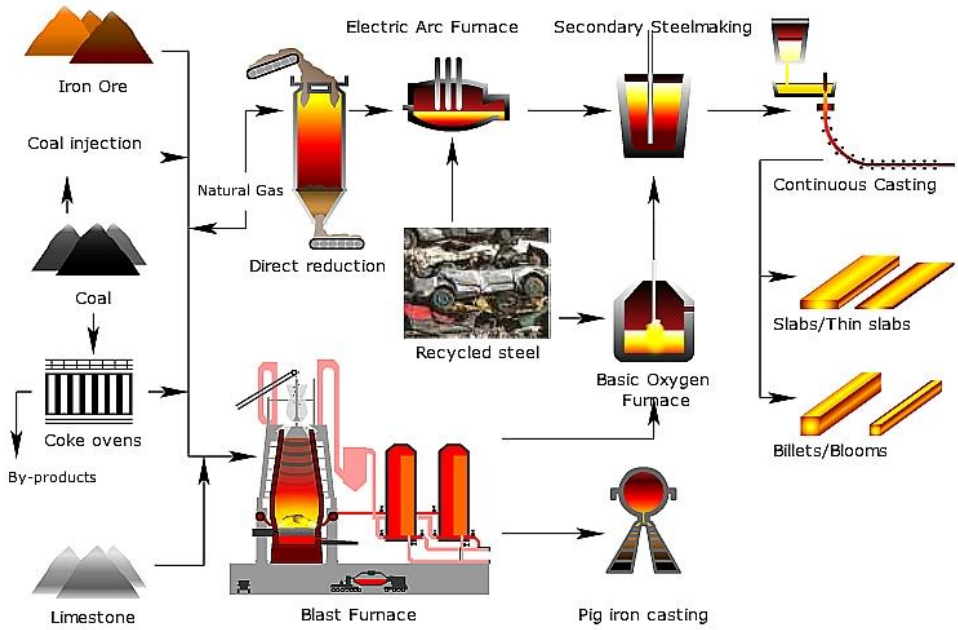

Figure 1.1: Overview of the steelmaking process starting from scrap steel. From [6].

1.2.1. Melt Shop. The steelmaking process begins in the melt shop. All steel plants employ a variation of two methods of melting: an electric arc furnace (EAF) or a basic oxygen furnace (BOF). The EAF steelmaking method is predominantly used in the United States today, however the BOF process has the highest global production. This section will focus on the EAF melting process. An electric arc furnace can use either AC or DC power. An AC furnace will have three electrodes that will lower down into the ladle once the scrap steel has been added. A DC furnace has a single graphite electrode and an anode that resides in the base of the furnace. This type of furnace requires a "hot heel," excess molten steel left in the furnace, to ensure intimate contact between the graphite electrode and the base anode and to increase the overall efficiency of the furnace. EAFs typically use a form of oxygen blowing in conjunction with the arc melting process. This helps remove carbon through gas evolution, as shown in Equations 1 and 2. Bracketed components are in the steel.

$$2[\mathrm{C}] + \mathrm{O}_{2\,(g)} \rightarrow 2\mathrm{CO}_{(g)} \quad (1)$$

$$[\mathrm{C}] + \mathrm{O}_{2\,(g)} \rightarrow 2\mathrm{CO}_{2\,(g)} \quad (2)$$

Oxygen and slag control are critical to generate a foamy slag, which protects the refractory, promotes phosphorus removal, and reduces iron oxide pickup into the slag. Eccentric bottom tapping (EBT) is commonly used for the EAF process to avoid slag carryover on tapping and decrease the reabsorption of nitrogen into the steel. The primary functions of the EAF are melting at steelmaking temperatures (~1600°C), carbon and phosphorous removal, and nitrogen control.

1.2.2. Ladle Metallurgy. Ladle metallurgy is a secondary refining process, post melting, that is used to achieve the target chemistry prior to casting. During this process the slag and steel are deoxidized to an acceptable oxygen content, typically by Al-killing or Si-killing the steel. Reduced oxygen content promotes desulphurization of the steel. The steel is typically alloyed to achieve the final desired chemistry. Other additions such as calcium may be made to modify inclusion chemistry and further desulphurize the steel by

the reaction shown as Equation 3. Bracketed terms still designate components in the steel. Parenthesized components are in the slag and bracketed components are in the steel.

$$2(\mathrm{CaO}) + 2[\mathrm{S}] \rightarrow 2(CaS) + [O_2] \quad (3)$$

Argon stirring is commonly employed to promote flotation of inclusions and homogenization of the steel. The ladle metallurgy step is critical for chemistry modification and attaining a target temperature for casting. It also can act as a buffer between the EAF and the caster which often run at different speeds.

1.2.3. Vacuum Treatment. Vacuum treatment is a process that has been developed to increase the cleanliness of the steel, which has become increasingly important for high-quality steel grades. This method is not employed for all steel grades and is not pictured in Figure 1.1. Vacuum methods may be employed for several purposes including: removal of dissolved gasses, decarburization, alloying, de-oxidation, and inclusion removal.

1.2.4. Tundish. Following the final refining step the ladle is brought to the tundish, which contains the steel between the ladle and the mold. Residence time in the tundish is increased so it can act as a reservoir during ladle changes; a critical aspect of continuous casting. The tundish is the final step in which inclusions can be removed prior to casting. Additionally steel composition and temperature must be controlled throughout this step to ensure proper casting. Modern tundishes employ several flow modifiers such as impact pads, weirs, dams or baffles to direct flow, promote inclusion removal, and to homogenize the melt. Steel is distributed from the tundish to the mold via a submerged entry nozzle (SEN). Many plants have a single tundish that distributes steel to multiple molds. It is increasingly important in these cases that the steel is homogeneous so the steel cast in each caster is identical.

1.2.5. Casting. Casting begins with the molten steel travelling from the tundish through the submerged entry nozzle (SEN) into a water-cooled copper mold. Molten steel is protected from oxidation by a thick layer of mold powder on top of the molten steel in the mold. The powder melts and infiltrates the gap between the molten steel and the mold. Heat transfer for steel shell solidification is controlled by the crystallization behavior of the mold flux.

Steel shrinkage during solidification is counteracted by tapering the mold. The mold oscillates at a fixed rate to prevent the steel shell from sticking and to pump molten flux down the mold gap for lubrication. [7, 8] Oscillation occurs in the casting direction with an amplitude less than 10 mm and a frequency range of 50 to 250 cycles per minute. [7] The mold oscillation is related to the casting speed by referring to the portion of the cycle when the mold moves downward at a speed greater than the casting speed as "negative strip." The complementary portion of the cycle is referred to as "positive strip." Negative strip time is necessary to compress and heal imperfections and strengthen the steel strand. Molten flux is also pumped further down the mold gap. However, if the negative strip time is too long, deep oscillation marks can form on the steel surface. Positive strip time helps distribute the liquid flux to the mold gap and promote flux consumption, which promotes uniform heat transfer. [7]

During casting, mold flux can be entrapped into the molten steel. This type of defect is associated with the flow patterns and may be caused by: 1) steel flow reversing from the narrow face of the mold, 2) the high shear stress that is associated with reversing flow, 3) the excessive velocity at the flux-metal interface, 4) entrapment from an argon bubble escaping the SEN ports and reaching the steel-mold powder interface, and 5) uneven flow on either side of the nozzle as depicted in Figure 1.2. [9] Water-model studies have been performed to understand the entrapment phenomena and to determine what parameters can be adjusted to minimize the formation of mold flux inclusions. [9-11] The water models were able to duplicate several of the suspected mechanisms and indicated the extent of entrapment as well as mold locations likely to experience these mechanisms.

Upon mold exit, the strand goes through a series of water sprays and support rollers to promote further solidification and control cooling. There are several caster configurations: vertical casters, bending casters with a straight mold, and bow-type casters with a curved mold. [5] Each process has advantages and disadvantages concerning bending, straightening, casting speed, inclusion removal, and strand length. Regardless, all casters must cool the strand and support the strand upon mold exit. This is typically done using a set of rollers that are aligned and tapered to compensate for shrinkage. Water

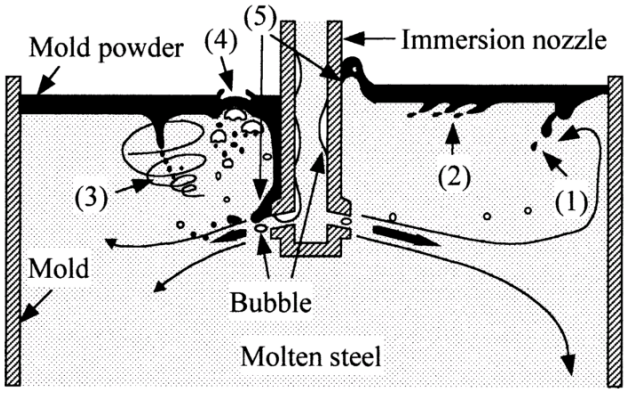

Figure 1.2: Schematic of methods of mold powder entrapment from [9]. Numbers correspond to the flux entrapment methods described previously.

nozzles or water-air nozzles are used to spray the steel shell surface to promote heat transfer through the slab and further cooling. The solidification rate of each steel grade must be controlled by modifying the water spray rate, and the casting speed. [5]

1.2.6. Mold Configurations and Properties. Conventional slab casters are typically rectangular with a taper towards the bottom of the mold to promote uniform shell formation during mold oscillation. A funnel-type mold may be used for thin slab-casting. These molds have a larger funnel opening at the top where liquid steel flows into the mold via the SEN. The bottom of a funnel mold is similar to a conventional mold because the sides become parallel again. Depending on mold sophistication, the taper of the mold can be adjusted prior to casting or in real-time. Molds are machined out of copper due to its high thermal conductivity (~402 W/mK at room temperature). [12] Often the hot face of the mold is coated in a sacrificial, 1-3mm thick, nickel coating to reduce wear. [13]

Many authors have modeled the thermal and mechanical behavior of conventional molds [13-14] as well as funnel molds [15-17]. These models are complex but still rely on assumptions to simplify the system for rapid computation. For example, mechanical models often ignore the nickel plating on the hot face because the layer is only a few millimeters thick. [13,17] Thermal models indicate that the highest temperature is found just below the meniscus, these temperatures can be problematic to the mechanical integrity of the mold because over time embrittlement, surface cracking, and crack propagation can occur on the copper surface. [16] After several cycles the hot face is machined to eliminate

the surface defects, which allows the mold to be reused. However the machining may have an effect on heat transfer through the mold as the water delivery mechanism is now closer to the hot face.

Trials of mechanically texturing the copper mold surface have been performed in an attempt to reduce mold flux heat density without worsening lubrication. [18] Results from the work of Cho and Jeong indicate that flux thickness, including liquid, decreased overall with the texturing method. Many more studies are still necessary to optimize the mold set up and reduce mold variability.

1.3. MOLD FLUX: STRUCTURE AND PROPERTIES

This section will overview the effect of different oxide additions on the overall glass network and the critical properties of mold flux.

1.3.1. Glass Structure. [19] Mold powders form both glassy and crystallized phases, thus it is important to understand the structure and the formation of each. Glass structure will be discussed in this section. Nucleation and growth phenomena of the crystallized phases will be discussed later in the kinetics section. Mold powders initially form glasses, which unlike crystalline materials (Figure 1.3a) have no long range order. Even though the same repeating units are present in a glass, a non-repeating network is formed (Figure 1.3b). Mold powders tend to have a high fraction of glass formers usually in the form of SiO_2 and sometimes B_2O_3. Glass formers follow an empirical set of rules determined by Zachariasen: (1) Each oxygen should be coordinated with no more than two metal atoms, (2) The metal atoms should have small coordination numbers, (3) oxygen polyhedral share corners, not edges or faces, and (4) Three or more corners of each polyhedral coordination unit must be shared in order to create a 3D network. [20] Silica prefers tetrahedral bonding. This makes silica a good glass former because the Si-O-Si bonds between tetrahedra are able to have various bonding angles. Most mold fluxes contain 25-40 wt% silica.

A large number of constituents that are added to mold powders are “modifiers.” These oxides modify the existing silica network by breaking bonds and neutralizing charges. Modifiers determine the number of non-bridging oxygen atoms (NBOs) that form in silicate tetrahedra. In a silicate glass with no modifiers, all tetrahedra have zero NBOs.

As the concentration of modifying oxides increases, the number of NBOs per tetrahedra will increase, indicating a more broken network. This structural change directly affects the properties of the glass. For example an increase in the number of NBOs will decrease the polymerization of the network and decrease the viscosity. The valence state of the modifier can also affect the viscosity. Cations such as calcium with a +2 valence state have a higher field strength than sodium ions with a +1 valence state. The increased field strength of alkaline earth oxides results in a stronger bond with the silicate network. This ultimately leads to increased viscosity relative to adding the same amount of alkali oxide.

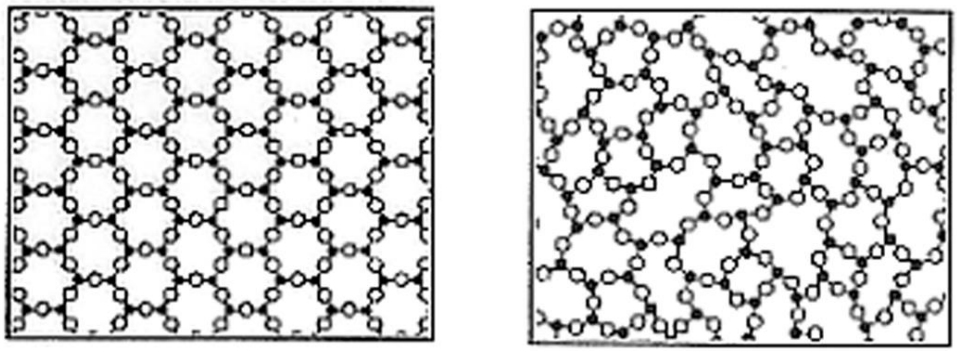

(a) (b)

Figure 1.3: Atomistic schematic of (a) crystalline material and (b) glassy material. From [21].

The basic glass model does fairly well at explaining additions of oxides and their effect on glass structure. However, it does not account for the addition of oxide modifiers beyond complete network depolymerization, nor does it explain the effect of CaF_2 additions. Several studies have been performed on SiO_2-CaO glasses with addition of oxide modifier (Na_2O [22], Li_2O [22], MgO [23], MnO [24]) and increasing amounts of CaF_2 to understand the effect of fluorine on the glass structure. As expected, the results vary depending on the base structure of the glass. Park et al. [23] found that increasing CaF_2 content reduced the crystallization temperature. Additionally IR spectra indicate that the number of bands with low [NBO]/Si decreased and bands with high [NBO]/Si increased with addition of CaF_2, which indicates that CaF_2 acts like a modifier. Other experiments

corroborate these results and further suggest that the effect of CaF_2 lessens after a critical amount has been added. [22, 24] The critical amount of CaF_2 varies based on the basicity and other modifiers present in the system.

Alumina is a conditional glass former, which means that it is difficult to form a glass alone but it will form a glass when combined with other glass forming oxides (i.e. aluminosilicate, aluminoborate, and aluminophosphate glasses). In a modified silicate network, the addition of alumina decreases the number of NBOs and increases the network connectivity. With a fixed concentration of modifying cations, an ideal ratio exists between silica and alumina to get the desired increase in viscosity. If too much alumina is added, there will not be enough cations to balance the lower valence state of the alumina ion. Ideally the ratio of alumina to silica is 1:1 with the exact amount of modifying oxides for a fully restored network, however research at Stanford has shown that perhaps NBOs still exist at this ratio. [25]

1.3.2. Composition. Conventional mold fluxes are composed of the same components (typical ranges shown in Table 1.1), but the relative amount of each varies depending on the desired properties. Properties considered are: viscosity, heat transfer, crystallization tendency, melting characteristics, and the effect of additions on structure. Effects of different element additions on the viscosity and crystallization tendency are detailed in 1.3.2.1 and 1.3.2.2 respectively. Heat transfer is outlined in section 1.3.3. Melting characteristics, including melt rate and the type of carbon used to coat the powder, are important for the prevention of steel oxidation and the continuous renewal of liquid flux in the mold. However, these topics but are not relevant to the central focus of this thesis and thus are excluded.

Table 1.1: Ranges of weight percentages of common oxides in conventional mold fluxes. The listed element denotes the oxide that is added (i.e. Al denotes Al_2O_3), except F which is typically added as CaF_2.

wt%	Ca	Si	Mg	Al	Mn	Na	F	Li	B	Zr	Ti	Basicity
Min	22	25	0	3	0	3	0	0	0	0	0	0.7
Max	44	45	14	22	3	16	11	5	2	2	< 1	1.3

1.3.2.1 Viscosity. Viscosity is critical because it is responsible for the flow characteristics and lubrication behavior of the mold powder. The viscosity is a direct measurement of the network polymerization of the silicate network; an increased fraction of NBOs results in a decreased viscosity. The most common methodology for measuring viscosity is the rotating spindle technique. [22-23, 26-28] This technique involves rotating a spindle in a crucible at constant speed and measuring the required torque. In all cases this measurement was executed at elevated temperature (1300-1500°C) to determine the effect of temperature on the viscosity of the specific molten flux. Viscosity at 1573K can vary from 0.5 dPas to 30dPas in high speed casting and billet casting respectively. [29] Several studies have been performed to understand the effect of different oxide additions on viscosity at different temperatures.

Increasing Na_2O content has been shown to depolymerize the silicate network by increasing the number of NBOs, which effectively lower the viscosity of melts of a variety of compositions. [30]. Li_2O, another alkali oxide, decreases the viscosity of the mold flux in additions up to 2 wt%. Work by Kim et al. has shown that additions exceeding 2 wt % have a dramatically reduced effect since other additions have already completely modified the existing silicate network. [22] The effect of CaF_2 is not as well understood as alkali metals in lime-alumino-silicate melts. Regardless, several studies have shown that increasing the CaF_2 content reduces the viscosity and the activation energy for viscous flow; the effect of each addition lessens the effect on viscosity. [22-24] The effect of CaF_2 on viscosity is more significant in a more basic system. [23]

TiO_2 is not commonly added to conventional mold powders, however during the casting of Ti-stabilized stainless steels, it often reduces silica in the glass by the reaction in Equation 4. Components in brackets are in the steel and parenthesized components are in the mold powder.

$$[Ti] + (SiO_2) \rightarrow [Si] + (TiO_2) \quad (4)$$

This exchange reaction can increase the TiO_2 content in conjunction with increasing the basicity of the mold flux. When TiO_2 replaces SiO_2 the viscosity has been shown to remain relatively constant at high temperatures (~1563-1623K) and increase viscosity at lower

temperatures. [26, 28] However without the Ti-Si exchange reaction, TiO_2 decreases viscosity. [28] Although rare earth oxide (RE) additions are uncommon, W. Deyong et al. have done some preliminary studies into the effect of RE additions on mold flux viscosity. [31] At 1300°C, the viscosity remained constant up to 15 mass percent RE oxide additions, above 15 mass percent of RE oxide additions the viscosity increases dramatically.

1.3.2.2 Crystallization tendency. The crystallization rate can be controlled by mold flux basicity, the weight percent ratio of CaO to SiO_2 (C/S), literature findings are compiled in Table 1.2. [32] Calcia and silica are the largest constituents of conventional mold powder as shown in Table 1.1. Increasing the basicity increases the crystallization temperature, thus mold fluxes with a C/S < 1 tend to be more glassy, whereas crystallization more readily occurs when C/S > 1. [32] More sophisticated ways of calculating basicity have been introduced where all oxides are considered based on the acidity or basicity, which considers valence state and oxygen affinity, as shown in Equation 5. [33]

$$B = \frac{2X_{CaO}+2X_{BaO}+2X_{CaF_2}+2X_{Na_2O}+2X_{Al_2O_3}+6X_{Fe_2O_3}+\left(2X_{MgO}+2X_{MnO}\right)}{X_{SiO_2}+2X_{Al_2O_3}+X_{TiO_2}+X_{B_2O_3}+\left(X_{MgO}+X_{MnO}\right)} \quad (5)$$

X represents the mole fraction of each compound. The parenthesized expression in the denominator is included if MgO content is greater than 7% or MnO content exceeds 4%. For all other cases the parenthesis in the numerator are used and the denominator is excluded. Although Equation 4 includes BaO, most conventional fluxes do not contain barium. However BaO is being investigated as a potential substitute in fluorine-free mold fluxes. [34] Alumina can behave as a modifier or conditional glass former and is therefore included in both the numerator and denominator of equation 4. Alumina content for conventional mold fluxes is given in Table 1.1; this table does not include alumina content for AHSS mold fluxes, which is discussed in section 1.2.6. Additions of up to 10 wt% alumina have been shown to decrease the crystallization ratio and crystallization temperature, suggesting that alumina inhibits crystal growth through acting as a glass former. [35-36]

One study reports that MnO and MgO can behave as network modifiers when present in low quantities, but in larger quantities, greater than 7 and 4 mole percent respectively, viscosity increases. [33] Lithium oxide and sodium oxide are both alkali

oxides that act as network modifiers. Alkali additions have been noted to change the method of crystallization from surface to bulk by enhancing the number of crystallization sites. [37] Lithium oxide tends to be present in smaller amounts by weight percent, but it is more effective than sodium at lowering T_g and the activation energy for crystal growth, thus enhancing crystallization. [22, 37] However sodium oxide, a primary component in nepheline, is typically added in larger quantities. Calcium fluoride additions greatly reduce viscosity, but have a diminished effect on the melting temperature. Direct effects of CaF_2 on crystallization are unclear, however it has been suggested that CaF_2 causes the precipitation of high temperature phases such as gehlenite and cuspidine. [38]

B_2O_3 is an effective glass former, but is not typically used in conventional mold fluxes. However, boria has been studied for potential use in fluorine free fluxes. [39] Fluorine free mold powders are of interest to steel producers because they avoid dangerous byproducts such as HF which can harm employees and corrode the casting equipment. TiO_2 also uncommon for conventional mold powders, but it has been researched for other

Table 1.2: Compilation of the effects of additions of common mold flux components on the crystallization behavior.

Addition	**Effect on Crystallization**	
Basicity	Increases	< 1 considered glassy
Al_2O_3	Depends	Additions of up to 10 wt% decrease percent crystal and crystallization temperature
MnO	Increases	Only reduces viscosity when less than 7 mol% added
MgO	Increases	Only reduces viscosity when less than 4 mole% added
Li_2O	Increases	More effective than Na_2O at lowering T_g and activation energy for crystal growth
Na_2O	Increases	Added to promote nepheline growth
CaF_2	Unclear	Decreases viscosity and is suggested to precipitate high temperature crystalline phases
B_2O_3	Decreases	Glass former, potential use in fluorine free mold fluxes and AHSS fluxes
TiO_2	Unclear	Suppresses cuspidine formation in favor of other crystalline phases

potential flux applications such as: fluorine free mold powder [39-40], AHSS [42], and casting Ti-stabilized stainless steels [26, 28, 42]. In stainless steel casting when TiO_2 pickup is at 5-10%, cuspidine and perovskite both form. However as TiO_2 additions increase, cuspidine formation is suppressed. [26]

1.3.3. Heat Transfer. Heat transfer between the steel strand and the copper mold is critical to the continuous casting process. It controls the steel shell growth during the strand residence time in the mold. Heat transfer in this system is complex and cannot be defined by a single parameter. The following subsections will introduce the methods used to measure heat transfer, detail the effects of crystallinity and air gap on the heat transfer, and review the compositional effects on heat transfer.

1.3.3.1 Experimental methods. Five primary methods and a sixth blended method have been developed to measure the heat transfer of mold powder. Schematics of each of the experimental methods are shown in Figure 1.4. (1) The pouring method was developed by Shibata et al.; molten slag is poured onto an instrumented copper plate to measure transient heat transfer to the mold. [43] Equipment set-up is relatively simple as shown in Figure 1.4a, but this test is limited because the thickness of the film cannot be varied and it is difficult to compute the heat transfer in transient conditions. [44] (2) The parallel plate experiment improved on the pouring method by adding a thermal gradient. Mold flux is melted on an inductively heated plate and a water-cooled copper plate is placed onto the top of the molten glass. [45-46]While this method is effective for steady state conditions, it does not work well for in-situ experiments. [44] (3) The infrared emitter technique (IET) alleviates many of the problems of the previous two methods. Heat transfer is measured through a mold flux layer by blasting the surface with infrared energy and measuring the temperature of the copper mold beneath the film. [47-48] Varying thickness and unsteady heat transfer conditions can by simulated with this method, but a heating process is employed, which is not representative of the behavior in the mold gap. [44]

(4) Industrial flux film structures can be replicated in the copper-finger test. In this test, a water-cooled finger is dipped into a bath of molten flux; by varying the amount of time in the bath, different structures can adhere and grow onto the finger. Heat transfer is measured by monitoring the water temperature going into and out of the finger and using

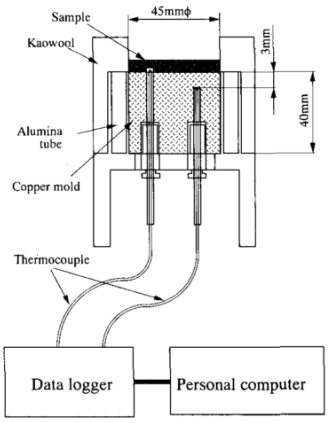

(a)

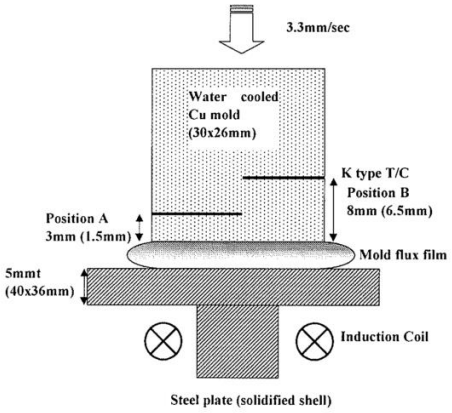

(b)

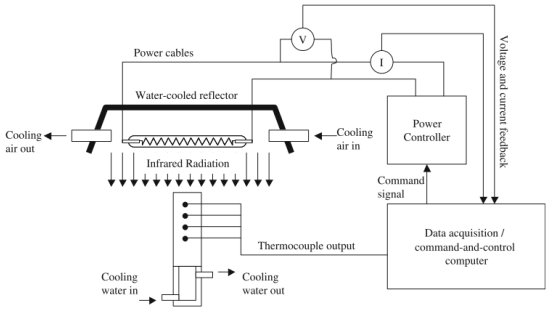

(c)

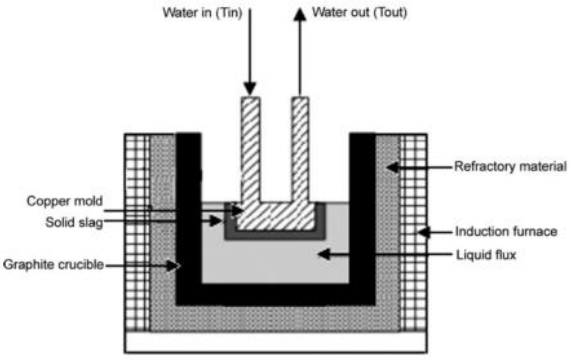

(d)

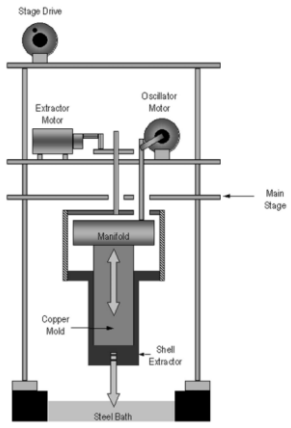

(e)

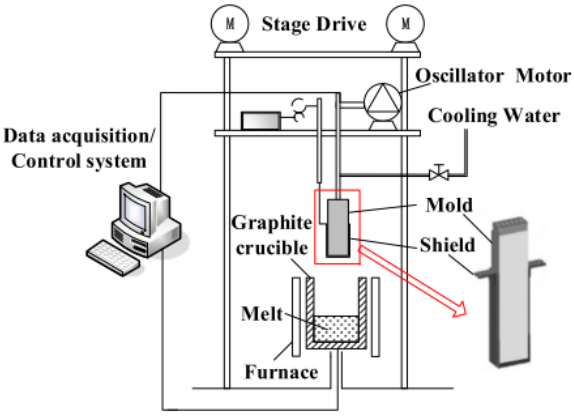

(f)

Figure 1.4: Schematics depicting each of the heat transfer measurement methods: (a) pouring [43], (b) parallel-plate [46], (c) IET [48], (d) copper finger [49], (e) mold simulator [52], and (f) MFHTS [44].

a simple energy conservation equation. [49-51] The copper-finger test is limited by its inability to monitor heat flux in real-time. [44] (5) A mold simulator was developed to simulate the change in heat flux with the growth of the steel shell. This test is ideal to test the heat transfer behavior of a new mold with a various grades of steel without disrupting plant production. [52] A problem with this test is the co-existing multi-factors, which confound the effects of each factor on the overall heat transfer. [44] A sixth method has been developed that combines the copper finger test with the mold simulator set up (Figure 1.4f). The mold flux heat transfer simulator (MFHTS) has an additional set of thermocouples placed beneath the copper finger surface to allow for real-time heat transfer analysis. Resulting flux films are identical to industrially extracted flux films. [44] The six methods presented are able to compute the heat transfer of the mold flux with varying degrees of similarity to an in-use mold.

Methods presented above are intended to measure the overall heat transfer of the system. Additional techniques were used to measure the thermal conductivity of the mold flux with varying degrees of crystallinity. These methods include: FTIR [53-54], laser flash [43, 55-56], non-stationary hot wire method [57-59], and even the double hot thermocouple technique (DHTT) [60]. Since radiative heat transfer has been proven to play a more pivotal role in heat transfer, measuring thermal conductivity is not useful for understanding mold gap behavior as measuring the overall heat transfer.

1.3.3.2 Crystallinity and air gap effects. Researchers agree that crystallization behavior is the dominant influence on heat transfer. [61-68] Crystallization reduces the heat transfer by two mechanisms: (1) shrinkage during crystallization increases the air gap between the mold wall and the mold flux and (2) transmissivity of crystallized mold flux is reduced, overall reducing radiative heat flux. [61] Heat transfer control is critical for steel shell solidification; the required shell thickness is dictated by the steel grade. Peritectic (PC) have a large volumetric shrinkage during the δ-γ phase transition, which increases the stress in the solidified shell, making PC steels prone to longitudinal cracking. Surface quality of PC steels can be improved by increasing the crystallinity and thickness of the film. [62] Low carbon (LC) steels are generally cast at a higher speed because they are more resistant to cracking. Higher casting speeds result in thinner shell thicknesses and higher frictional forces, which increases the probability of a breakout. [63] Therefore, for

LC steels a glassy layer of flux is often maintained between the strand and the mold to increase heat flux and maximize shell thickness before mold exit.

Dynamic flux crystallization experiments by Wang and Cramb [47, 64] showed that crystallization reduces radiative heat transfer by 16-20%, which agrees with work by Ozawa et al. [65] The study by Ozawa suggests that radiative conductivity becomes constant above 15% crystallization and lattice conductivity increased with increasing crystallization. [65] The increase in lattice conductivity was more notable above 20% crystallization, which is speculated to be related to higher lattice connectivity.

An air gap forms between the flux film and mold wall because shrinkage occurs as the flux film crystallizes, thus increasing the surface roughness of the flux film. A study by Cho et al. showed that increased basicity of mold powder can lead to higher shrinkage [66]. Yamauchi et al. noted a 15% reduction in heat transfer for a high basicity flux and proposed three mechanisms for this behavior: 1) an increase in micropores, 2) a high crystalline fraction, and 3) an increase in surface roughness. Several experiments have demonstrated that interfacial resistance controls heat transfer [67], and that the gas type and gap size will heavily influence the heat transfer coefficient. [68]

1.3.3.3 Compositional effects. Additions of certain components can improve or impede the ability to crystallize and so affect the overall heat transfer. J. Diao et al. published two papers concerning the effects of transition metal oxides on the heat transfer behavior of the mold powder, primarily focused on FeO, MnO, and TiO_2. [53, 69] These studies found that transition metal oxides reduce heat transfer, but the effect is more pronounced in crystallized regions than glassy regions. Another study disagreed, showing results that FeO increases the apparent absorptivity and decreases apparent reflectivity, which does not reduce heat transfer. [61] The authors' claim that crystallized mold fluxes can further reduce radiative heat transfer without the addition of FeO. J. Bothma has shown that the effect of TiO_2 during the casting of stainless steels is overshadowed by the increase in viscosity due to the exchange reaction in (4).[70] This increase in viscosity causes porosity and the contact resistance to increase effectively limiting heat transfer.

The effects of basicity and alumina additions on the thermal conductivity were measured in two separate experiments using the same non-stationary hot wire method. [57-58] Basicity increases were shown to decrease the thermal conductivity when $C/S < 1$.

However when C/S > 1, the thermal conductivity became constant. Experimental results also showed that additions of alumina (up to 15-20 wt%) increased the thermal conductivity. [57-58]

Extensive research has been performed to improve the understanding of heat transfer behavior in mold fluxes. Standard techniques are used to study thermal conductivity, while specific experiments have been designed to study the heat transfer behavior of mold fluxes. Studies agree that a larger gap between the flux film and the mold wall reduces heat transfer. Radiative heat transfer will be reduced by increasing the crystallization fraction, but lattice conductivity will increase. Compositional effects on heat transfer are mainly related to the overall effect of the component on crystallization behavior.

1.3.4. Crystalline Phases and Morphology. Crystalline phases that form in the mold gap play a substantial role in the heat transfer and the overall strength of the flux film. Cuspidine has been identified as the primary phase, but several other phases have been reported to form based upon the chemistry of the mold powder. A review of the phases reported in literature are summarized in Table 1.3. This table excludes fluorine-free mold fluxes and phases that form in AHSS mold powders. Most phases reported contain Na, Ca, Si, Al, and O, the primary atomic constituents of mold powders.

Crystal morphology is also important to consider as it often indicates the thermal history of the crystal. Using single hot thermocouple technique (SHTT) and double hot thermocouple technique (DHTT) to create continuous cooling transformation (CCT) diagrams and time-temperature-transformation (TTT) diagrams, Li et al. were able to observe crystal formation at various times and temperatures. [78] At the highest temperatures (>1350°C) equiaxed spherical crystals were observed. Dendritic crystals grew quickly in the range of ~1250°C to 1350°C due to the fluidity of the melt. Equiaxed and columnar growth occurred at low temperatures (1175°C-1250°C), and below 1175°C only columnar growth occurred. [78] A study by Mizuno et al. observed similar structures in laser microscopy samples and glass films heat treated at various temperatures in a resistance furnace. [80] In this case directional columnar grains were observed at 800°C and equiaxed dendrites formed at 600°C. Dendritic growth suggests a large undercooling during quenching, which in the case of the glass films could indicate nucleation had already

Table 1.3: A review of phases reported in literature through cooling from a liquid or aging from a glass.

Phases	Formula	References
Cuspidine	$Ca_4Si_2O_7F_2$	[51,71-81]
Nepheline	$NaAlSiO_4$	[72, 76, 82]
Combeite	$Na_2Ca_2Si_3O_9$	[71, 73, 82]
Gehlenite	$Ca_2Al_2SiO_7$	[71, 73, 82-83]
Melilite	$(Ca,Na)_2(Al,Mg,Fe^{++})(Si,Al)_2O_7$	[83]
Akermanite	$Ca_2Mg[Si_2O_7]$	[83]
Sodium Silicate	Na_2SiO_3	[72]
Pseudo-wollastonite	$CaSiO_3$	[72]
Hematite	Fe_2O_3	[72]
Wollastonite	β-$CaSiO_3$	[73, 81, 82]
Larnite	Ca_2SiO_4	[73]
Rankinite	$Ca_3Si_2O_7$	[73]
Merwinite	$Ca_3Mg(SiO_4)_2$	[73]
Hatrurite	Ca_3SiO_5	[73]
Fluorite	CaF_2	[74, 77]
Sodium fluoride	NaF	[76-77]
Calcium silicate hydrate	$Ca_2Si_6O_{17}(OH)_2$	[77]
Tetrasodium aluminosilicate	$Na_4Al_2Si_2O_9$	[78]
Calcium sodium silicate	$Na_2Ca_2Si_2O_7$	[78]
Disodium aluminosilicate	$Na_4Al_2Si_2O_9$	[82]

occurred in the glass during the initial quench. Other authors attribute the dendritic crystal growth to basicity or cooling rate. [51, 74, 81, 84] Dendritic growth can occur homogeneously (equiaxed crystals) or heterogeneously by nucleating and growing off of another phase or pore. [74] Although phases are readily identified via XRD and morphologies viewed using SEM, a correlation between thermal history, phase, and crystal morphology has only be clarified at short times. [85] The devitrification behavior below the nose of the curve needs to be studied for longer times.

1.3.5. Fluxes for Advanced High Strength Steel (AHSS) Casting. Steel production in some countries is inexpensive due to reduced labor costs. In order to stay competitive, many American companies are pushing to produce niche steels that are difficult to cast, such as high aluminum transformation-induced plasticity (TRIP) and

peritectic steels. High aluminum steels are difficult to cast because the aluminum in the steel will reduce less stable oxides in the mold powder such as SiO_2 and MnO: [86] Components in brackets are in the steel and parenthesized components are in the mold flux.

$$3(SiO_2) + 4[Al] \rightarrow 3[Si] + 2(Al_2O_3) \quad (6)$$

$$3(MnO) + 2[Al] \rightarrow 3[Mn] + (Al_2O_3) \quad (7)$$

These exchange reactions will minimally effect the composition of the steel, however the composition of the mold powder can be greatly affected. The alumina content of the mold powder can increase up to 30% [87], which affects the properties of the mold powder. Residence time in the mold gap can drastically change the lubrication and heat transfer behavior of the mold powder.

Additions of various modifiers have been investigated to evaluate their effect on critical properties such as crystallization temperature, critical cooling rate and the crystalline phases formed. The primary crystalline phase that forms in Ca-Si based AHSS mold fluxes is CaF_2. [88-90] This phase can be modified with up to 10% TiO_2 addition, which increases the crystallization temperature and forms MgO, $Ca_{12}Al_{14}O_{33}$, and $CaTiO_3$. [91] Li_2O suppresses crystallization by decreasing the critical cooling rate and the crystallization temperature. [88] Lithia also inhibits high temperature phase formation by increasing the incubation time; crystallization of cuspidine and $Ca_2Al_2SiO_7$ are suppressed in favor of $LiAlO_2$. Na_2O also suppresses crystallization and decreases the crystallization temperature. Sodium promotes nepheline growth and decreases incubation time. [88] BaO inhibits crystallization and promotes Ba-rich phases. [89] BaO also increases heat transfer, reduces the crystallization temperature and critical cooling rate, and curtails the effect of increasing alumina to silica ratio. [90] Alone, additions of B_2O_3 inhibit the crystallization of CaF_2. [89] However in combination with BaO, B_2O_3 promotes crystallization in the high temperature region and CaF_2 forms. [89] MnO is a reducible oxide and may be exchanged with aluminum in the steel, although additions of MnO improve heat transfer by reducing the thickness of the crystallized layer and increasing the thickness of the liquid flux. [92]

Research has been focused on eliminating the Si-Al exchange reaction, primarily through the development of Ca-Al based fluxes. [93] Slabs were successfully cast with reduced surface defects and less than 5% overall alumina pick up by using a Ca-Al based flux. [94] Crystallization temperatures of Ca-Al fluxes are lower than conventional Ca-Si fluxes, Ca-Al fluxes can also crystallize cuspidine, lower heat transfer at the meniscus, and yield complex morphologies. [95] Casts employing Ca-Al based fluxes have been successful, but more development work is needed in this area. It is necessary to improve our understanding of the phases that crystallize and how to control the formation of the complex crystal morphologies.

1.4. KINETICS

This section will provide an overview to the homogeneous and heterogeneous nucleation behavior and growth phenomena. The Johnson-Mehl-Avrami (JMA) technique for analyzing the combined nucleation and growth behavior will also be detailed.

1.4.1. Nucleation Theory. [96] A barrier exists for the formation of a new phase from a liquid or a gas. The new phase forms by agglomerating a small nucleus of atoms. The rate of movement of atoms to and from the nucleus defines the rate of new phase formation. Nucleation can occur homogeneously or heterogeneously. Homogeneous nucleation occurs by the spontaneous formation and growth of nuclei of the new phase. Heterogeneous nucleation lowers the surface energy barrier of nucleation by initiating the new phase on a foreign phase or particle. Mathematical considerations of the energy barrier of homogeneous and heterogeneous nucleation will be discussed in the following sections.

1.4.1.1 Homogeneous nucleation. [96] Max Volmer invented nucleation theory by considering the surface energy barrier difference between small particles and the bulk phase. He assumed that the free energy favoring nucleation formation would have to balance with the decreased free energy of the new phase with the increased surface energy required to form a new cluster. Assuming the cluster is a sphere with radius r, Volmer was able to define the change in free energy for cluster formation as:

$$\Delta G_r = \Delta G_V \frac{4}{3}\pi r^3 + \gamma 4\pi r^2 \quad (8)$$

where ΔG_V is the change in free energy per unit volume and γ is the surface tension. Separating Equation 8 into two terms, the first term describes the bulk free energy of the new phase and the second term refers to the surface free energy of the nuclei. If ΔG_r is plotted as a function of radius, a critical radius (r*) can be defined; r* is the radius when the bulk free energy and the surface free energy term are equal.

$$r^* = \frac{2\gamma}{\Delta G_V} \quad (9)$$

For radius sizes greater than r* nucleation is possible because the bulk free energy of the new phase is larger than the surface free energy term, however below r* nucleation will not occur because the surface free energy is too large. This relationship is graphically shown as Figure 1.5. By substituting r* (Equation 9) back into free energy for cluster formation equation (Equation 8), the free energy to form a cluster can be calculated.

$$\Delta G_{r^*} = \frac{16}{3}\frac{\pi\sigma^3}{(\Delta G_V)^2} \quad (10)$$

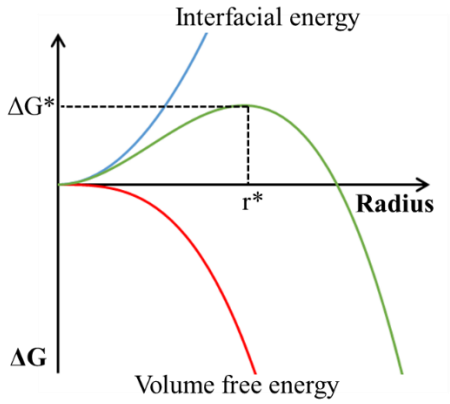

Figure 1.5: Gibbs free energy as a function of the radius of the nucleus. The critical Gibbs free energy (ΔG*) and critical radius (r*) are defined to occur when the interfacial energy is equal volume free energy.

Since the probability of finding a fluctuation of energy, W, is given by a Boltzmann factor: exp (-W/kT), the probability of finding a cluster of critical size r* among N atoms is:

$$\frac{N_{r^*}}{N} = \exp\left(-\frac{\Delta G_{r^*}}{kT}\right) = \exp\left(-\frac{16\pi\sigma^3}{3kT(\Delta G_v)^2}\right) \tag{11}$$

The probability of finding a critical size cluster in Equation 11 can be related to the nucleation rate (I) by:

$$I = \frac{N_{r^*}}{N} \cdot v \tag{12}$$

where υ is the atomic jump frequency. Equation 11 can also be related to temperature to solve for various degrees of undercooling by expanding the volume free energy term into its components:

$$\Delta G = \Delta H - T\Delta S \cong \Delta H - \frac{T}{T_m}\Delta H = \Delta H\left(1 - \frac{T}{T_m}\right) = \frac{\Delta H}{T_m}(T_m - T) = \frac{\Delta H}{T_m}(\Delta T) \tag{13}$$

where H is enthalpy, S is entropy, T is temperature, and T_m is the melting temperature. When Equation 13 is substituted into Equation 11, the result is an equation that relates the critical cluster size to the degree of undercooling (ΔT).

$$\frac{N_{r^*}}{N} = \exp\left(-\frac{16\pi\sigma^3}{3kT\left(\frac{\Delta H}{T_m}(\Delta T)\right)^2}\right) \tag{14}$$

A critical cluster homogeneously nucleated from a liquid typically contains about 300 atoms. [96] The free energy required to form a cluster accounts for the free energy change necessary for all 300 atoms. Nucleation occurs rapidly once a certain degree of undercooling is achieved, especially in systems where atom mobility is high such as a liquid metal. In systems with high viscosity, such as glasses, the growth rate of nuclei can

be reduced so the rate can be measured. Surface tensions are difficult to measure because of surface irregularities and defects in the structure, therefore it is not straightforward to use the equations stated above. Additional limitations of the classical nucleation theory include: assuming the critical nucleus is a sphere, ignoring free energy contributions from other sources such as stress, and assuming the cluster is at equilibrium. Despite the limitations of classical theory, Zanotto and James validated that classical theory satisfactorily described the temperature dependence of nucleation rates over a wide range of temperatures for lithium silicate and barium silicate melts. [97] In addition, Zanotto and James suggest that the interfacial energy may not be independent of temperature as assumed.

1.4.1.2 Heterogeneous nucleation. Homogeneous nucleation assumes that nucleation occurs spontaneously due to the reduction in free energy for nuclei greater than a critical size. However, there are often foreign particles present that can act as nucleation sites and further reduce the energy barrier for nucleation. In heterogeneous nucleation, the wetting angle (θ) describes the interaction of the new phase with that of a foreign particle. When surface tension between the two phases is low, θ is small. Complete wetting occurs when θ = 0. The wetting angle and the surface tensions between a nucleating droplet and a mold wall are shown in Figure 1.6. Balancing the surface tension terms yields:

$$\gamma_{LM} = \gamma_{SM} + \gamma_{SL}\cos\theta \tag{15}$$

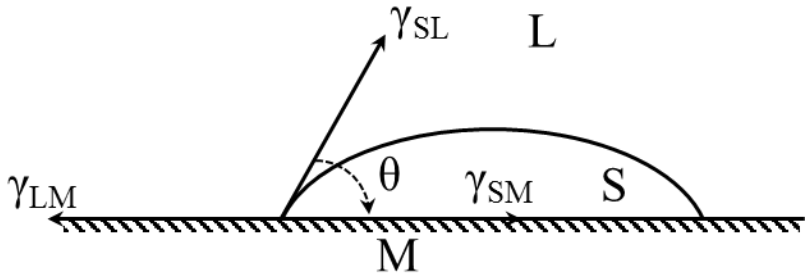

Figure 1.6: Schematic of a solid droplet (S) heterogeneously nucleating along a mold wall (M) from a liquid (L). The surface tension (γ) between each phase and the contact angle (θ) are labelled.

The free energy for heterogeneous nucleation is expressed as:

$$\Delta G_{Het} = V_s \Delta G_V + A_{LS}\gamma_{SL} + A_{SM}\gamma_{SM} - A_{LM}\gamma_{LM} \quad (16)$$

where A is the interfacial area and Vs is the volume of the droplet. Since $A_{LM} = A_{SM}$, Equation 15 can be substituted into Equation 16 and simplified:

$$\Delta G_{Het} = (2 - 3cos\theta + cos^3\theta)\left[\frac{1}{3}\Delta G_V \pi r^3 + \gamma_{LS}\pi r^2\right] \quad (17)$$

The free energy for heterogeneous nucleation (Equation 17) related back to homogeneous nucleation (Equation 8) is:

$$\Delta G_{Het} = \Delta G_{Homo}\left[\frac{2 - 3cos\theta + cos^3\theta}{4}\right] \quad (18)$$

When θ = 90°, the free energy for heterogeneous nucleation is reduced to half of the free energy for homogeneous nucleation. Even at non-wetting conditions (θ > 90°) the free energy for nucleation is reduced for heterogeneous nuclei. Additional surface roughness can also further reduce the free energy required for nucleation. When foreign particles are present, it is far more likely that phases will nucleate heterogeneously because the free energy is significantly reduced for cluster formation.

1.4.2. Growth Behavior. This section reviews the classical models for crystal growth from a glass melt; these mechanisms occur after the nucleation of critical-sized nuclei. K.A. Jackson, D.R. Uhlmann, and J.D. Hunt pioneered many of the classic growth models used today. [98] The main points on the theory of interface motion and overall growth are summarized by I. Gutzow in [99]. A brief introduction to growth velocity and the mechanisms of crystal growth will be presented here. The crystallization velocity, V, of a crystal growing in a supersaturated phase is temperature dependent and can be related by:

$$V \cong const.\times z \left[1 - \exp\left(-\frac{\Delta\mu}{kT}\right)\right]\Omega \tag{19}$$

Where z is the impingement rate of the molecules of the ambient phase, Δμ is the thermodynamic driving force (i.e. the supersaturation), and Ω is a function of Δμ. The form of Ω is dependent on the growth mechanism.

For normal growth, molecules are incorporated directly into growth sites of the advancing crystal, causing Ω to be constant and equal to the relative number of growth sites. This type of growth is only possible on non-equilibrium, high-faceted crystal faces. Melts with structurally similar corresponding crystals with atomically rough interfaces have been shown to increase the number of growth sites, causing continuous growth.

Spiral growth is only possible when the growing crystal phase contains screw dislocations. The screw dislocations act as a constant source of growth sites and the driving force becomes:

$$\Omega = \frac{d\Delta\mu}{4\pi V_{m\sigma}} \tag{20}$$

Where σ is the specific surface energy at the interface, V_m is the molar volume, and d is the inter-atomic spacing of the crystal.

Two-dimensional nuclei formed onto a foreign crystal can also act as growth sites for lateral crystalline layer propagation. For this growth mechanism, the thermodynamic driving force is:

$$\Omega = const.\times \exp\left(-\frac{K_2}{kT\Delta\mu}\right) \tag{21}$$

$$K_2 = \frac{\pi\sigma^2 V_m d}{R} \tag{22}$$

Lateral growth by either surface nucleation or spiral growth is only possible for high entropy melts. For these growth mechanisms to occur in lower entropy systems, a greater degree of undercooling is necessary.

All three mechanisms of crystal growth can occur at small undercoolings for simple glass forming melts. The valid range for growth mechanisms is predicted by melt to crystal structure similarity. Lateral growth modes are only observed in glass forming melts where the crystallization process is tied to significant structural changes. Spiral growth is the predominant form of reconstructive crystallization. It is theoretically possible that the growth mechanism will change based upon the degree of undercooling, however it is difficult to prove this transition experimentally.

1.4.3. JMA Kinetics. [96, 100] Johnson - Mehl - Avrami (JMA) kinetics is a model for nucleation and growth that assumes both behaviors occur simultaneously throughout the transformation period. There are four primary assumptions for this model: (1) the growth rate of the nucleus is constant, (2) nucleation is homogeneous (or heterogeneous on randomly dispersed nuclei), (3) the nucleation rate is constant, and (4) the new phase grows as a sphere. The derivation for the model can be found in [96] and will not be repeated here. The Johnson-Mehl equation models the volume of material transformed as a function of nucleation and growth rate.

$$X_f = 1 - \exp\left(\frac{-\pi}{3} I \mathrm{v}^3 t^4\right) \tag{23}$$

In Equation 23, X_f is the fraction transformed, I is the nucleation rate, v is the constant growth rate, and t is time. This form of the equation corrects for nuclei overlap. Avrami proposed a more general form of this equation.

$$X_f = 1 - \exp(-(kt)^n) \tag{24}$$

$$k = k_0 \exp\left(\frac{-Q}{RT}\right) \tag{25}$$

where k_0 is the attempt frequency, n is the time exponent, and Q is the activation energy. If k_0, n, and Q are constant over a range of temperatures the reaction is considered isokinetic. Large values of n indicate a fast reaction, whereas smaller values of n correspond to a slower reaction. The parameter k shifts the curve left and right, high k values result in shorter incubation times whereas small k values have longer incubation times. To solve for Avrami constants the fraction transformed is measured at isothermal temperatures and plotted as a function of time. Figure 1.7 is a typical graphical representation of a JMA curve. With changes in temperature, the shape of the curve will remain the same, but the curve will be translated to longer or shorter times. Shifts in k_0 have the same effect, the overall shape remains, but larger k_0 values shift to shorter times. Changes in n correspond to a change in slope; when n increases, growth occurs over a shorter period of time and the slope increases.

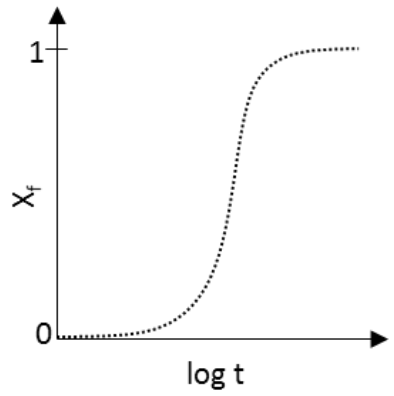

Figure 1.7: A typical JMA curve plotting fraction transformed as a function of log time.

The JMA equation can be used to find the time required for a particular fraction of transformation. Typically 5% is used to define the onset of crystallization and 95% indicates the end of the reaction. This translates well into a time-temperature-transformation (TTT)-diagram, which will be expanded upon in section 1.5.2. A useful way to extract the kinetic constants from the crystallization data is to plot $-\ln(1-X_f)$ versus time on a double log plot. Equation 26 can be used to extract the values of n and k.

$$\log\left(-ln\left(1-X_f\right)\right) = n\log(k) + n\log(t) \tag{26}$$

Equation 26 follows the linear equation form, y = mx + b; n is defined by the slope of the line and the intercept is equal to n log (k). The activation energy of the reaction can also be determined by using Equation 28. The validity of the JMA model can be tested by an isothermal method (Equation 27) and an isochronal method (Equation 25). Non-linear portions of the plotted isothermal data indicates that the behavior is deviating from Avrami kinetics.

$$\frac{d\ln(-\ln\left(1-X_f\right))}{d\ln\left(\frac{1}{T}\right)} = n \tag{27}$$

$$\frac{d\ ln\left[-\ln\left(1-X_f\right)\right]}{d\ln\left(\frac{1}{T}\right)} = \left(\frac{nQ}{R}\right) \tag{28}$$

The Johnson Mehl equation is similar to the Avrami equation, but it introduces separate exponents for nucleation and growth.

$$X_f = 1 - \exp\left(-\frac{\pi}{3}J^r G^s t^{r+s}\right) = 1 - \exp((-kt)^n) \tag{29}$$

In Equation 29, n = r + s. When separated into nucleation and growth portions, the exponents give insight to the mechanism of nucleation and growth. When s = 1 needle like growth occurs, s = 2 results in plate-like growth, and when s = 3 crystal growth is spheroidal. The nucleation component, r, defines the nucleation rate. When r = 1 the nucleation rate is constant, if r > 1 the nucleation rate increases with time, and if r < 1 nucleation rate decreases with time. Nucleation is complete and site saturation has been achieved when r = 0. The JMA method is commonly used to produce TTT-diagrams and to determine the mechanism of both nucleation and growth.

1.5. CCT & TTT CRYSTALLIZATION DIAGRAMS

Two diagrams are commonly generated to describe crystallization phenomena: continuous cooling transformation diagrams (CCT) and time-temperature-transformation (TTT) diagrams. CCT diagrams are experimentally determined by cooling a liquid from a melt and measuring the crystallization temperature during cooling. Some tests determine the onset of crystallization by visually observing the sample throughout the entire test. [85] Thermal techniques detect a peak, which indicates an exothermic transformation. [101] A CCT diagram is generated by performing the experiment at different cooling rates.

TTT diagrams are generated using isothermal techniques. The onset of crystallization is either determined optically or with a characterization technique such as X-ray diffraction (XRD). The resulting shape of a TTT diagram is typically a "C", where the lowest and highest temperatures take the longest amount of time to crystallize. [85] The nose of the TTT-curve defines the separation between crystallization and glass formation. The cooling rate that crosses the nose of the TTT-cure is called the critical cooling rate (CCR). Samples cooled faster than the CCR are glassy; samples cooled slower are crystalline.

TTT diagrams and CCT diagrams appear to map out the same regions, however the two diagrams do not generate the same curve. Since CCT curves are generated by continuous cooling, crystallization temperatures are lower and longer times are required for the onset of crystallization compared to isothermal techniques. A lot of development has gone into transforming CCT diagrams into TTT diagrams and vice versa for steels. [102] This ultimately led to the creation of the JMatPro software, which, unfortunately, is not as good at converting oxide systems. However, using Scheil's additivity rule CCT diagrams can be converted to TTT diagrams for oxide systems. [40] This rule assumes that the continuous cooling curve can be described by the addition of several small isothermal steps.

$$\sum_{i-1}^{n} \frac{\Delta t_i}{\tau_i} = 1 \tag{30}$$

In Equation 30, Δt_i represents the time period for the i-th isothermal step and τ_i is the ideal incubation time of TTT-diagram at the same temperature of the i-th isothermal step.

1.5.1. Experimental Methods. In the following sections, several techniques used to generate both TTT and CCT diagrams will be outlined to highlight the advantages and disadvantages of each technique. In addition, the effect of composition on the crystallization temperature and incubation time will be discussed for mold flux systems.

1.5.1.1 Differential thermal analysis (DTA). Differential thermal analysis is a robust technique for materials analysis. Heat is applied to a sample and a reference material simultaneously, while the temperature of each sample is continuously monitored with thermocouples. [103] As the sample goes through physical and chemical changes, such as melting, decarburization, crystallization etc., the monitored temperature is affected by changes in internal energy. By monitoring differences in temperature between the sample and the reference, temperature and energy for the physical and chemical changes can be determined.

DTA is used to determine the crystallization temperature of materials at different cooling rates. [104] The crystallization temperature is defined by the onset of the exothermic peak on cooling. DTA can be used to generate CCT curves by cooling at various rates and determining the crystallization temperature. [105] However, this technique is limited to slow cooling rates, which often are not representative of the mold gap. [106] Most commercial DTA units are limited to sample sizes of less than one gram, which intensifies the effect of compositional changes. Maldonado et al. were able to use DTA to determine the kinetic parameters for mold flux powders using a Kissinger-type equation, which was used to predict the TTT-diagram. [107] A Kissenger-type equation

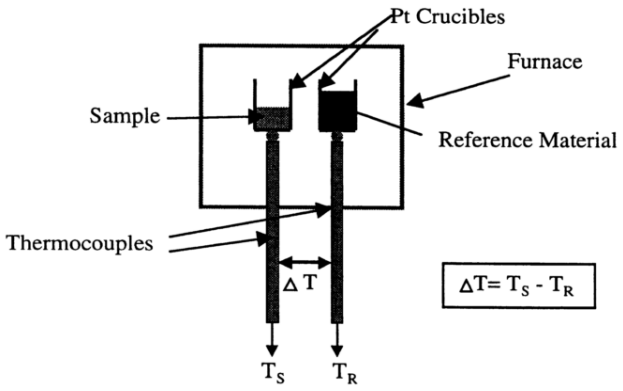

Figure 1.8: Schematic of a typical DTA experimental set up from [104].

can be used to determine the activation energy and an Arrhenius pre-exponential factor and can take the form shown in Equation 31.

$$\ln\left(\frac{\beta}{T_m^2}\right) = \left(\ln(Zn(1-x_m)^{n-1}\right) - \ln\left(\frac{E}{R}\right)) - \frac{E}{R}\left(\frac{1}{T_m}\right) \quad (31)$$

where β is the heating or cooling rate, Z is the pre-exponential factor, E is the activation emergy, T_m is the melting temperature, x_m is the volume fraction of crytals at the peak maximum, R is the gas constant, and n is the order of the reaction. The predicted TTT-diagram is in good agreement with experimental results.

1.5.1.2 Differential scanning calorimetry (DSC). Differential scanning calorimetry is a testing method patented by E. Watson and M. O'Neil. [103] Instead of applying constant heat and monitoring temperature changes like DTA, in DSC heat is added to maintain constant temperature between a specimen and a reference. This provides a direct quantitative measurement of heat effects, as well as increased sharpness and resolution. Faster speeds can be used to survey a wide range of temperatures in a short time. DSC is capable of using smaller sample sizes than DTA, which intensifies the issue of compositional change. However this could be mitigated by using sealed sample holders.

DSC was employed by Meng et al. to create CCT curves with cooling rates from 1 to 30°C/sec. [105] Since DSC is limited to slow cooling rates relative to the critical cooling rate of most fluxes, the authors had to employ a different technique to increase the cooling rate. Maldonado et al. also used DSC to determine the kinetic parameters for a Kissenger-type equation so the TTT curve could be predicted. [109] The DSC predicted TTT-diagram agrees well with the experimentally determined diagram.

1.5.1.3 Single hot thermocouple technique (SHTT). Single hot thermocouple technique was developed by Kasiwaya et al. for in situ observation of crystallization phenomena and to overcome the slow cooling rates needed for DTA and DSC. [110] SHTT technique utilizes a complex control system that rapidly alternates between heating the specimen and monitoring temperature. The B-type thermocouple is bent into a U-shape and a small glass specimen (< 1g) is balanced on the thermocouple as shown in Figure 1.9 (a). The specimen is melted and held at temperature to ensure uniformity, then quenched following the desired thermal profile. This method has been used to directly continuously

cool samples for CCT diagrams [101, 110-113], and to isothermally age samples for TTT diagrams [101, 110-114].

SHTT is limited to small sample sizes (< 1g) and slower cooling rates (max 16°C/s) relative to those experienced in the mold (average of 20-25°C/s, locally 50-100°C/s). [106] In addition, because the crystallization behavior can be directly observed, the flux compositions that can be tested are limited to transparent systems. Transparent flux systems often exclude transition metal oxides such as FeO and MnO, which can significantly impact the crystallization behavior of the flux.

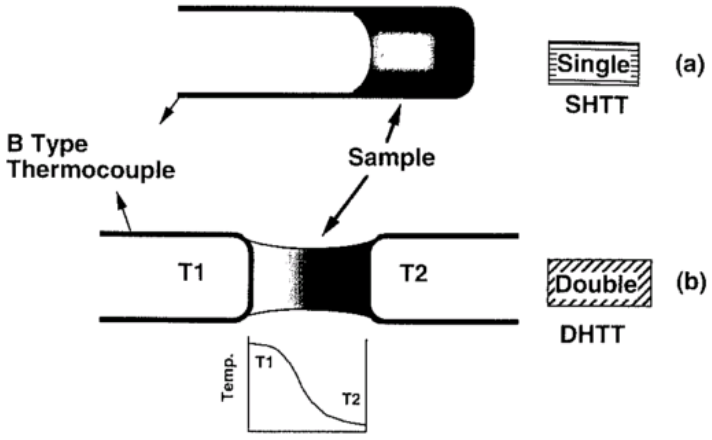

Figure 1.9: Schematic of the sample region of (a) SHTT and (b) DHTT technique from [110].

1.5.1.4 Double hot thermocouple technique (DHTT). Double hot thermocouple technique is an extension of SHTT. As shown in Figure 1.9 (b), DHTT employs two thermocouples which can introduce a thermal gradient in the flux sample. [110] The sample size of the flux is still small (15-20mg) [104], but because this method employs a thermal gradient it is more representative of mold gap behavior. DHTT can be used to generate CCT [85, 110] and TTT-curves [85, 115]. This technique is often used to see how crystallization behavior changes with the introduction of a thermal gradient [116]. The

same limitations of SHTT apply to DHTT: small sample size, slower cooling rates relative to the mold, and the flux must be transparent.

1.5.1.5 Confocal scanning laser microscopy (CSLM). Crystallization behavior can be observed in-situ using a hot-stage CSLM. A halogen lamp heats the sample while temperature is continuously monitored with a thermocouple as shown in Figure 1.10. [117] Sample images are continuously recorded and crystallization temperature and can be reviewed to determine the time and temperature of crystallization. In a conventional CSLM, fluorine cannot be controlled once it volatilizes, which impacts the overall chemistry of the flux. Park et al. modified their microscope to include a quartz cover to isolate the observation and contain volatiles. [118]

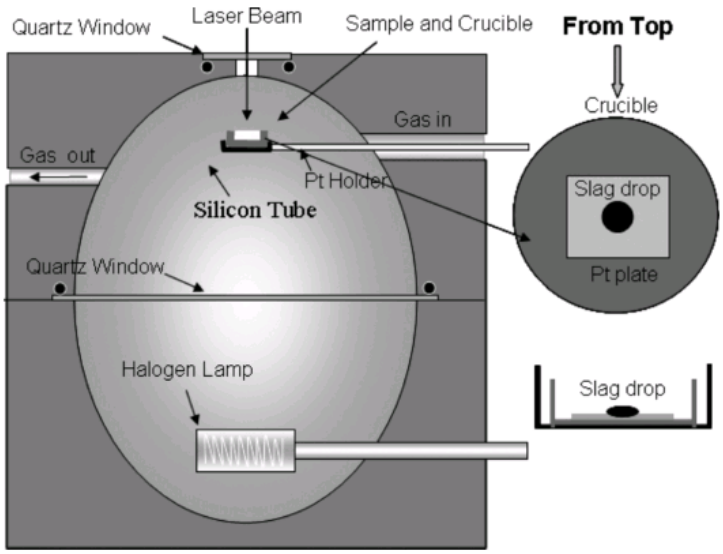

Figure 1.10: Schematic of a typical CSLM set up for mold flux crystallization analysis from [117].

CSLM is a high magnification technique, which aids in measuring small (~50μm) crystal. However, the surface area of the sample is large at high magnification and it is difficult to find the first crystal to measure the size. [104] In addition, CSLM microscopes are expensive and thus inaccessible to many researchers.

1.5.1.6 Other techniques. The previously described methods are commonly used to study mold powders. Techniques reviewed in this section are more uncommon, but have been employed by a few research groups. Before the use of SHTT and DHTT, many researchers would use a quench, re-heat, and isothermal age method to determine the TTT-diagram of the system. Using this technique, molten flux was quenched to room temperature and confirmed to be completely glassy. The material was then reheated in a furnace to an isothermal temperature and aged to investigate the devitrification behavior. [108] This method does not replicate the thermal history of the fluxes in the mold, thus it is expected that the crystal morphologies and incubation times will differ from those quench to and held at the aging temperature directly.

Prasad et al. review the segmented mold or "step chill" method used to generate CCT diagrams. [106] A stair-step type mold with eight cells of different widths can be used to test eight cooling rates at one time. Temperature is monitored in each cell and differentiated to identify thermal arrests, which indicate a phase change. Crystal phases and morphology must be analyzed using other characterization techniques such as XRD and microscopy.

An atomizer technique can also be employed to generate the highest cooling rates. [104, 106] Glassy samples can be made for other methods or this technique can be used to analyze flux crystallization behavior. This method uses a high speed two color pyrometer, which can measure temperature, velocity and size. If crystals nucleate in the droplet the pyrometer will note the discontinuity in the trajectory.

The dip thermocouple method can be used to increase the cooling rate experienced by the mold flux relative to DSC or DTA. A thermocouple is dipped into molten flux, then removed and allowed to cool in air. As the droplet of flux at the end of the thermocouple cools, the temperature is continuously monitored. [104, 106] Thermal data can be analyzed by differentiating and identifying the thermal arrest that corresponds to crystallization.

1.5.2. Compositional Effects. Similar trends can be noted between the compositional effects on CCT and TTT diagrams and the viscosity effects discussed earlier in Section 1.3.2.1. Flux composition can change the crystallization temperature and critical cooling rate on the CCT diagram. Incubation time, the time it takes to initiate crystallization, can vary in TTT diagrams.

Zirconia is commonly added to mold powders to promote crystallization. The crystallization temperature increases with increasing zirconia content. This is attributed to the zirconia acting as a site for heterogeneous nucleation. [111, 119] The incubation time varied based on temperature; at low temperature zirconia additions increased the viscosity and the incubation time increased. [111] When temperatures were elevated the incubation time was shortened, which was attributed to the decreased energy required for heterogeneous nucleation.

Shu et al. observed no obvious effects of small (< 5 wt%) titania additions on the TTT-diagram. [39] Additions greater than 5% slightly decreased the incubation time. Another study noted an increase in incubation time with 2% titania additions. [111] As titania additions increased the nose of the curve became less sharp, eventually forming a double-nosed curve. Both studies agree that large (> 5 wt%) additions of TiO_2 decrease incubation time.

Increasing of lithium oxide content in lime-alumina based mold fluxes decrease the crystallization temperature. [88] CCT diagrams of conventional fluxes showed that additions less than 6 mass% Li_2O easily formed a glass. Larger additions (> 6 mass%) increased the critical cooling rate by 4°C/s for every 1% lithium oxide added. [112] As lithium content was increased the incubation time increased at high temperatures and decreased at low temperatures. Lu et al. confirmed a decrease in incubation time at low temperatures after a critical addition (4-7 wt%) of lithium. [88]

Sodium oxide additions lower the crystallization temperature of lime-alumina based mold fluxes, but have no impact on the critical cooling rate. [88] Incubation time is short at midrange temperatures, but increases dramatically at higher and lower temperatures. Increasing sodium oxide content does not change the incubation time at low temperatures, but increases the incubation time at high temperatures. The opposite effect occurs for MC steel flux compositions; Na_2O promotes crystallization and increases the crystallization temperature. [78] Furthermore, incubation time is reduced at all temperatures with increasing Na_2O content. Both studies note that when Na_2O levels are high (> 7.5 mass%), the effect of additional Na_2O on crystallization behavior is diminished. The differences in the results of the two studies emphasizes the importance of the interaction of all components in the system. In fluxes with more alumina, Na_2O additions

balance the alumina ion in the glassy network, increasing the glassiness of the system. However in conventional fluxes sodium additions break up the glassy network and promote crystallization.

B_2O_3 is a glass forming oxide, therefore the additions of boron oxide contribute to the glassy network. In a study of boron oxide additions between 0 and 5%, the incubation time increased by an order of magnitude. [39] In AHSS studies of lime-alumina mold powders, B_2O_3 has been added in excess of 15 wt% to keep the flux glassy throughout the casting sequence. [87]

MnO additions have only been studied for lime-alumina based fluxes using the crystal fraction in DHTT thermal gradient experiments. [92] Results showed that additions of MnO increase in the liquid content of thermal gradient samples. MnO weakens the crystallization behavior of the flux by contributing the polymerization of the glassy network.

Shifts in TTT diagrams and CCT diagrams are directly related to the effect of each addition on the glassy network. Polymerized networks take more time to crystallize, increasing incubation time and lowering the crystallization temperature. Depolymerized networks crystallize more easily, which translates to an increase in crystallization temperature and a decrease in incubation time.

1.6. CHARACTERIZATION TECHNIQUES

Conventional techniques such as scanning electron microscopy (SEM), energy dispersive spectroscopy (EDS), X-ray diffraction (XRD), and differential thermal analysis (DTA) were used to characterize samples from experiments conducted in this work. These methods are common and technique limitations are generally well known. This section will focus on lesser known techniques that were employed for sample analysis: cathodoluminescence (CL) and Reitveld analysis. This section will detail background information about each technique and describe some of the limitations of the characterization method.

1.6.1. Cathodoluminescence Microscopy. Similar to scanning electron microscopy (SEM), cathodoluminescence phenomena is observed by impinging electrons onto a material surface. Electron excitation of the affected atoms results in the emission of

photons. This technological phenomena was first used for cathode ray tube based instruments. As electron microscopy was developed, CL has become a critical characterization technique in geology and has expanded to other fields. [121] CL provides two pieces of information: microscopy and spectroscopy. Microscopy produces a luminescent map of a region, whereas spectroscopy obtains a spectra at a specific point of interest. Steel industry applications primarily use the microscopy aspect of CL. [87, 122-127] This technique uses a relatively simple set up with a small high-vacuum chamber with an optical window, which can be mounted onto an optical microscope. [121] A "flood illumination" electron gun, where a wide spray of electrons impinge the surface of the sample, is used to produce large total CL intensities, which increases the spectral resolution of the region. This technique is considered non-destructive, but can ionize or create defects in the surface of the sample. [121] This is a non-issue for steel industry samples, but can cause issues for materials where the defect chemistry is critical.

Luminescence phenomena are sensitive to slight changes in the material. Changes in CL are noted to occur due to intrinsic and extrinsic factors. Intrinsic factors are related to the structure and fundamental band gap of the material. [121] Extrinsic factors are associated with impurities in the band gap caused by: an increase in temperature, local defects, electric field, stress, and local chemistry changes. There is not a systematic way to separate the effect of intrinsic and extrinsic factors on CL bands because an applicable theory has not yet been developed. Consequently it is difficult to use CL as a quantitative technique. [121] Therefore, CL is often used in conjunction with other characterization methods. This methodology is limited to low magnification images due to objective lenses with long working distances, which cannot resolve multiphase regions smaller than 20μm. [122]

1.6.1.1 Application of CL to the steel industry. CL was used in the steel industry to research inclusions, nozzle clogging, slags, and other non-metallic components. [122-126]. Different phases have distinctive CL colors, distinguishing changes in chemistry in different regions. For example corundum (Al_2O_3) is bright red in CL, whereas spinel ($MgAl_2O_4$) is bright green. [122] M. Karakus et al. examined a nozzle clog area using CL and discovered that, although it was previously suspected to be corundum, the clog was mostly comprised of spinel. [123] In the reflected light image (Figure 1.11A) the clog area

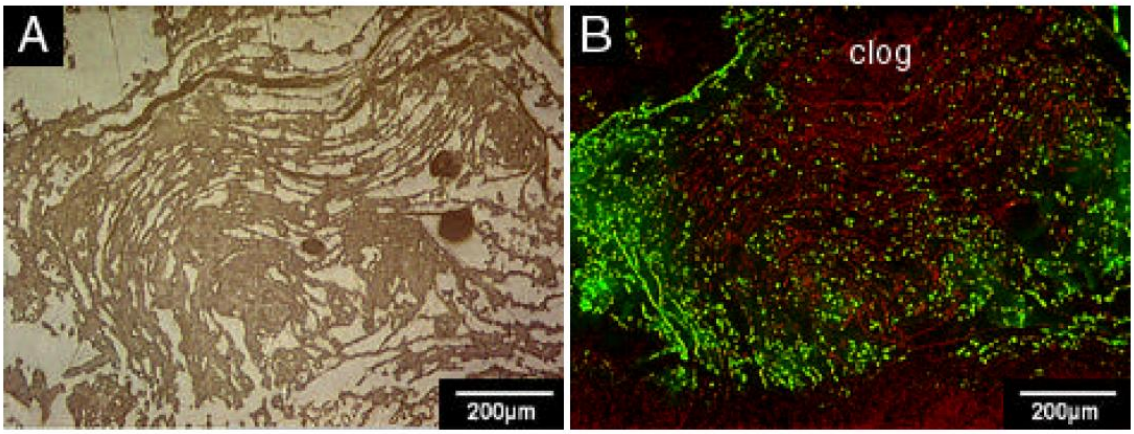

Figure 1.11: Reflected light (A) and CL images (B) of powdery deposits along the inside a post-mortem submerged entry nozzle. From [123].

is visible, but is a single color which seems to indicate that only one phase is present. However, two distinct phases are visible in the CL image (B): spinel (green) and corundum (red).

Each phase has a distinct color, allowing it to be distinguished from the surrounding area. Most transition metal ions and rare earth elements are activators that emit photons in the visible range when excited by electrons. However, iron typically will poison the CL

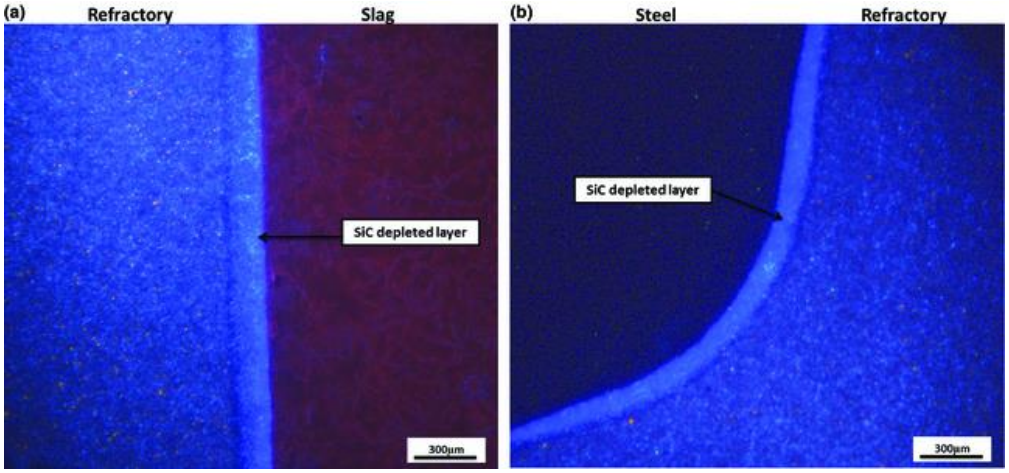

Figure 1.12: Refractory corrosion samples at the (a) refractory-slag interface and at (b) the refractory-steel interface. From [126].

process, causing no color to be seen in phases with high iron concentrations. [122] The effect of iron on CL can be observed in refractory corrosion tests by A. Kumar et al. in Figure 1.12. [126] Image (a) contains some faint coloration in the slag layer, which contains CL active oxides. However at the steel-refractory interface in (b) no CL is observed in the steel layer due to the high iron content. CL is a better used technique when iron is absent, but it can be used to observe the effect of iron on the surrounding refractory material.

1.6.1.2 Application of CL to mold fluxes. Aside from the papers presented in this thesis, only two references have specifically applied CL to mold fluxes. Microscopy results by E. Paransky et al. suggest that CL may be applied to mold fluxes and is effective for distinguishing between glassy regions and crystalline regions. [127] The authors suggest that CL may be used to determine the kinetics of crystalline layer growth, however the technique used is not clearly identified. However they note the difference in morphologies and stark contrast between phases. The authors recommend using this method in conjunction with image analysis software to better analyze the percentage of phases.

Researchers at Arcelor Mittal and Stollberg USA used CL to better visualize the chemistry changes in the mold powder while casting AHSS. [87] They cast high aluminum TRIP steels using a few lime-silica and lime-alumina mold fluxes and studied the chemistry changes, crystallization behavior, and slab surface quality. Lime-silica fluxes had an orange-yellow tinge in CL images and tended to precipitate CaF_2, resulting in a layered structure. As shown in Figure 1.13, the lime-alumina fluxes started as a blend of navy and greenish layers, but as the residence time in the mold increased, the colors progressed to a bright blue and pink, indicating a significant chemistry change. [87] These authors employed CL to visualize the crystallization behavior across the entire mold gap and were able to determine which powder minimized steel surface defects and retained desired properties. [87]

1.6.2. Quantitative XRD. X-ray diffraction (XRD) is a structural technique that is often used to determine what crystalline phases are present in a specimen. Each crystalline phase has a specific "fingerprint," a set of peaks that corresponds to the d-spacings present in the material. When multiple phases are present, it becomes more difficult to resolve which peaks belong to which phase. Software analysis has made it easier to match a specimen pattern with standard patterns. Relative peak heights of each phase does not

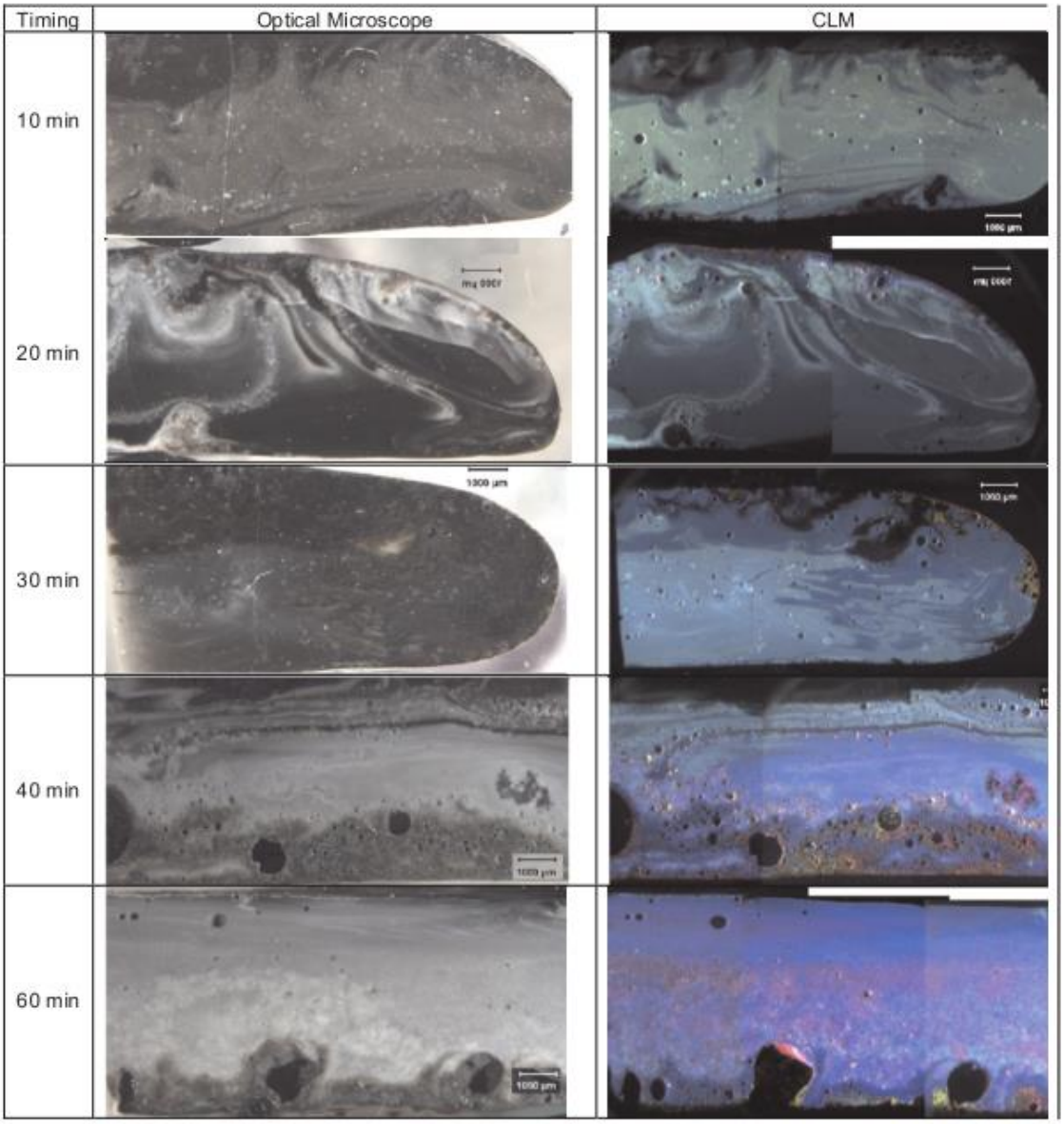

Figure 1.13: Optical and CL images of an advanced high strength steel mold flux film at various time during the alumina-silica exchange reaction in the mold.

correlate linearly to the percentage of each phase present. [128] Therefore in order to quantify the percentage of each phase present a different method is needed.

1.6.2.1 Methods. Cullity outlines three methods to quantify a multiphase sample: an external standard, direct comparison, and an internal standard. [128] The external standard method involves measuring a pure specimen of one of the phases present in the

material to determine a normalization constant that is related to the conditions of the instrument. The intensity ratio of a material containing phase α to pure α ($I_\alpha/I_{\alpha p}$) can be solved for using a complex relationship between the weight fractions, densities, and absorption constants. [128] Typically the relationship between $I_\alpha/I_{\alpha p}$ is not linear, therefore a calibration curve can be made by testing the pure standard against synthetic mixtures of the two phases in different ratios as shown in Figure 1.14.

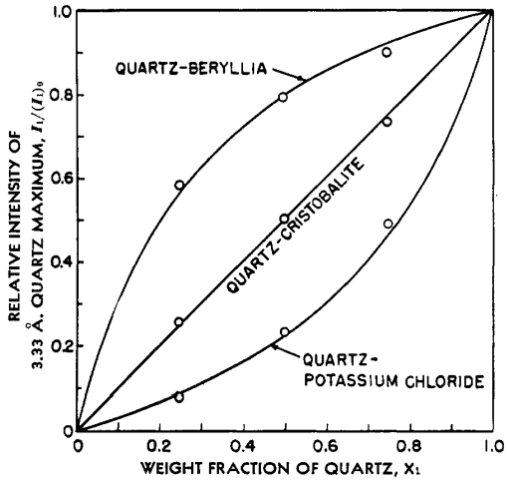

Figure 1.14: Calibration curve for quartz with berryllia, cristobalite, and potassium chloride using pure quartz as an external standard. From [129].

The external standard method is beneficial because it is an indirect method and does not contaminate the sample. However this method can be difficult to implement because the mass absorption coefficient must be accurately measured for the sample and standard. Additionally this method cannot correct for microabsorption errors. Measurements on the pure standard will have to be repeated to compensate for the ageing of the tube as well as configurational changes in the instrument.

The direct comparison method does not require a sample of a pure phase because another phase in the mixture becomes the reference line. This method works particularly well for materials such as iron that have two or more phases with the same composition,

but different structures. In this case the diffracted intensity equation of the two phases, γ and α, are related by:

$$\frac{I_\gamma}{I_\alpha} = \frac{R_\gamma c_\gamma}{R_\alpha c_\alpha} \tag{32}$$

where I is the X-ray line intensity of each phase, c is the concentration of each phase, and R is a constant that depends on θ, hkl, and the material. Using this equation and the pattern, the value of c_γ/c_α can be determined. For a material like iron the two (or three) phases make up the entirety of the phases present, therefore using Equation 33, the percentage of each phase can be determined.

$$c_\alpha + c_\gamma\ (+c_C) = 1 \tag{33}$$

The parenthesized portion of Equation 32 is included only if a third phase, C, is present. In the case where a third phase is present an additional relation between either α or γ and C will be necessary. The direct comparison method works well for metallurgical samples where the total concentration of phases will add to one (i.e. no amorphous content).

The internal standard method mixes a known quantity of a pure standard into the sample. This standard is related to phases in the material by:

$$\frac{I_A}{I_S} = K\frac{c_A}{c_S} \tag{34}$$

where A refers to the phase in the sample, S is the standard, and c is the weight percent of each phase. K is a constant that relates the two phases together. If corundum is used as the standard the Reference Intensity Ratio (RIR) value takes the place of K and is typically reported in all standard patterns. Since a single peak is used to determine the weight percentage of each phase, the results may be skewed due to preferential orientation or sample absorption. When peaks overlap, the intensity of a peak is difficult to extract.

All three methods described above are accepted methods to quantify XRD patterns. However since the development of computers, more sophisticated computer software has

been developed to account for complex phenomena that can affect the peak height, broadening, and shifts in peak location.

1.6.2.2 Reitveld analysis. Developed by H. M. Reitveld in 1969, this method uses a computer to more comprehensively analyze the full diffraction pattern. [130] The Reitveld method applies a least-squares refinement until the best fit is obtained between the entire sample pattern and the calculated pattern. The calculated pattern can be refined using crystal structure models, diffraction optic effects, instrumental factors, and other specimen characteristics. [131] The user plays a vital role in Reitveld refinement. The user must determine all phases present in the pattern and throughout the refinement process apply various portions of the model. The order in which parts of the model are applied will affect the quantification results. The user must be sure that the model makes physical and chemical sense.

1.7. PURPOSE STATEMENT

The goal of this research is to characterize the morphology of commercial mold fluxes through flux film sampling at industrial companies. Those structures will then be replicated in the laboratory using both primary cooling and secondary isothermal aging techniques. These methodologies will be applied to several mold powders with different composition. Additionally the relationship between the mold flux film structure and mold thermal behavior will be investigated at manufacturing sites with instrumented molds to understand the effect of mold flux morphology and thermal history on the overall heat transfer.

2. METHODOLOGY

2.1. INDUSTRIAL MOLD FLUXES

Industrial sponsors supplied mold powders with a variety of chemistries for the testing procedures outlined in Sections 2.2 and 2.3. All mold powders were carbon coated, spray dried, and granulated; chemistries as measured by the manufacturer using XRF are listed in Table 2.1. Powders were calcined prior to employing either testing method to reduce melting time. All samples were calcined at 600°C for three hours and stirred periodically.

Table 2.1: Industrial mold flux compositions in weight percent (R=Na, K, Li). Basicity is the ratio of lime to silica in the mold powder. A sample name was given to each mold powder to avoid disclosure of the supplier.

Sample Name	MgO	Al_2O_3	MnO_2	R_2O	F	B_2O_3	ZrO_2	TiO_2	Fe_2O_3	Basicity
G1	3	6		18	9	<1				0.8
G2	3	6		17	9					0.8
G3	2	5	2	13	10		2			0.92
G4	3	4	2	13	10		2			0.83
H1	2	5		10	4					1.16
H2	4	3		14	9					0.77
H3	4	11		14	9					0.77
H4	2	5		11	9					0.92
S1	<1	4		8	6					1.06
S2	1	6		4	7					1.09
S3	<1	5		8	5					0.98
S4	2	5		7	7					1.25
D1	2	4	0	11	8					0.99
D2	1	4	0	11	9					1.18
D3	2	3		10	8					1.12
D4	1	3	0	11	9					1.15
D5	3	4	3	5	8					1.1
D6	2	4	2	5	8					1.2
D7	6	3	<1	14	11	2				0.9
D8	2	4		9	8					1.06
U1	2	<1	<1	15	13			<1	<1	0.72

2.2. PRIMARY TESTING

Approximately 55 grams of calcined powder were melted in air for 15 minutes at 1350°C in a graphite crucible. Molten glass was poured directly into an instrumented step chill mold (SCM). SCMs were designed to test eight different cooling rates by having eight cells with varying widths as shown in Figure 2.1. Cooling rate is dictated by the cell width, with the widest cell (top) having the slowest cooling rate and the thinnest cell (bottom) having the highest cooling rate. The dimensions of each cell are given in Table 2.2. Steps were instrumented with a grounded, 0.020" outer-diameter, K-type thermocouple at the center of the cell. A portable data logger (Graphtec midi logger GL 220) monitored temperature every 0.01 seconds.

(a) (b)

Figure 2.1: Configuration of small copper 8-step chill mold with (a) defined cell sizes and (b) thermal insulation and thermocouple instrumentation.

Table 2.2: Step chill mold cell dimensions.

Step	***1***	***2***	***3***	***4***	***5***	***6***	***7***	***8***
Width (mm)	25	20	16	12	8	6	4	2

Three mold configurations were used: a large water-cooled copper mold (water cooling can be turned on or off), a small copper mold (Figure 2.1), and a large steel mold. These configurations were used to modify the cooling rate from fastest to slowest respectively. The water-cooled mold and steel mold are the same molds referenced in [107]. Thermal data was smoothed using a weighted averaging scheme; thermal arrests were pinpointed by looking for a decreased cooling rate and a cooling acceleration of zero. For some chemistries thermal arrests were identified by extrapolating the slopes before and after the thermal arrest and identifying the intersection point.

Specimen were extracted from each cell of the SCM for characterization. Powder x-ray diffraction (XRD) was performed on a PANalytical X'Pert Pro Multi-Purpose Diffractometer with a Cu Kα x-ray source to determine whether the cell crystallized. Specimen from cells containing crystallized material were mounted in epoxy and polished to a 0.1μm finish. Microstructures were analyzed using cathodoluminescence (CL) microscopy (model 8200 MK II) and SEM/EDS using an ASPEX-PICA 1020.

2.3. ISOTHERMAL AGED TESTING

The isothermal tin bath quench and age methodology is outlined in the experimental procedure of Paper II. The paper specifically outlines the methodology for testing flux G2, but the isothermal testing set up was slightly modified for each mold powder. S1 corroded several stainless steel tubes and required a thin layer of graphite on the inside of the steel tube to prevent corrosion during melting.

Future experiments will be carried out on synthesized advanced high strength steel (AHSS) fluxes. The synthetic powders were batched to match the chemistries of dip samples extracted from a mold during the casting of a TRIP steel and are not granulated. Alumina content increased to nearly 30%, and the silica content decreased significantly. These fluxes require a higher melting temperature than 1350°C, therefore an induction furnace set up with graphite tubes was introduced, as shown in Figure 2.2, to achieve temperatures that exceed 1350°C with minimal fluorine loss. This testing set-up is able to achieve 1400-1700°C as measured by an optical pyrometer. Graphite can reduce silica, however no silicon peaks were observed when testing the glassy G2 flux at 1500°C. The testing procedure is still in the development stage.

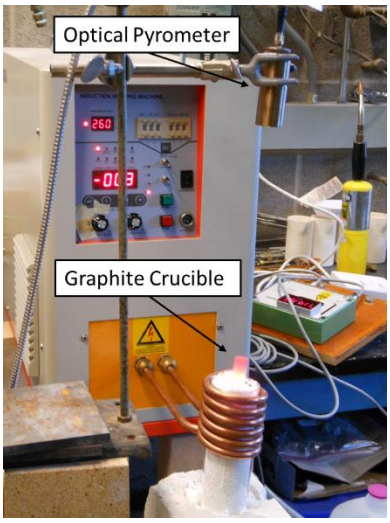

Figure 2.2: Induction furnace set up for melting AHSS fluxes.

2.4. XRD QUANTIFICATION METHOD

Specimens from each cell of all primary tests and all aged test samples were ground (-325 mesh) and analyzed via powder X-ray diffraction (XRD) on a PANalytical X'Pert Pro Multi-Purpose Diffractometer using a Cu Kα X-ray source for a standard thirty minute scan. Due to variations in the XRD source and overall set up, patterns generated on different days cannot be directly compared. Primary samples were not quantified, but were ran on the same day to compare the growing intensity of the peaks to confirm higher crystalline content in the larger cells. Aged samples at isothermal temperatures were run on the same day for direct comparison to one another.

The standard thirty minute scan is used to determine if the aged sample is glassy or crystalline. For crystalline samples, the phases present were determined (i.e. only cuspidine or cuspidine and nepheline etc.). Crystallized samples were scanned at a slower rate over the 24 to 31° two-theta angle range; then the area under the (221) cuspidine peak can be measured. It was assumed that the area under the peak was related to how much cuspidine was present. At an isothermal temperature, when no crystallization has occurred the area under the peak will be zero. When the maximum amount of crystallization occurred the

peak height will be the tallest. It was assumed that a linear relationship existed between these two points; the 1 hour sample must be quantified to fix the second endpoint.

The 1 hour samples were quantified by mixing 10 wt% of alumina standard with the sample and scanning over a 2 hour time period. The pattern was refined using the RIQAS Reitveld software. By fixing the alumina content, the software can more accurately estimate the amorphous content. The cuspidine content of all samples at an isothermal temperature was determined by using the area under the cuspidine peak and relating it to the area of the 1 hour (221) peak and the cuspidine content determined by Reitveld. For samples with more than just cuspidine present, the full pattern scan was refined by the Reitveld software to determine the crystalline phase distribution. This phase distribution totals 100% since the software cannot accurately determine amorphous content without a standard. The content of other phases was determined by using the percentage of cuspidine present in the sample; the remainder was assumed to be glass.

This method was confirmed for the 1 hour G2 sample at 700°C by comparing the quantitative XRD results to an area analysis of cuspidine in several regions; the results were reproducible within 3 wt%. However, treatment times less than 1 hour were not verified microscopically due to the heterogeneous nature of the crystal growth. The synthesis of cuspidine (procedure in Section 2.5) allowed for the validation of the Reitveld results. Glass was also batched and melted with a chemistry equivalent to 43% cuspidine removal as shown in Table 2.3. Cuspidine was mixed with the glass in known ratios: 10/90, 22/78, 30/70, and 43/57 respectively by weight percent; 10 wt% alumina standard was added for quantification purposes. Results determined experimentally through Reitveld analysis were compared to the known ratios of each mixture in Figure 2.3.

Table 2.3: Synthetic glass composition (wt%) based on G2 flux when 43 wt% cuspidine is removed.

CaO	SiO_2	MgO	Al_2O_3	Na_2O	CaF_2	Li_2O
0	45	5	13	25	02	10

Cuspidine batched in the 43/57 cuspidine-to-glass ratio was re-mixed and ran three times on the X-ray diffractometer to quantify the error associated with the instrument and Reitveld analysis. The standard deviation indicates variability up to 4 wt% between measurements. In addition, the trend of the experimental results is parallel to the theoretical 1:1 line. This suggests that Reitveld predicts the correct trend with increasing cuspidine content, but it underestimates the percent cuspidine present. This underestimation may be due to absorption effects or difficulty modelling the amorphous behavior. Based on the y-intercept of the trendline, it is suggested that 6 wt% is added to all Reitveld estimations of cuspidine content with a known amount of standard present.

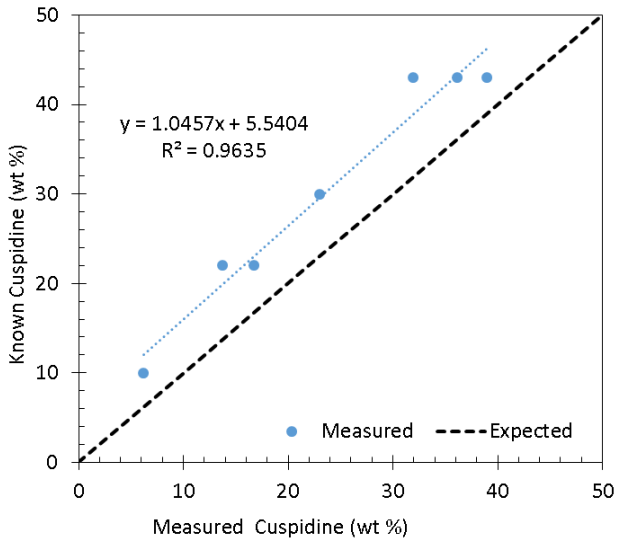

Figure 2.3: The known quantity of cuspidine plotted against the cuspidine content determined experimentally by Reitveld analysis.

2.5. SYNTHETIC CUSPIDINE

Cuspidine was synthesized to standardize XRD quantification. Rankinite ($Ca_3Si_2O_7$) was synthesized first by mixing 99+% pure $CaCO_3$ and SiO_2 in a 3:2 molar ratio. Powders were thoroughly mixed by adding alumina media and deionized water and ball milling for approximately 18 hours, then dried in a 110°C furnace. Powder was pressed into 5g, 1" diameter pellets. Pellets were fired in a Pt crucible at 1375°C for 10 hours, then

removed immediately from the crucible and allowed to cool. Room temperature samples were stored under vacuum and Rankinite was confirmed via XRD.

Rankinite pellets were ground and equimolar amounts of rankinite and CaF_2 were mixed together. One gram of the mixed powder was pressed into ½" diameter pellets. Several pellets were stacked in a larger Pt crucible for firing. A smaller Pt crucible was placed upside-down over the top of the pellets to act like a lid. The furnace was preheated to 900°C and then the pellets were placed in the furnace. After 4 hours of sintering, the pellets were removed and quickly cooled in air. The bottom pellet was discarded and top pellets were characterized to confirm the formation of cuspidine. Excess CaF_2 was also found in the XRD pattern. For quantification purposes, a small portion of the cuspidine sample was mixed with 25 wt% NIST Alumina standard and analyzed via XRD. The pattern was then run through the Reitveld program to confirm the percent cuspidine present in the sample, fixing the alumina content at 25 wt%. Results showed that less than 3 wt% CaF_2 was present in the cuspidine. An unsuccessful second attempt to make cuspidine was made in another furnace at 900°C. This suggests the controller and the actual temperature of the furnace initially used differ. Based on the difference measured by a separate thermocouple above 1300°C during the 10 hour Rankinite firing, it is suspected that the furnace was up to 75°C above 900°C when cuspidine was made.

3. SUMMARY OF PAPERS

PAPER I: Application of Cathodoluminescence in Analyzing Mold Flux Films

Paper I was submitted and presented at the 10th International Conference on Molten Slags, Fluxes, and Salts in Seattle Washington, May 2016. Flux film samples were extracted from a funnel mold in an industrial thin slab caster. Accompanying thermocouple data was analyzed to relate morphological structures to the heat removal measured in the mold. It was determined that in the high stress funnel region, the flux film would fracture and withdraw, briefly leaving an air gap which lowered the regional heat removal. Glass would re-infiltrate the region, increasing the heat transfer to a local maxima. As the glass solidified and crystallized, the heat transfer would slowly decrease. The repetition of this thermal cycling leads to what is coined as "saw tooth" behavior. Using conventional techniques for mold flux characterization, it would be difficult to view this behavior. By employing cathodoluminescence high resolution images of the entire cross section of the flux film were taken at low magnification. This method is recommended for further study of flux films.

PAPER II: Investigation of Mold Flux Crystallization by Rapid Quenching and Isothermal Aging in Molten Tin

Paper II was submitted and accepted for presentation at the AISTech 2017 conference in May 2017. "Quench and age" experiments were performed on a specified mold flux chemistry at 500 to 800°C for 0.5, 1, 2, 4, 8, 16, 32, and 60 minutes. Specimen were melted at 1350°C for 1 minute and quenched at a rate greater than the critical cooling rate to an isothermal temperature. XRD and microscopy showed that crystallization rates leveled off at 32 minutes to 1 hour for all temperature. Three phases were observed: cuspidine, nepheline, and lithium silicate. Comparison of quench and age microstructures with those of the flux film indicated similar faceted morphologies. Continuous cooling experiments yielded only dendritic structures and cuspidine crystals. Since the majority of the flux film structure is non-dendritic and contains nepheline, the structures in the flux film could not have formed by continuous cooling and instead formed by devitrification.

PAPER

I. APPLICATION OF CATHODOLUMINESCENCE IN ANALYZING MOLD FLUX FILMS

Elizabeth Nolte[1], Jeffrey D. Smith[1], Michael Frazee[2], Neil Sutcliffe[2], Ronald J. O'Malley[1]

[1]Missouri University of Science and Technology
238 McNutt Hall, 1400 N. Bishop Ave., Rolla, MO, 65401, USA

[2]Nucor Steel Gallatin
4831 US Highway 42 West, Ghent, KY, 41045, USA

ABSTRACT

Mold fluxes are used in continuous casting of steel to control heat transfer from the steel shell to the copper mold based on their structure and properties. Structures observed in mold flux film samples extracted from conventional and thin slab continuous casters at the end of a cast were examined using cathodoluminescence (CL) imaging in conjunction with XRD and SEM/EDS analysis. Glassy and crystalline structures in the flux films varied greatly depending on sampling location in the mold, distance from the mold wall and the mold flux being examined. Temperature data collected from thermocouple arrays in a thin slab funnel mold indicated saw-tooth temperature fluctuations in the lower area of the funnel region, presumably due to cyclic fracture and regrowth of the mold flux crystalline layer in that region of the mold. The temperature observations correlate well with the structures observed in the flux film samples from the region. CL microscopy clearly distinguishes glassy regions from regions with devitrified and dendritic crystal growth, as well as continuous and fractured crystallite layers and cuspidine and nepheline phases that are present. The technique also highlights small variations in Mn oxide content in the glassy region of the flux that results from exchange reactions with the steel, making flow lines in the previously liquid portion of the flux film clearly visible. The benefits of applying cathodoluminescence imaging to the analysis of mold flux films in continuous casting are discussed.

1. INTRODUCTION

Mold flux is critical for regulating mold heat flow and controlling slab surface quality in the continuous casting process [1, 2, 3]. The crystalline structure that forms in the mold flux film in the mold gap region of the continuous caster plays a significant role in the performance of a mold powder for a given steel grade and caster (Figure 1.1).

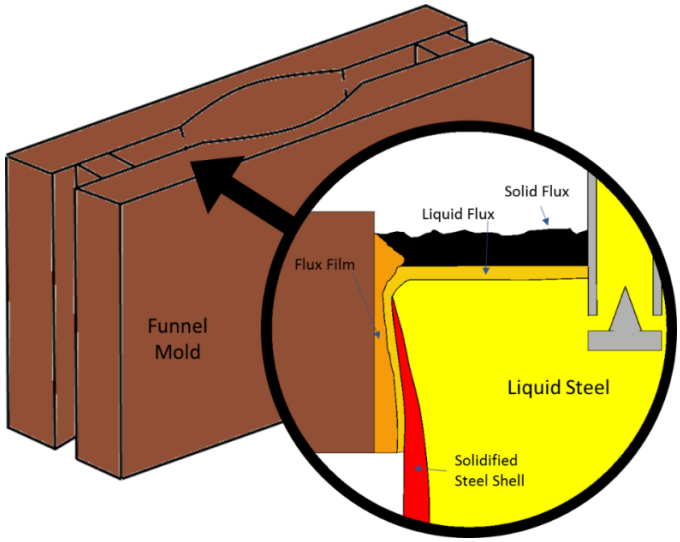

Figure 1.1: Schematic of the funnel mold and the cross section of the mold.

Mold powders are often selected based on their viscosity and primary crystallization temperature even though the crystallite phases and morphologies that are observed in the mold gap generally do not form by the primary crystallization path [4]. The crystalline layers that are observed in the mold gap have been found to form by devitrification of the super-cooled glass layer that remains in contact with the caster mold well beyond the residence time of the steel shell [4,5]. The phases and structures formed by devitrification have a strong influence on the mold thermal behavior through their influence on the crystalline layer's resistance to shear and fracture in the mold gap. Crystalline film fracture and reformation appears to be a primary cause of periodic temperature and heat transfer fluctuations in the mold [4]. Techniques such as: (DSC) [6-8], (DTA) [9-11], (SHTT) [6,12-14], and (DHTT) [14], can be used to characterize mold

flux. However, these techniques rely on simulating only a small portion of the mold environment. Cathodoluminescence (CL) analysis has been a standard technique for geological materials for 30 years, but in the last 20 years has been developed as an effective method to observe refractory corrosion. [15] This paper will discuss the application of cathodoluminescence analysis to the investigation of crystallization behavior for industrial flux films, in conjunction with (XRD) and (SEM).

2. EXPERIMENTAL PROCEDURE

Flux film samples were extracted from the funnel mold of a thin slab caster at the end of a cast. The flux composition, as reported by the supplier, is recorded in Table 2.1.

Table 2.1. Composition of mold flux in wt% (R=Na, K, Li).

Basicity	MgO	Al_2O_3	ΣR_2O	F
0.8	2.6	5.9	16.5	8.6

Specimens were analyzed using powder x-ray diffraction (XRD) on a PANalytical X'Pert Pro Multi-Purpose Diffractometer with a Cu Kα x-ray source. Specimens were mounted in epoxy and polished to a 0.1μm finish. Crystallite structures were analyzed using cathodoluminescence (CL) microscopy (model 8200 MK II) and SEM/EDS using an ASPEX-PICA 1020.

3. RESULTS & DISCUSSION

Many of the flux film samples exhibited a crystalline layer on the mold wall side of the film as reported elsewhere [5,24,25]. Samples obtained from lower in the funnel also exhibited fractures in the crystallite film, and areas that were almost fully glassy. Figure 3.1 shows the variation in the flux film appearance as the sample location progressed lower into the funnel.

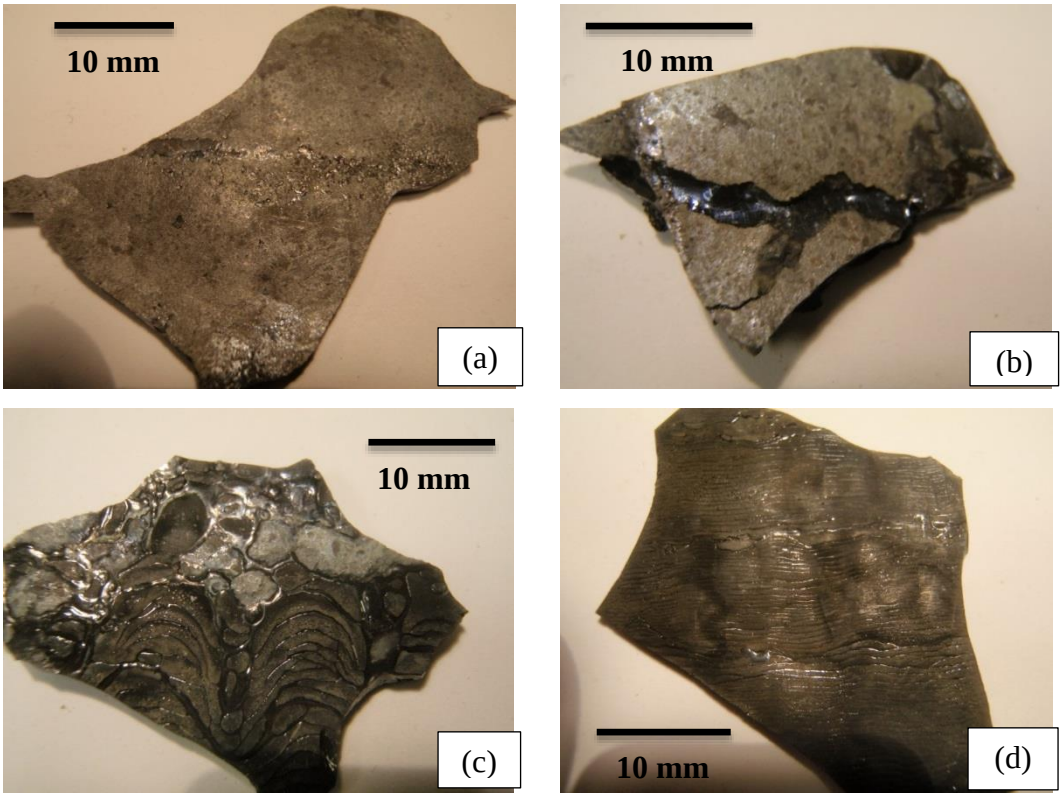

Figure 3.1: Flux film samples from upper funnel area (a) to lower funnel area (d) - Mold side.

Figure 3.1 (a) and (b) are primarily crystalline with very little glass infiltration except along a large crack in (b). Figures 3.1 (c) and (d) are glassy and show longitudinal striations across the face. This structure is believed to result from crystalline layer fracturing and re-filling with glass. This behavior is consistent with thermal data collected from an instrumented funnel mold, where temperature was monitored at several locations both within and outside of the funnel region. Large saw tooth shaped fluctuations in temperature (± 45°C) were evident within the high-stress funnel region (Figure 3.2a). The rapid temperature decrease is associated with crystal fracture and removal, while the rapid temperature increase is associated with glass infiltration in the fractured region. The slow drop in temperature is associated with aging and crystallization of the glass. Outside of the funnel region, smaller (± 10°C) temperature fluctuations were evident (Figure 3.2b).

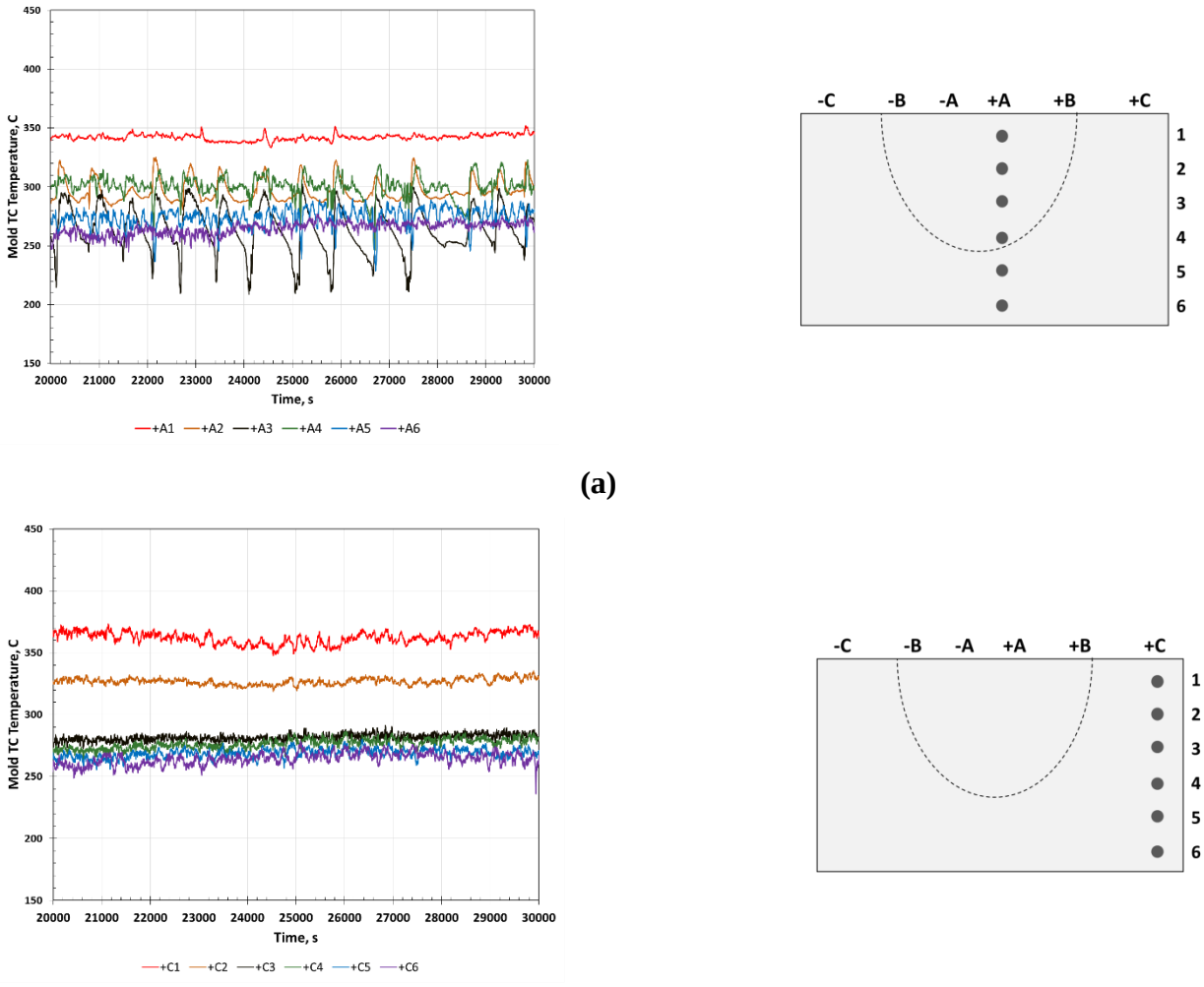

Figure 3.2: Inside the funnel area (a) exhibits saw tooth behavior, where temperature fluctuates on a semi-regular basis with respect to time. Outside the funnel area (b), temperature fluctuations are mild (± 10°C). Corresponding diagrams indicate thermocouple locations in the funnel mold.

CL imaging proved to be a valuable method for identifying crystalline phases and structure in polished flux film samples. Figure 3.3 shows a cross section of a flux film from lower in the funnel area. The yellow and bright orange regions are crystalline and the light orange regions are glassy. The crystalline layer on the mold side of the flux film is fractured. The flow lines in the glassy region suggest that glass flowed and infiltrated the

fracture region. The structures in the CL image support the theory of crystalline fracture and backfilling with glassy material by the mechanism proposed in Figure 3.4.

The variation in shades in the darker orange region opposite the mold highlights the flow lines in the glassy region of the flux film that was fluid during casting. The color

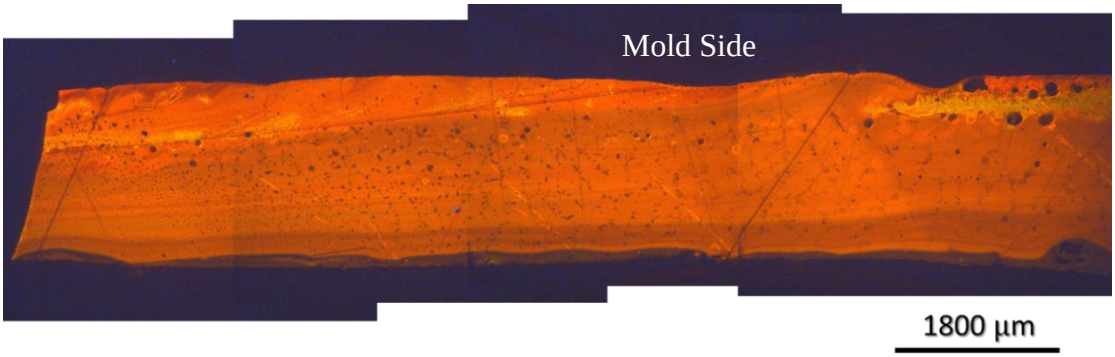

Figure 3.3: CL image of flux film sample – lower funnel region.

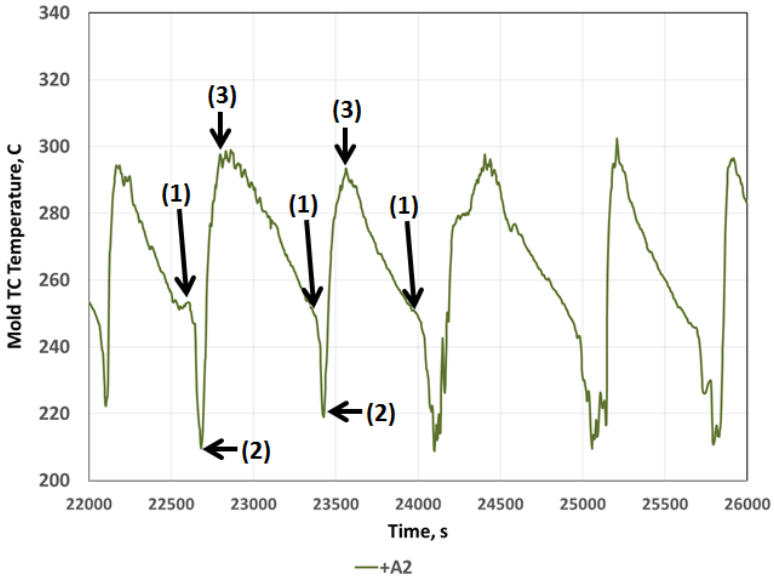

Figure 3.4: Proposed origin of saw tooth temperature fluctuations: (1) fracture of flux crystalline film, (1→2) withdraw of flux crystalline film, (2) air gap, (2→3) inflow of glass, (3) complete glass infiltration, (3→1) aging and crystallization of glass.

variations are directly related to variations in manganese oxide content in the flux that was picked up during casting from interaction of the mold flux with the molten steel. Figure 3.5 documents this pickup. These variations in manganese oxide level were also documented using SEM/EDS analysis.

XRD analysis of the flux films shows both the cuspidine and the nepheline phases are present in the flux film. The presence of nepheline in the crystalline layer suggests that this layer formed by devitrification of a super-cooled glass and not by primary crystallization [1, 9]. Devitrification follows a cooling path achieved by cooling faster than the critical cooling rate, avoiding crystallization, and isothermally holding at a temperature. In flux films, nepheline can only be formed through devitrification [9]. Its presence suggests that a super-cooled glass layer that remains in contact with the caster mold well beyond the residence time of the steel shell [1]. The distribution of cuspidine and nepheline in the crystalline layer can be seen more clearly in the CL image in Figure 3.6(a), cuspidine being yellow and nepheline being brown. These phases were also confirmed by SEM EDS analysis, Figure 3.6(b).

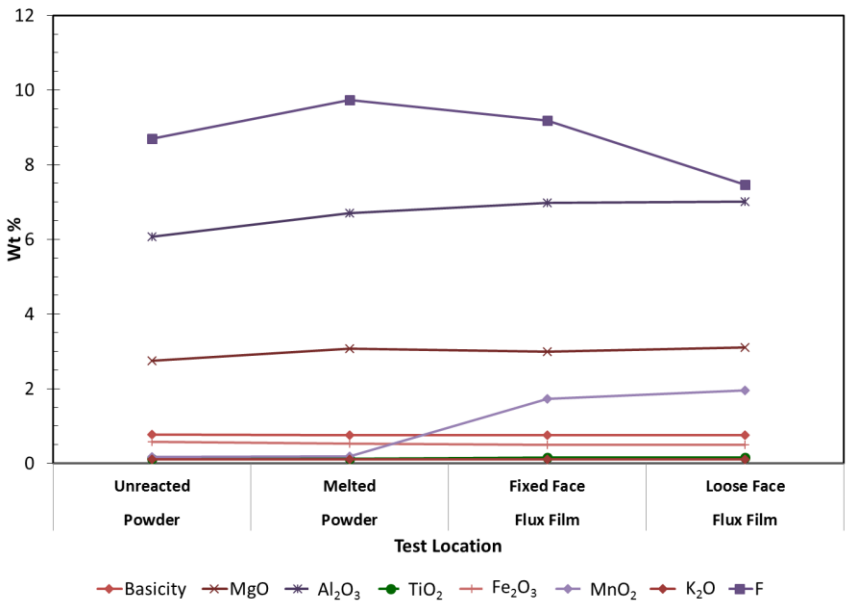

Figure 3.5: Flux film chemical analysis indicating manganese oxide pickup in mold flux.

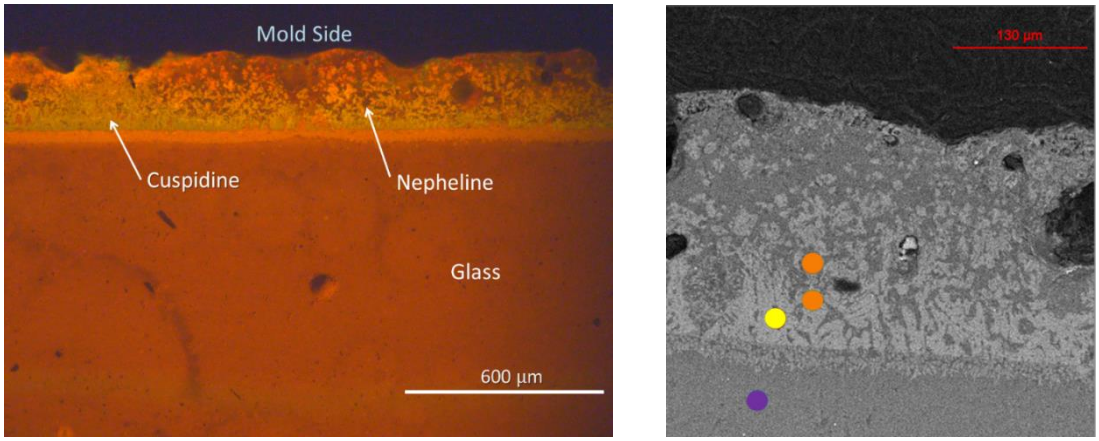

(a) (b)

Figure 3.6: CL image (a) and SEM image (b) of the crystal growth along the mold wall. In (b) orange is nepheline, yellow is cuspidine, and purple indicates the bulk glassy region.

CL images best show the morphology and crystallites present. The cuspidine (yellow-orange) appears to co-crystallize with nepheline (dark orange) along the mold face. The crystal structures in the flux film change based on distance from the mold wall. Along the mold wall both cuspidine and nepheline have crystallized as small equiaxed crystals. As the temperature increases with distance away from the mold wall, the nepheline crystals do not appear to form as readily and the cuspidine crystal concentration increases. This forms a dense crystalline layer approximately 200µm from the mold wall. EDS confirmed the compositions of the crystals. In Figure 3.6(b) the orange region indicates nepheline, yellow is cuspidine and purple is the bulk glass where the Ca to Si ratio is approximately 1:1.

Although the nepheline and cuspidine phases can both be distinguished in the SEM image, it is much easier to visualize the crystallization of cuspidine and nepheline using CL analysis. In addition, small variations in manganese oxide content in the glass can be easily observed.

4. CONCLUSIONS

Flux films have widely varying structures based on distance from the mold wall and position in the mold. Information on these structures can be obtained by carefully extracting flux films at the end of a cast sequence and analyzing their microstructure. Cathodoluminescence imaging allows different structures to be observed more readily than by SEM analysis. This technique makes variations in the content of transition metal oxides in the flux film readily visible. Flux film structures can also vary significantly within a funnel mold. Flux film samples from high stress regions in the funnel area are observed to have fracture and glass re-infiltration marks that match the saw tooth temperature behavior in these regions. The following specific conclusions are made based on these experiments:

Large fluctuations in temperature on the mold side of the flux film are observed in the funnel region. In addition, glassy striations are observed on the mold face side of the flux film suggesting that the flux film repeatedly fractures, dropping the mold temperature sharply on initial withdrawal of the crystalline layer and then increasing temperature sharply when new glass infiltrates the fractured region. Following infiltration, the mold temperature then drops slowly as the re-infiltrated glass ages and crystallizes. This mechanism explains the observed periodic saw tooth mold temperature behavior.

Cathodoluminescence is a useful tool for studying flux films. It provides high resolution at low magnification, so phases can be easily distinguished optically and other small details can be observed that may have been missed using other techniques. It provides better visualization the distribution and type of crystal structures than SEM analysis and can also be used to observe small variation in composition in the bulk glass regions. Therefore, use of CL in analyzing flux films is recommended.

REFERENCES

1. K.C. Mills, “Mold Fluxes for Continuous Casting and Their effect on Product Quality”, McLean Symposium, Proc., ISS, Toronto, Canada, 1998, pp. 195-201.
2. K. Ichikawa, A. Morita, Y. Kawabe, “Behavior of Powder Slag Film and Influence of Powder Slag Film on Mold Heat Transfer Rate”, Shinagawa Technical Report, Vol. 36, pp. 99-107, 1993.
3. K. Watanabe, M. Suzuki, K. Murakami, H. Kondo, A. Miyamoto, and T. Shiomi, “The Effect of Mold Powder Crystallization on Heat Transfer in Continuous Casting Mold”, NKK Technical Review, No. 77, 1997, pp. 20-26.

4. R.J. O'Malley , "Observations of Various Steady State and Dynamic Thermal Behaviors in a Continuous Casting Mold", Proc. 82nd Steelmaking Conf., ISS, Chicago, IL, March 21-24, 1999.
5. Y. Meng and B.G. Thomas, ''Simulation of Microstructure and Behavior of Interfacial Mold Slag Layer in Continuous Casting of Steel'', ISIJ Int., 46, 2006, pp. 660-669.
6. Y. G. Maldonado et al., "Estimation of Time-Temperature-Transformation Diagrams of Mold Powder Slags from Thermo-analysis of Non-isothermal Crystallizsation," *Met. And Mat. Trans. B,* (2014).
7. M.-D. Seo, C.-B. Shi, J.-W. Cho, and S.-H. Kim, "Crystallization Behaviors of CaO-SiO 2 -Al 2 O 3 -Na 2 O-CaF 2 - (Li 2 O-B 2 O 3) Mold Fluxes," (n.d.).
8. M.-D. Seo, C.-B. Shi, H. Wang, J.-W. Cho, and S.-H. Kim, "Non-isothermal melt crystallization of cuspidine in CaO–SiO 2 –CaF 2 based glasses," *J. Non. Cryst. Solids*, **412** 58–65 (2015).
9. Y.G. Maldonado, F.A. Acosta, A.H. Castillejos, and B.G. Thomas, "Kinetic Study of the Devitrification of Mold Powder Slags," *AISTech*, 11 (2012).
10. R. Carli and C. Righi, "Mould flux crystallization : A kinetic study," *VII Int. Conf. Molten Slags Fluxes Salts*, [Mm] 821–826 (2004).
11. Z. Wang et al., "Crystallization Kinetics and Structure of Mold Fluxes with SiO_2 Being Substituted for Casting of Titanium Stabilized Stainless Steel," *Met. And Mat. Trans. B,* 44 606-612 (2013).
12. J. Li et al., "A Kinetic Study of the Effect of Na_2O on the Crystallization Behavior of Mold Fluxes for Casting Medium Carbon Steel," *ISIJ Int.*, 52 [12] 2220-2225 (2012).
13. B. Jiang et al., "A Kinetic Study of the Effect of ZrO_2 and CaO/Al_2O_3 Ratios on the Crystallization Behavior of a CaO- Al_2O_3-Based Slag System," *Met. And Mat. Trans. B,* 45 1057-1067 (2014).
14. Y. Kashiwaya, C.E. Cicutti, A.W. Cramb, and K. Ishii, "Development of Double and Single Hot Thermocouple Technique for in Situ Observation and Measurement of Mold Slag Crystallization.," *ISIJ Int.*, **38** [4] 348–356 (1998).
15. M. Karakus and R. E. Moore, "Cathodoluminescence (CL) Microscopy Application to Refractories and Slags", Journal of Minerals & Materials Characterization & Engineering, Vol. 1, No. 1, 2002, pp. 11-29.
16. R.B. Tuttle, K.D. Peaslee and J.D. Smith, "Interaction of Molten Ultra Low Carbon Steel with Carbide and Nitride Refractory Materials", Refractories Applications Transactions, **3** [1] 101-108 (2007).
17. L. Trueba, K.D. Peaslee, J.D. Smith and M. Karakus, "Effect of Nozzle Base Material on the Rate of Clogging during the Continuous Casting of Aluminium-killed Steels," Steel Research International, **77** [1] 37-47 (2006).

18. S. Ramachandran, K.D. Peaslee and J.D. Smith, “Thermochemistry of Steel-Refractory Interactions in Continuous Casting Nozzles,” ISS Transactions, September 2003, 55-63 (2003).

19. M. Karakus, J.D. Smith and K.D. Peaslee, “Study of Non-Metallic Inclusions in Continuously Cast Steel Using Cathodoluminescence Microscopy,” 38th Annual Meeting of the St. Louis Section of the American Ceramic Society, Chesterfield, MO, 201-212 (2002).

20. M. Karakus, J.D. Smith and R.E. Moore, “Cathodoluminescence Mineralogy of used MgO-C Bricks in Basic Oxygen Furnaces,” Veitsch-Radex Rundschau, **1** 24-32 (2000).

21. J.D. Smith, K.D. Peaslee, M. Karakus and L. Trueba, “Study of Continuous Casting Nozzle Clogging Using Cathodoluminescence Microscopy,” Advances in Refractories for the Metallurgical Industries III, eds. C. Allaire and M. Riguad, 187-200 (1999).

22. J.D. Smith, K.D. Peaslee, M. Karakus and H. Ruiz, “Post Mortem Analysis of Foundry EAF Refractories,” 53rd Technical and Operating Conference, Steel Founders’ Society of America, Chicago, IL, (1999).

23. M. Karakus, J.D. Smith, and R.E. Moore, “Mineralogy of the Carbon Containing Steelmaking Refractories,” UNITECR ‘97, New Orleans, LA, **2**745-754 (1997).

24. R.J. O’Malley and J. Neal, ‘‘An Examination of Mold Flux Film Structures and Mold gap Behavior Using Mold Thermal Monitoring and Petrographic Analysis at Armco´s Mansfield Operations’’, METEC Congress 99, Dusseldorf, Vol. 1, 1999, pp.188-195.

25. W. Yan, W. Q. Chen, C. Lippold, H. G. Zheng, “Structure and performance characteristics of mold flux films for continuous casting of special alloy steels”, La Metallurgia Italiana - n. 11-12/2013, pp. 35-42.

26. Y. Kashiwaya, C. Cicutti, A. Cramb, “Crystallization Behavior of Mold Slags”, ISS Steelmaking Conference Proc., Vol. 81, pp. 185-191, 1998.

27. Grieveson, P., Bagha, S., Machingawuta, N., Liddell, K. and Mills, K.C. 1988: ‘Physical properties of casting powders: Part 2 Mineralogical constitution of slags formed by powders’, Ironmaking and Steelmaking Vol.15 No.4, pp. 181-186.

II. INVESTIGATION OF MOLD FLUX CRYSTALLIZATION BY RAPID QUENCHING AND ISOTHERMAL AGING IN MOLTEN TIN

E. I. Peterson, T. P. Sander, J. D. Smith, and R. J. O'Malley

Missouri University of Science and Technology
220 McNutt Hall, 1400 N. Bishop, Rolla MO, 65401
Phone: (573) 341-4711
Email: einyt3@mst.edu

Keywords: TTT diagram, Crystallization, Cuspidine, Nepheline, Industrial flux film

ABSTRACT

Crystallization behavior of a mold flux under conditions found in the mold gap of the continuous casting process was investigated. A laboratory technique that employs molten tin as the quench medium was utilized to "quench and age" molten flux samples to generate a time temperature transformation (TTT) diagram for nucleation and growth of crystallites from the molten mold flux. A commercial flux film sample of the same composition was extracted from a caster at cap-off. The phases, structure, and quantity of crystallites formed in the mold gap are compared to the crystal phases and structures observed in the "quench and age" experiments and with crystal structures formed in the lab by direct cooling and crystallization of the flux. The crystal phases and morphologies present in the extracted flux film compare favorably with the structures and phases observed in the "quench and age" experiments.

1. INTRODUCTION

Continuous casting relies on mold powder to control the heat transfer between the steel shell and the water-cooled copper mold. Proper heat transfer is critical to prevent surface defects and breakouts. [1] Heat transfer is controlled by the crystallization behavior of the mold flux in the mold gap. Despite the higher thermal conductivity of crystallized phases, heat transfer in the mold gap is controlled by radiation and interface roughness between the mold wall and flux film, thus glassy regions have higher heat transfer. [1-4] While it is recognized that heat transfer is an important property of the mold flux, it is

difficult to measure and is often not repeatable. [4] Therefore it is important to study the crystallization and subsequently correlate the crystal morphologies to the thermal behavior to understand what is happening in the mold gap.

Several methods have been used to study the crystallization behavior of mold fluxes. These include: differential scanning calorimetry (DSC) [6-8], differential thermal analysis (DTA) [7-14], confocal laser microscopy (CSLM) [15-17], single hot thermocouple technique (SHTT) [6, 12-14], and double hot thermocouple technique (DHTT) [14]. DSC and DTA identify phase transformations from changes in thermal behavior relative to a reference. These techniques are generally limited to non-isothermal studies, require small samples (< 1g), and have slow heating rates (~10°C/min). Small batch sizes increase the effect of volatile loss, such as fluorine. CSLM is a powerful technique that allows the crystallization behavior to be observed over time; however the microscope is expensive and has poor atmosphere control. Work by Cho et al. demonstrated that adding a quartz lid to the CSLM unit decreases fluorine loss, though the sample size is still small (0.07-0.12 grams). [15] SHTT and DHTT are also limited to small batch sizes (< 0.1g), but generally samples can be heated and cooled quickly to minimize fluorine loss. Sample transparency is a larger issue for SHTT and DHTT specimens as these techniques require visual observation of crystal formation. Components such as FeO, MnO, and TiO_2 are often excluded to increase transparency. [14] Yet these oxides can be important to the crystallization behavior; TiO_2 has been reported to act as a nucleating agent. [18]

An isothermal tin bath quench method has been developed to address some of the issues with the techniques discussed previously. This test was designed to accommodate larger sample sizes (~8 g), allowing powder X-ray diffraction (XRD) and microscopy to be performed. Since transparency is not a requirement for this test, industrial flux compositions that contain transition metal oxides can be tested. In this work, isothermal tests were performed at specified times and temperatures on an industrial mold powder. Crystallized phases were identified and mapped in a time-temperature-transformation (TTT) diagram and crystal morphologies were compared with industrial flux film samples.

2. EXPERIMENTAL PROCEDURE

Industrial mold powder (chemistry in Table 2.1) was calcined at 600°C for 3 hours, stirring periodically to facilitate carbon removal before melting. Small batches (~10g) were melted at 1350°C for ten minutes in a graphite crucible. Molten flux was rapidly quenched between two room temperature copper plates; glass formation was confirmed with XRD. The quenched glass was crushed using a hardened steel pin and die set. Stainless steel tubing (0.25" OD, 0.020" wall thickness) was crimped at one end and filled with the crushed glass. Specimens were melted by suspending them in a furnace for 1 minute at 1350°C and then rapidly transferring to, and quenching in, the tin bath held at a specified temperature. Specimens were aged for 0.5, 1, 2, 4, 8 16, 32, and 60 minutes in the tin bath. After isothermal aging, the specimens were water quenched to cool them rapidly to room temperature. A thermocouple was inserted into the stainless tube in one experiment to confirm complete melting of flux and to document the quench rates. The thermal profile of the test is presented as Figure 2.1. A maximum temperature of 1340°C was achieved, which is above the melting temperature (~1120°C, DTA) of the flux sample. The quench rates in the tin bath and in the water bath averaged 65°C/s and 30°C/s, respectively, and were adequate to avoid premature crystallization. A schematic of the tin bath quench system is included as Figure 2.2.

Table 2.1: Composition of mold flux in wt% (R=Na, K, Li).

Basicity	MgO	Al_2O_3	ΣR_2O	F
0.8	2.6	5.9	16.5	8.6

A diamond saw was used to section the stainless steel tubes, isolating the portion of the specimen that was immersed in the tin. Extracted samples were ground (-325 mesh) and analyzed via powder X-ray diffraction (XRD) on a PANalytical X'Pert Pro Multi-Purpose Diffractometer using a Cu Kα X-ray source. A Reitveld refinement method [19] was used to determine the quantity of each crystalline phase. Amorphous content of samples that were aged for 60 minutes at each test temperature was determined by doping

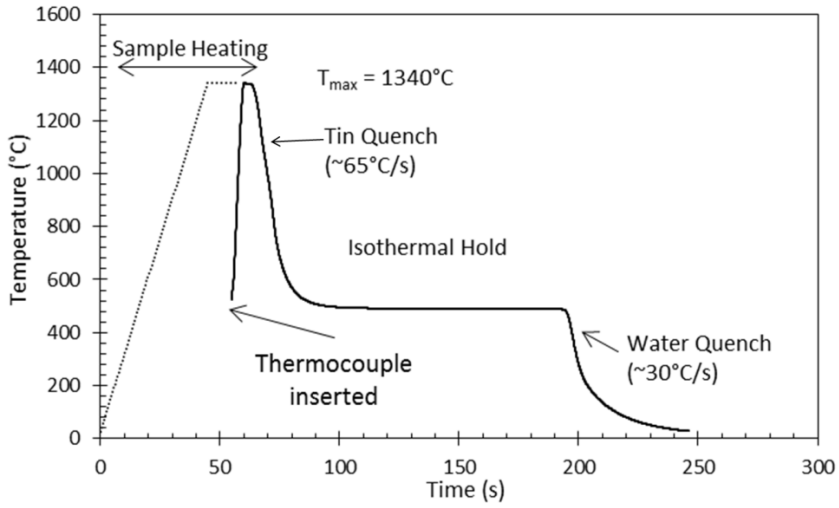

Figure 2.1: Thermal profile of aged test with isothermal hold for 2 minutes at 500°C. Dashed lines indicate estimated glass temperature prior to thermocouple insertion.

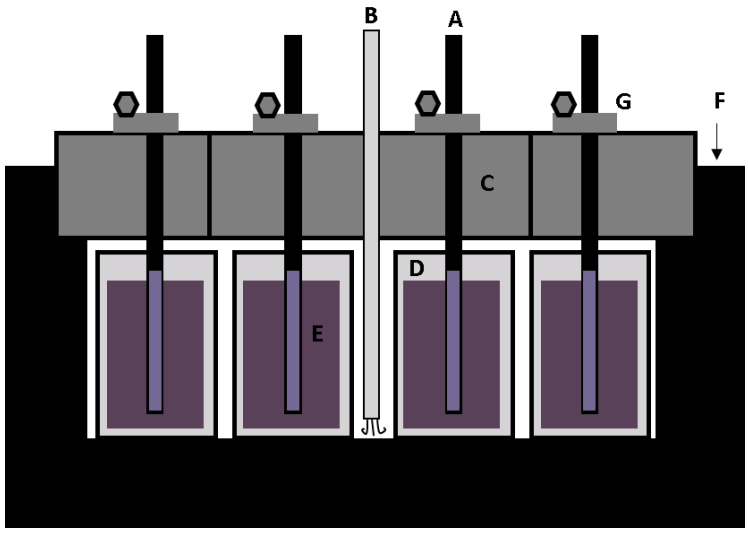

Figure 2.2: Schematic of isothermal tin bath quenching system. (A) are the specimens (x4), (B) argon input to reduce tin oxidation, (C) refractory lid, (D) crucibles containing tin, (E) tin bath, (F) is the resistance element furnace, and (G) are the specimen holders (x4) to suspend the sample in the bath away from crucible walls.

with 10 wt% of a NIST 676 alumina standard and measuring the X-ray pattern. This pattern was modeled using Reitveld software with the alumina peak constrained to 10 wt%. Subsequent spectra were acquired using a slow scan rate (0.0134°/s) in the 24-31° two-theta range and the integrated area under the 2-2-1 cuspidine peak was measured. The percentage of cuspidine was calculated using a linear relationship between the peak area and the amount of cuspidine present in the alumina doped samples. The percentage of other phases in the samples were determined using Reitveld software, scaled to the previously determined cuspidine content. Microstructures were examined using cathodoluminescence (CL) microscopy (model 8200 MK II) and SEM/EDS using an ASPEX-PICA 1020 and a Helios Nanolab 600 for higher resolution.

3. RESULTS & DISCUSSION

3.1. Generation of Quantitative TTT-diagram

SEM images of aged samples (Figure 3.1) show heterogeneously nucleated crystals along the tube wall. The transformed fraction increased with time, achieving complete transformation between 16 and 32 minutes for all temperatures. Two distinct phases were identified: cuspidine ($Ca_4Si_2F_2O_7$) and nepheline ($NaAlSiO_4$), which have been reported as common phases in literature. [1, 21] Additionally several peaks potentially correspond to a lithium silicate phase (Li_2SiO_3). However since it is difficult to distinguish lithium silicate from lithium in the bulk glass using most characterization techniques and less than 10 wt% forms, this phase could not be confirmed. Crystallization contour lines were drawn onto the time-temperature-transformation (TTT) diagram to indicate the total percentage transformed (Figure 3.2).

XRD results indicate that the first detectable crystalline phase was cuspidine. Nepheline and lithium silicate phases always formed after 10-30 wt% cuspidine was present and they often appeared together, suggesting that cuspidine may act as a nucleation site for nepheline and lithium silicate growth. However, at 700°C, nepheline was observed nearly 40 minutes earlier than lithium silicate. Complete transformation is achieved between 32 minutes and 1 hour and the weight percentage of all phases appears to stabilize (Figure 3.3).

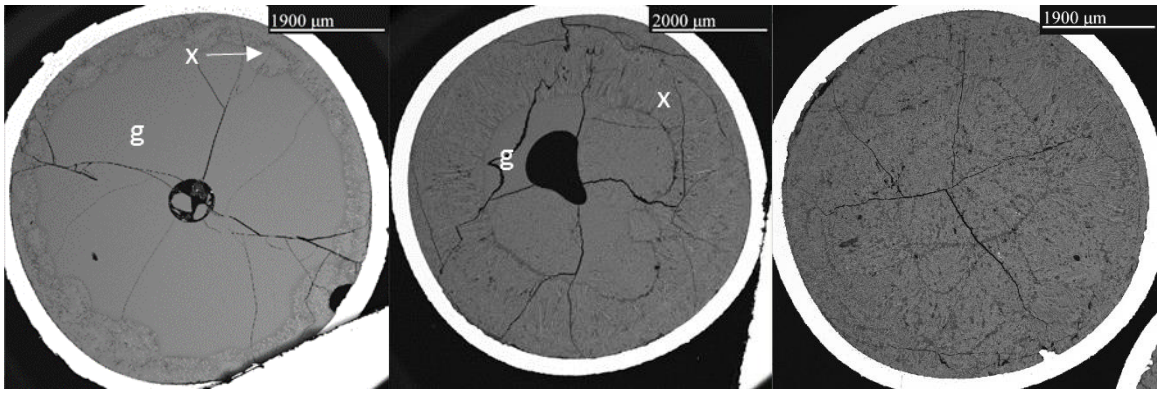

(a) (b) (c)

Figure 3.1: SEM cross sections of aged samples at (a) 4 minutes, (b) 16 minutes, and (c) 1 hour at 700°C. "x" and "g" denote the crystallized and glassy regions respectively.

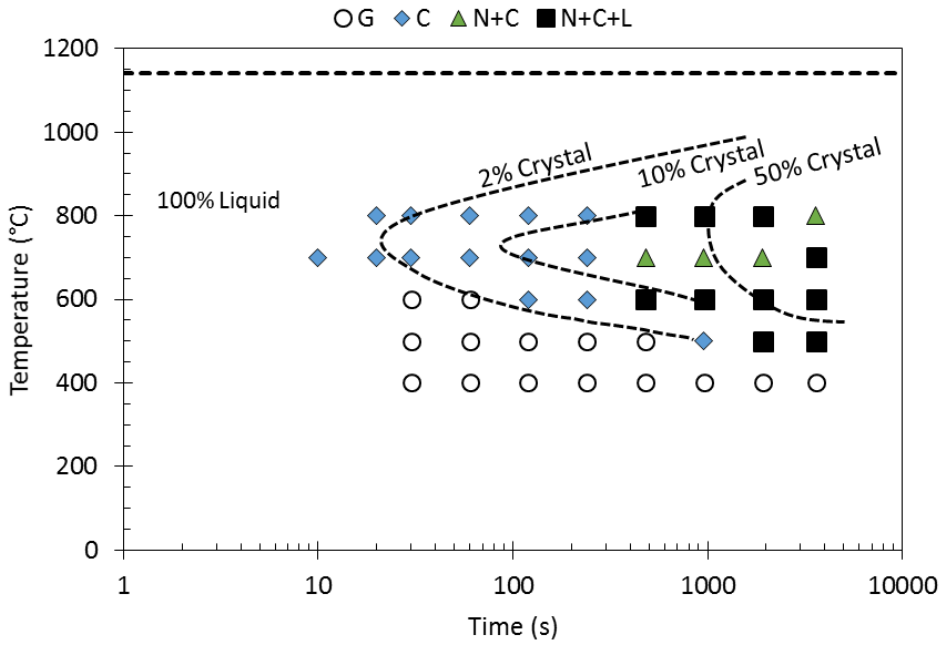

Figure 3.2: TTT diagram indicating phases that form for distinct times and temperatures. "G" indicates that no crystallization was detected. "C" indicates regions where cuspidine forms. Regions with "N+C" contain both cuspidine and nepheline. Regions where all three phases: nepheline, cuspidine, and lithium silicate form are denoted by "N+C+L."

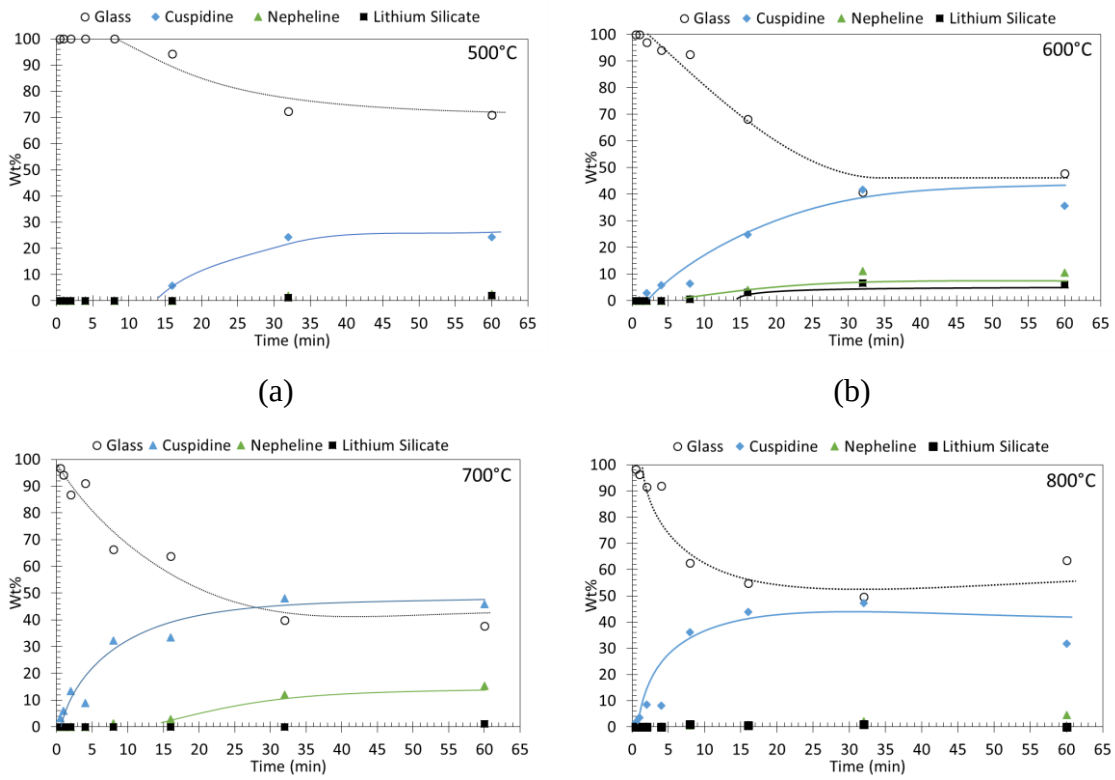

Figure 3.3: Weight percent of each phase plotted against time for (a) 500°C, (b) 600°C, (c) 700°C, and (d) 800°C.

For aging times of less than 1 hour, cuspidine forms at all test temperatures above 400°C. Cuspidine formed after a few seconds at 700°C but required 16 minutes to form at 500°C. After cuspidine nucleation, growth occurred rapidly during the first 15 minutes. Thereafter, the percentage of cuspidine increased more slowly until maximum crystallization was achieved.

In Figure 3.3(b), lithium silicate was indicated to exist based upon XRD results. This phase has not yet been visually identified in SEM specimens. This is likely due to three factors: the low z-value (similar to the base glass), the small (< 5 wt%) percentage that forms, and the fact that lithium is undetectable using standard EDS equipment. Nepheline also forms in relatively small amounts (< 5 wt% at 800°C and 500°C), but at 600°C and 700°C about 10-15 wt% forms. Nepheline is stable over a wider temperature range than lithium silicate and is most favorable to form between 600°C and 700°C.

Nepheline has a similar z-contrast to the bulk glass so high magnification and high contrast are required for identification as shown in Figure 3.4. Nepheline appears to grow between cuspidine crystals, as observed by other investigators [15].

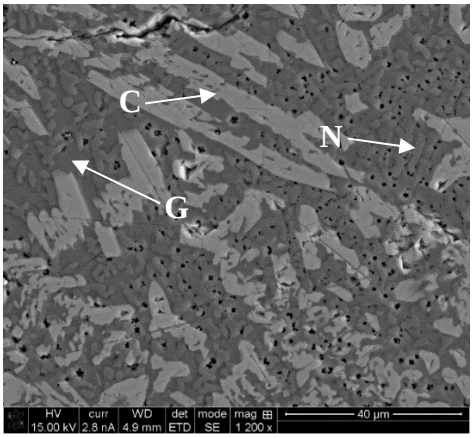

Figure 3.4: High resolution SEM image of sample aged for 32 min at 700°C taken with high contrast. Light phase crystals are cuspidine (C), the dark phase is nepheline (N) and the matrix is glassy (G).

3.2. Industrial Flux Film

A flux film with the chemistry in Table 2.1 was extracted from a funnel mold of a thin slab caster at the end of a heat. Crystallization behavior of the flux film varied with height/position in the mold. XRD results from various regions of the industrial flux film indicate that multiple phases form in the mold gap. The predominant crystalline phases, cuspidine and nepheline, form adjacent to the mold wall as indicated in Figure 3.5. Additionally most samples display a strong amorphous hump in XRD spectra indicating glass formation. Both CL and SEM-EDS corroborate these observations (Figure 3.5). Cathodoluminescence (CL) is a geological technique that is commonly used to analyze rock minerology. It has been applied to analyzing conventional flux films by Paransky et al. [22] and advanced high strength steel (AHSS) flux films by Blazek et al. [23]. The authors employed CL to analyze a flux film with the same chemistry described in Table 2.1, the results are reported in [24].

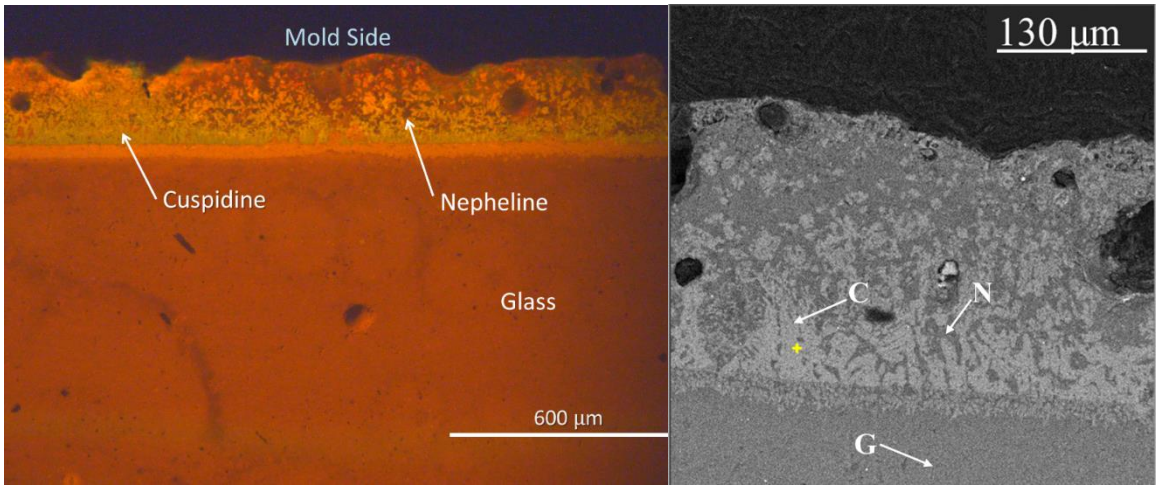

(a) (b)

Figure 3.5: CL image (a) and SEM image (b) of the crystal growth along the mold wall. The cuspidine (C), nepheline (N) and glassy (G) phases are labelled in (b). From [24].

Flux films have a complicated crystalline structure, containing a mixture of phases formed by different thermal histories. Along the mold wall, a thin glassy layer that contains some porosity is observed in Figure 3.6(a). Cuspidine is present just behind this layer in the form of small (< 10µm) faceted crystals. As distance from the mold wall increases the size and area fraction of cuspidine increases (Figure 3.6(b)), but structures remain faceted. EDS maps of two separate crystallized regions along the mold wall (Figure 3.7 and Figure 3.8) indicate that the crystal phase fractions change with distance from the mold wall. The sodium-rich nepheline phase is observed between the cuspidine crystals, but in Figure 3.7 the nepheline fraction is much higher than the region shown in Figure 3.8.

Variability in nepheline crystal density suggests that local temperature differences within the film may affect the crystal growth. Large pores present in the flux film shown in Figure 3.7 likely inhibit heat transfer locally and increase the temperature on the steel side of the pore. The increased temperature in this region appears to coincide with enhanced nepheline growth.

Small equiaxed dendritic crystals were observed on the steel shell side of the crystalline layer. These crystals, Figure 3.9, appear to be less than 5µm in diameter and to have grown from isolated nuclei, not as dendritic structures as observed in Figure 3.8.

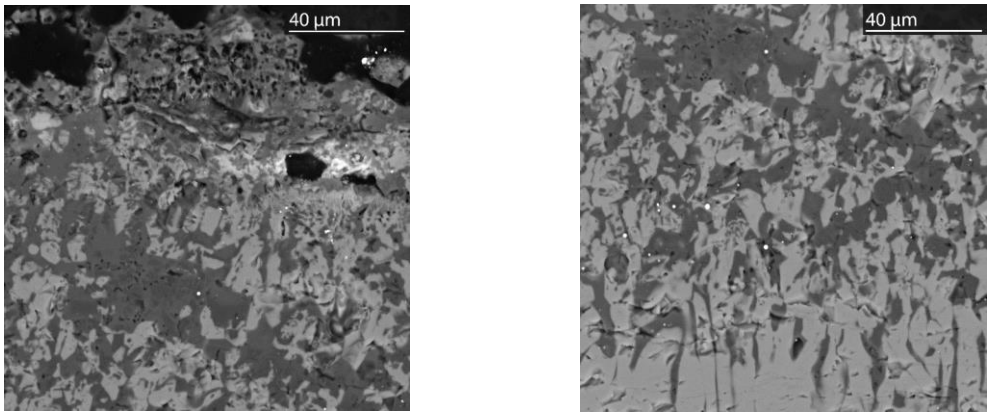

(a) (b)

Figure 3.6: Micrograph of flux film crystalline structure at (a) the mold wall and (b) just above the glass-crystalline region interface.

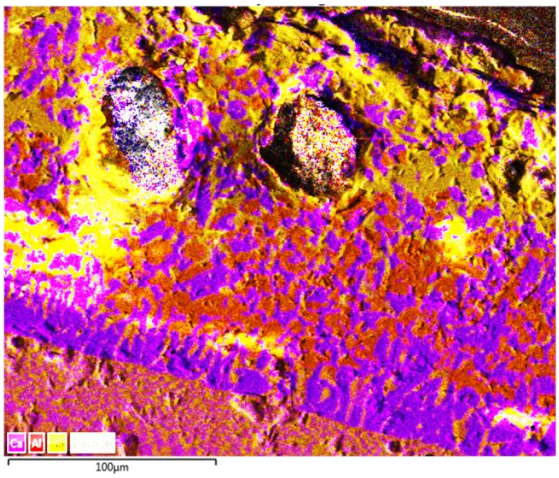

Figure 3.7: Elemental map of flux film against the mold wall superimposed onto the original micrograph. Purple represents Ca-rich cuspidine regions. Yellow indicates Na-rich glassy regions. Orange designates nepheline regions, a mixture of Na and Al.

3.3. Microstructural Comparison

Most of the flux film morphological features appear to be faceted and non-dendritic, with the exception of the dendritic structures observed on the shell side of the crystalline layer. In laboratory continuous cooling tests, the method described in [25] was performed with the same flux chemistry. All crystals formed by continuous cooling had a dendritic

structure (Figure 3.10) and only cuspidine was observed. Since much of the industrial flux film structure is not dendritic and contains nepheline, the observed structures could not have formed by continuous cooling. Thus, the crystal structures observed in the industrial flux film must have formed through devitrification. Laboratory aged samples display morphologies and phase assemblages comparable to those observed in the industrial flux

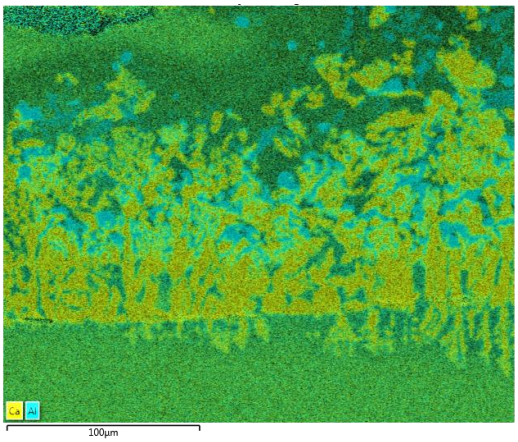

Figure 3.8: Elemental maps of Ca (yellow) and Al (blue) indicating cuspidine and aluminum regions of the flux film respectively. Figure is oriented such that the mold wall is at the top.

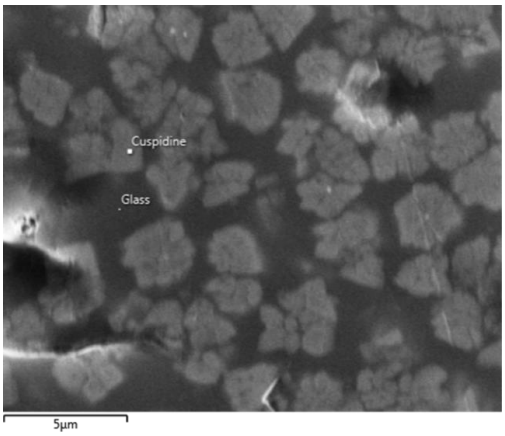

Figure 3.9: SEM micrograph of region below dense cuspidine layer on the steel side.

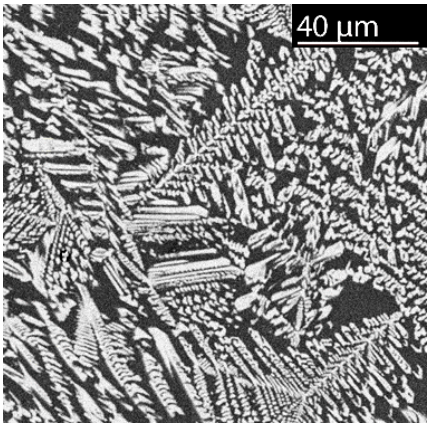

Figure 3.10: Primary dendritic growth from continuous cooling experiment.

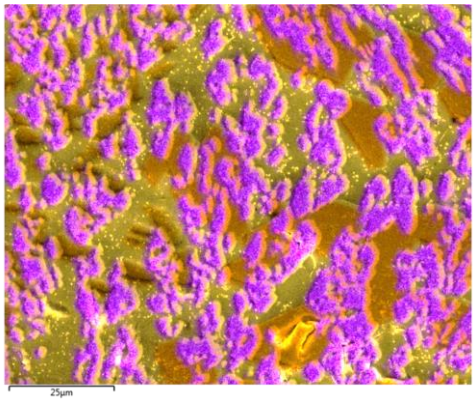

Figure 3.11: EDS map superimposed on an electron micrograph of a tin bath quench sample aged at 700°C for 32 minutes. Purple indicates Ca-rich cuspidine regions. Yellow represents Na-rich glassy regions. Orange denotes nepheline, a mixture of red Al-rich and yellow Na-rich regions.

film (Figure 3.11). Nepheline is observed between cuspidine crystals in both the tin bath quenched samples and the flux film sample, further supporting devitrification as the crystal forming mechanism. The TTT-diagram generated from the tin bath quench experiments indicates that cuspidine is the first phase to form at all temperatures, and that the secondary phases only form after initial cuspidine growth. Nepheline and cuspidine do not appear to co-crystallize. Rather these studies suggest that nepheline nucleation and growth only occurs after cuspidine forms.

4. CONCLUSIONS

The crystallization of a commercial, non-transparent mold flux containing transition metal oxide was measured using a new experimental technique. Quantitative XRD analysis combined with isothermal quenching and aging of flux samples in a molten tin quench bath was used to generate a quantitative TTT diagram for crystallization of the flux. A commercial mold flux film was also examined, and the crystalline phases and structures were compared to laboratory observations. The following conclusions were drawn from the experiments for the flux composition analyzed:

1. In tin bath quench and aged experiments, crystal growth appears to plateau after approximately 30-45 minutes at test temperatures above 400°C. At 400°C, no crystallization was observed for this flux at times of less than 60 minutes. Details of the specific crystalline phases encountered follow.
    a. Cuspidine was the first crystal to form. At the lower test temperatures (400-600°C), several minutes were required before crystallization was observed. At higher temperatures (700-800°C), crystallization occurred within seconds.
    b. Nepheline formed after cuspidine, but only after a minimum of 10 wt % cuspidine was present. In addition, nepheline was observed to form between cuspidine crystals. Nepheline crystallizes most rapidly between 600°C and 700°C. Temperatures above and below this range tend to crystallize with less than 1 wt% nepheline.
    c. XRD results suggests that crystalline lithium silicate may also be present in samples at 600°C, however it was difficult to verify using standard microscopic techniques.
2. In the industrial flux films, faceted cuspidine was observed through most of the crystalline layer, while dendritic (columnar and equiaxed) cuspidine was observed on the steel shell side of the crystalline layer.
3. Comparable crystal morphologies were observed in flux film samples and tin bath quench and age experiments, suggesting that the structures observed in this flux film form by devitrification.

5. ADDENDUM

Synthesis of cuspidine allowed for the verification of the quantitative XRD method outlined in this paper. Cuspidine was synthesized in two steps. First, rankinite was manufactured by mixing 99+% pure $CaCO_3$ and SiO_2 in a 3:2 molar ratio. Powders were thoroughly mixed and pressed into pellets. Pellets were fired in a Pt crucible at 1300°C + 75°C for 10 hours. Samples were immediately removed from the crucible and cooled to room temperature, then Rankinite was confirmed via XRD.

Rankinite pellets were ground and equimolar amounts of rankinite and CaF_2 were mixed together. Pellets were pressed and stacked in a larger Pt crucible for firing. A smaller Pt crucible was placed upside-down over the top of the pellets to act like a lid. The furnace was preheated to 900° + 75°C and then the pellets were placed in the furnace. After 4 hours of sintering, the pellets were removed and quickly cooled in air. The bottom pellet was discarded and top pellets were characterized to confirm the formation of cuspidine. Excess CaF_2 was also identified. For quantification purposes, a small portion of the cuspidine sample was mixed with 25 wt% NIST Alumina standard and analyzed via XRD. The pattern was analyzed using the Reitveld program to confirm the percent CaF_2 present in the sample, fixing the alumina content at 25 wt%. Results showed that less than 3 wt% CaF_2 was present in the cuspidine.

Cuspidine deficient glass was batched and melted from reagent grade raw materials. The chemistry of the glass, as reported in Table 5.1, was based on the G2 flux composition when 43% cuspidine is removed. Cuspidine and the glass were mixed in known ratios: 10/90, 22/78, 30/70, and 43/57 respectively by weight percent, adding 10 wt% alumina standard to each mixture for quantification purposes. Results determined experimentally by Reitveld analysis were compared against the known ratios of the mixtures in Figure 5.1.

Table 5.1: Synthetic glass composition (wt%) based on G2 flux when 43 wt% cuspidine is removed.

CaO	SiO_2	MgO	Al_2O_3	Na_2O	CaF_2	Li_2O
0	45	5	13	25	2	10

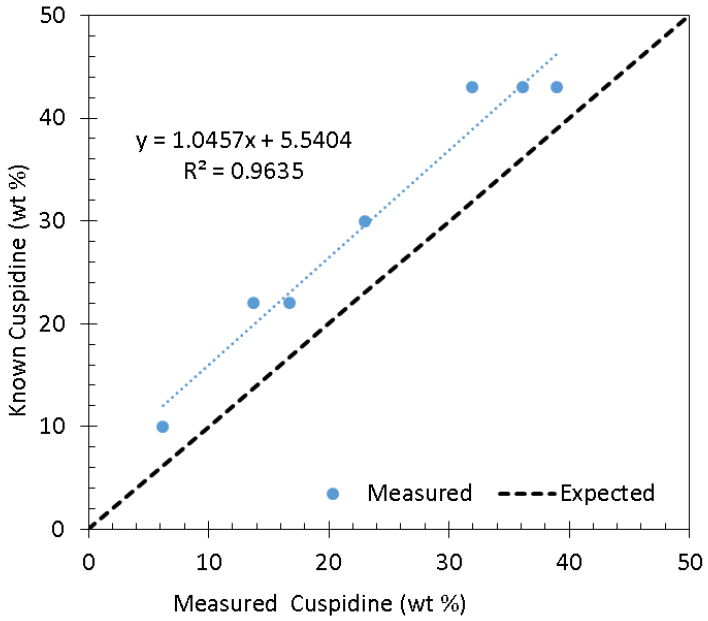

Figure 5.1: Known quantity of cuspidine in each sample plotted against the cuspidine content measured by Reitveld analysis. Same as Figure 2.3 in Methodology section.

Cuspidine batched in the 43/57 cuspidine to glass ratio was re-mixed and analyzed three times on the X-ray diffractometer to quantify the error associated with instrument measurement and Reitveld analysis. The standard deviation indicates approximately 4 wt% standard deviation between the measurements. In addition, the experimental trendline is parallel to the theoretical 1:1 line. This suggests that Reitveld predicts the correct trend with increasing cuspidine content, but it underestimates the percent cuspidine present.

Based on the y-intercept of the trendline, it is suggested that 6 wt% is added to all Reitveld estimations of cuspidine content with a known amount of standard present.

Based on the observations above, the G2 1 hour results were re-quantified by adding 6 wt% to the cuspidine percentage. Phase percentages at shorter times were recalculated based on the area under the (221) cuspidine peak and the corrected 1 hour percentages. Smaller values near the onset of crystallization did not change very much as they were already a small portion of the total crystallization, whereas longer times with larger fractions of crystal changed more significantly. The re-quantified TTT diagram is Figure 5.3, indicating also a 60% iso-crystallization line.

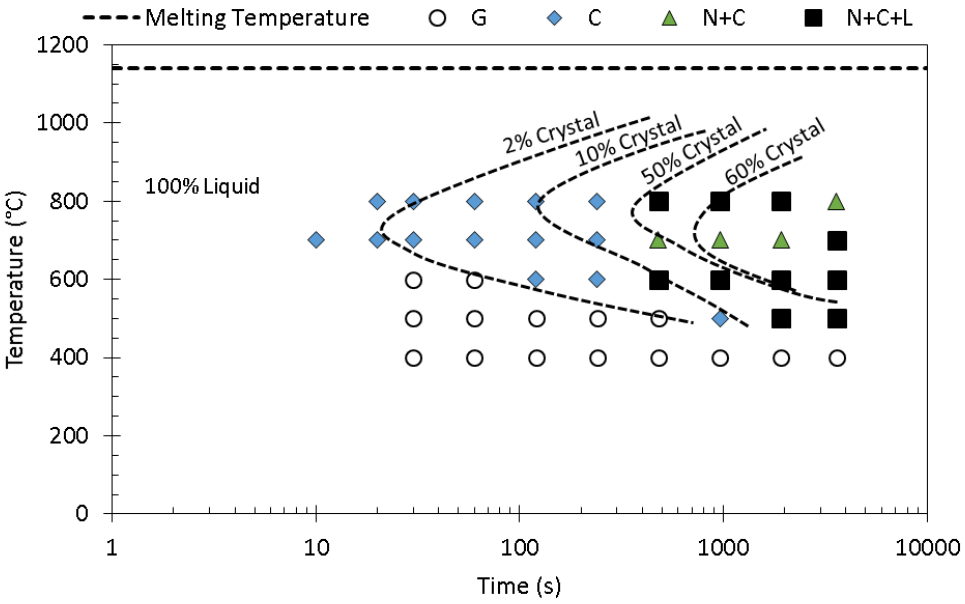

Figure 5.2: Corrected TTT diagram indicating phases that form at distinct times and temperatures. “G” specifies that no crystallization was detected. “C” indicates regions where cuspidine forms. Regions with “N+C” contain both cuspidine and nepheline. Regions where all three phases: nepheline, cuspidine, and lithium silicate form are denoted by “N+C+L.”

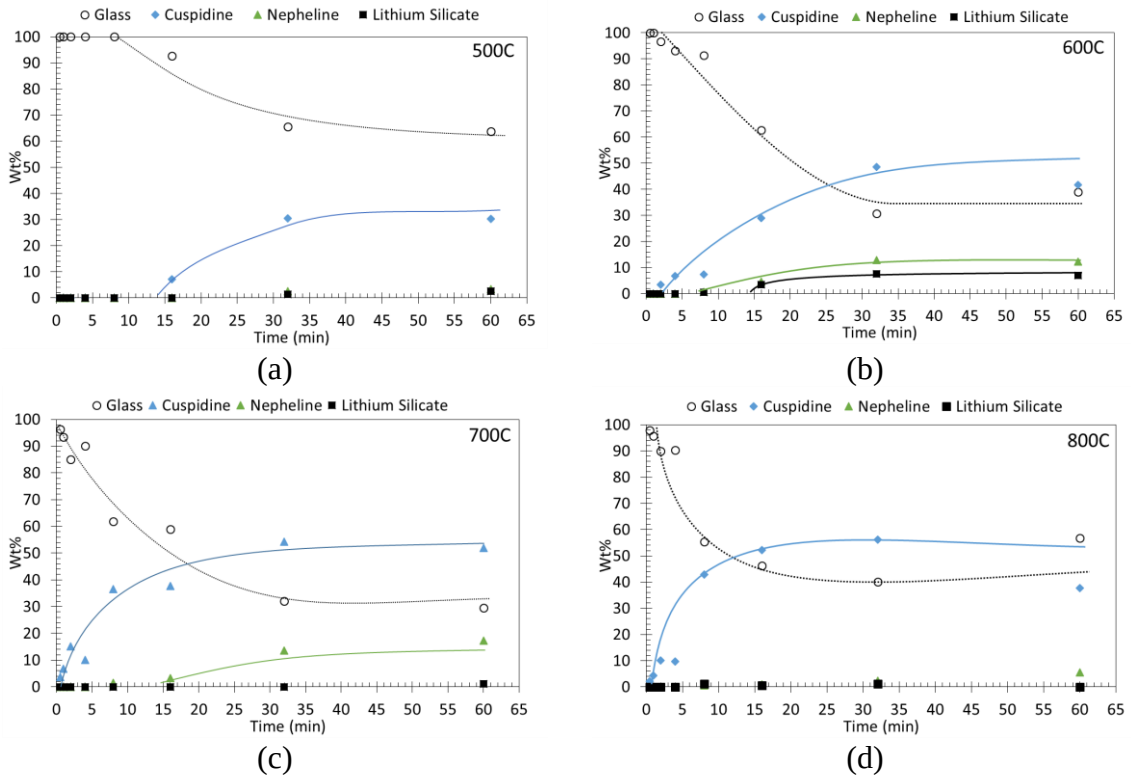

Figure 5.3: Corrected plots of the weight percent of each phase plotted against time for (a) 500°C, (b) 600°C, (c) 700°C, and (d) 800°C.

The graphs of phase growth over time at each temperatures were also corrected and are below as Figure 5.3. Trends in the corrected plots still indicate complete transformation at about 32 minutes. However the percent crystal achieved is at or above 50% for temperatures above 600°C. At 500°C only about 40% crystal is achieved. Other trends corresponding to time of transformation appear constant, although the phase percentages are varied.

6. ACKNOWLEDGEMENTS

We would like to thank the member companies of the Peaslee Steel Manufacturing Research Center (PSMRC) for financial and technical support of this project. We also extend our gratitude to the undergraduate students involved with this project.

REFERENCES

1. K.C. Mills, A.B. Fox, Z. Li, and R.P. Thackray, "The performance and properties of mould fluxes," *Ironmak. Steelmak.*, **32** [1] 26–34 (2005).
2. K.C. Mills, L. Courtney, A.B. Fox, B. Harris, Z. Idoyaga, and M.J. Richardson, "The use of thermal analysis in the determination of the crystalline fraction of slag films," *Thermochim. Acta*, **391** [1–2] 175–184 (2002).
3. K.C. Mills, "Physical Properties of Casting Powders Part 2 Mineralogical constitution of slags formed by powders," *Ironmak. Steelmak.*, **15** [4] 181–186 (1988).
4. K.C. Mills, "Structure and Properties of Slags Used in the Continuous Casting of Steel : Part 1 Conventional Mould Powders," *ISIJ Int.*, **56** [1] 1–13 (2016).
5. Y. G. Maldonado et al., "Estimation of Time-Temperature-Transformation Diagrams of Mold Powder Slags from Thermo-analysis of Non-isothermal Crystallization," *Met. And Mat. Trans. B*, (2014).
6. M.D. Seo, C. Bin Shi, J.W. Cho, and S.H. Kim, "Crystallization Behaviors of CaO-SiO2-Al2O3-Na2O-CaF2-(Li2O-B2O3) Mold Fluxes," *Metall. Mater. Trans. B Process Metall. Mater. Process. Sci.*, **45** [5] 1874–1886 (2014).
7. M.-D. Seo, C.-B. Shi, H. Wang, J.-W. Cho, and S.-H. Kim, "Non-isothermal melt crystallization of cuspidine in CaO–SiO 2 –CaF 2 based glasses," *J. Non. Cryst. Solids*, **412** 58–65 (2015).
8. Y.G. Maldonado, F.A. Acosta, A.H. Castillejos, and B.G. Thomas, "Kinetic Study of the Devitrification of Mold Powder Slags," *AISTech*, 11 (2012).
9. R. Carli and C. Righi, "Mould flux crystallization : A kinetic study;" pp. 821–826 in *VII Int. Conf. Molten Slags Fluxes Salts*. 2004.
10. Z. Wang et al., "Crystallization Kinetics and Structure of Mold Fluxes with SiO_2 Being Substituted for Casting of Titanium Stabilized Stainless Steel," *Met. And Mat. Trans. B*, **44** 606-612 (2013).
11. J. Li et al., "A Kinetic Study of the Effect of Na_2O on the Crystallization Behavior of Mold Fluxes for Casting Medium Carbon Steel," *ISIJ Int.*, **52** [12] 2220-2225 (2012).
12. B. Jiang et al., "A Kinetic Study of the Effect of ZrO_2 and CaO/Al_2O_3 Ratios on the Crystallization Behavior of a CaO- Al_2O_3-Based Slag System," *Met. And Mat. Trans. B*, **45** 1057-1067 (2014).
13. Y. Kashiwaya, C.E. Cicutti, A.W. Cramb, and K. Ishii, "Development of Double and Single Hot Thermocouple Technique for in Situ Observation and Measurement of Mold Slag Crystallization," *ISIJ Int.*, **38** [4] 348–356 (1998).
14. A.W. Cramb, "The Solidification Behavior of Slags: Phenomena Related to Mold Slags," *ISIJ Int.*, **54** [12] 2665–2671 (2014).
15. J.W. Cho and H. Shibata, "Effect of solidification of mold fluxes on the heat transfer in casting mold," *J. Non. Cryst. Solids*, **282** [1] 110–117 (2001).

16. H.G. Ryu, Z.T. Zhang, J.W. Cho, G.H. Wen, and S. Sridhar, “Crystallization Behaviors of Slags through a Heat Flux Simulator,” *ISIJ Int.*, **50** [8] 1142–1150 (2010).

17. M. Hanao, “Influence of Basicity of Mold Flux on its Crystallization Rate,” *ISIJ Int.*, **53** [4] 648–654 (2013).

18. Z. Li, R. Thackray, and K.C. Mills, “A test to determine crystallinity of mould fluxes,” *VII Int. Conf. Molten Slags Fluxes Salts*, 813–820 (2004).

19. R. A. Young. *The Reitveld Method*. International Union of Crystallography, Oxford Union Press, 1995.

20. B. D. Cullity. *Elements of X-ray Diffraction Second Edition*. Addison-Wesley Publishing Company, Inc. 1978.

21. A. Cruz, F. Chávez, A. Romero, E. Palacios, and V. Arredondo, “Mineralogical phases formed by flux glasses in continuous casting mould,” *J. Mater. Process. Technol.*, **182** [1–3] 358–362 (2007).

22. E. Paransky, E. Divry, and M. Rigaud, “Application of Cathodoluminescence Technique in Light Microscopy to Crystallisation Study of Mold Fluxes,” *Micros. Miroanal.*, [Suppl. 2] (2002).

23. K. Blazek, H. Yin, G. Skoczylas, M. McClymonds, and M. Frazee, “Evaluation of Lime-Silica and Lime-Alumina Mold Powders Developed for Casting High Aluminum TRIP Steel Grades;” pp. 1–10 in *Metec Insteel Con*. 2011.

24. E. I. Nolte, J. D. Smith, M. Frazee, N. Sutcliffe, R. J. O'Malley, "Application of Cathodoluminescence in Analyzing Mold Flux Films." 10th International Conference on Molten Slags, Fluxes, and Salts. Wiley, May 2016, 317-25.

25. A. Prasad and H. Henein, “CCT Diagrams for Mold Flux Crystallization Studies,” *ISSTech 2003 Conf. Proc.*, 257–262 (2003).

SECTION

4. CONCLUSION

The research presented in this thesis focused on understanding the morphologies of industrial flux films and attempting to duplicate the structures in a series of laboratory experiments. Cathodoluminesence (CL) microscopy was applied to flux film analysis, allowing for high resolution, low magnification investigation of the mold gap. Using CL, nepheline and cuspidine phases could be distinguished along the mold wall. Additionally fractures were evident in the funnel region of the water-cooled mold. These fractures have been linked to oscillating, "saw-tooth" thermal behavior that occurs only in the funnel region. The high temperature point of the oscillation is correlated to glass infiltration, which increases the heat transfer. As the glass begins to crystallize, the temperature decreases steadily. When crystalline fracture occurs and withdraws, a sudden drop in temperature is experienced, which was correlated to an air gap forming. Thermal data and structural data of the flux film correlated, but structures and phases could not be duplicated by primary cooling.

An isothermal tin bath quench method was developed to increase sample size and avoid chemistry modification relative to other crystallization techniques. Cuspidine was the first phase formed in both continuously cooled and isothermal samples. In isothermal testing, cuspidine was observed to form in several minutes at low temperatures (500-600°C), whereas only a few seconds were required at high temperatures (700-800°C). Nepheline and lithium silicate, two phases not observed in continuously cooled samples, were detected using the isothermal method. Nepheline formed only after cuspidine was in excess of 10 wt% and was most favored between 600 and 700°C. At temperatures outside of this range less than 1 wt% nepheline was observed. Lithium silicate may be present at 600°C, but its existence cannot be proven by standard microscopic techniques. Aged structures were faceted and non-dendritic, which mimic the crystal layer observed along the mold wall. The similarity of aged structures to industrial flux films suggests that the crystalline layer along the mold wall forms by devitrification.

5. FUTURE WORK

5.1. COMPLETION OF PRIMARY TESTING

The step chill testing method works well for easily crystallized fluxes because thermal arrests can be easily identified. On the other hand, glassy fluxes may only crystallize in one cell and have thermal arrests that are difficult to identify. Some glassy fluxes will not crystallize in any of the developed mold configurations. A slower cooling method is necessary for these fluxes. DTA and DSC are slow cool methods, but volatile loss is high for unsealed samples because the heating rate is so slow. A step chill or other slow cool method would be beneficial for identifying a critical cooling rate range for glassy fluxes and identifying behavior for fluxes with long residence times in the mold.

Additional characterization of the primary test thermal data is necessary to understand the effect of composition on the crystallization temperature. Fluxes tested in this thesis were collected from industrial sponsors that produce a variety of steels. Compiling flux chemistry, crystallization temperature, and steel composition data would be useful for mapping out chemistry ranges of fluxes that are compatible with certain steel compositions, and identifying the ideal crystallization behavior for the mold gap. In addition tests would need to be repeated to better quantify the error associated with the crystallization temperature measurement.

5.2. EXPANDING AGED TESTS

Other flux chemistries are already in the process of being testing using the quench and age technique. Completing tests on fluxes with different chemistries would aid in identifying the compositional effects on isothermal crystallization. In addition, the aged crystals could be directly compared to flux films to get an idea of the temperatures experienced along the mold gap. Aged tests may also be repeated numerous times at different aging temperatures to acquire more data points for kinetic analysis of crystallization behavior.

5.2.1 Advanced High Strength Steel Mold Powders. AHSS are of particular interest to the steel industry due to their enhanced mechanical properties. However, the higher alumina content causes significant problems such as changes in heat flux and lubrication during the casting process. Since these steel chemistries are difficult to cast,

they have a higher market value and so their development is of great interest to steel companies. During the casting process, conventional fluxes experience an alumina-silica exchange reaction where the alumina in the steel reduces the silica in the mold powder. Alumina content of the mold powder can increase by 30 weight percent. Since the silica content decreases, the melting temperature of these fluxes increases, changing the properties of the flux during the casting process.

A future experiment has been designed to test AHSS powders at various stages of the alumina-silica exchange reaction, based on dip sample chemistries during the casting of a TRIP steel. Since these powders have elevated alumina contents, a higher temperature furnace is necessary for melting. An induction furnace set up has been completed, as shown in Figure 2.2, to melt these fluxes at temperatures above 1400°C. Extensive TTT-diagram development would aid in understanding the effect of the alumina-silica exchange reaction on the crystal evolution in the mold gap.

5.2.2 Changing Tube Wall Material. Nucleation behavior can change based upon the wetting behavior between the liquid and solid interface. It would be interesting to test graphite, quartz, and copper and compare the nucleation behavior to the steel tubes used in these experiments. Utilizing different materials would help to better understand the effect of the copper mold on the nucleation behavior along the mold wall.

APPENDIX A

INFLUENCE OF MOLD FLUX CRYSTALLITE FILM FRACTURE ON THERMAL FLUCTUATIONS IN A THIN SLAB FUNNEL MOLD

INFLUENCE OF MOLD FLUX CRYSTALLITE FILM FRACTURE ON THERMAL FLUCTUATIONS IN A THIN SLAB FUNNEL MOLD

**Manuscript submitted and accepted for presentation at AISTech 2017.*

R. J. O'Malley[1], E. I. Peterson[1], J. D. Smith[1],
S. Jauch[2], M. McClymonds[2], and N. Sutcliffe[3]

[1]Missouri University of Science and Technology
220 McNutt Hall, 1400 N. Bishop Ave, Rolla, MO 65401
Phone: (573)341-7683
omalleyr@mst.edu

[2]Imerys Steelcasting USA,Inc.
4113 Witmer Road, PO Box 368, Niagara Falls, NY 14302

[3]Nucor Steel Gallatin
4831 US Highway 42 West, Ghent, KY, 41045

Keywords: Mold flux, Mold heat transfer, Crystallization, Thin slab funnel mold, Continuous casting

ABSTRACT

Mold thermal data from two thin slab casters was investigated. Both facilities employ funnel molds that were instrumented with thermocouple arrays that extend into the lower part of the mold. Under specific operating conditions, regular saw-tooth-like temperature fluctuations were observed in the lower part of the funnel area at both facilities. Flux film sampling and analysis of the mold temperature data suggest that the fluctuations are caused by the fracture, removal and regrowth of the mold flux crystalline layer in the convergent area of the funnel. The effects of the film fracture on the heat flux profile in the mold are examined.

INTRODUCTION

The magnitude, stability and uniformity of heat extraction in the mold of the continuous casting process is influenced markedly by the properties of continuous casting

mold flux and the conditions within the mold gap[1-4]. Large local variations in heat removal in the mold can induce stresses in the solidifying steel shell that can lead to defects such as longitudinal cracks, shell buckling and shell thinning. The crystallization behavior of the mold flux plays an important role in the control of the process by slowing the rate of heat extraction and reducing heat removal variability [5, 6]. It has been shown that the stability of the crystalline layer that resides against the mold within the mold gap has a strong effect on the variability in mold temperature and heat removal during casting[2, 7]. Weak crystallites can fracture easily, leading to large variations in heat transfer with time, while excessively strong crystallite layers can cause a steady drop in heat removal over time[2, 8].

In high-speed thin slab casting, the shear stresses in the mold gap are often higher than the stresses observed in the conventional continuous casting process, in part because higher casting speeds and oscillation frequencies are employed in the process. In thin slab casters that employ funnel mold designs, additional shear stresses can be generated in the lower area of the funnel as the solidifying steel shell is formed in the mold to achieve a rectangular slab shape at mold exit[9, 10]. If the shear stresses in this region of the mold exceeds the shear strength of the crystalline layer in the flux film, the film can fracture locally in the region of high shear stress [11-13]. In this paper, the authors present some examples of localized thermal instabilities that were observed in the mold funnel area on two thin slab casters along with evidence for the source of these instabilities. It should be noted that saw-tooth-like mold temperature fluctuations have been observed in many studies [2, 7, 8, 12]. What is of interest here is the relatively small localized area within which these fluctuations occur, and the difficulty in detecting them without employing enhanced mold instrumentation.

PROCEDURE

Process data was collected during casting from two thin slab casters that employed funnel molds. The molds were both instrumented with thermocouples to examine the mold temperatures over a large area of the mold during casting. At caster G, mold flux films were also extracted at cap-off to examine the structures of the flux films in different areas of the mold funnel. A map of the thermocouple positions on the thin slab mold at company

G is shown in Figure 1 and the thermocouple positions on the thin slab mold at company D is shown in Figure 2.

An example of some additional process data (cast speed, mold broad-face heat removal, etc.) collected from company G is shown in Figure 3 for a typical cast sequence of medium carbon steel. The sequence represents 18 hours of casting time. The corresponding thermocouple traces from each broad-face plate for this cast sequence are shown in Figure 4. At company G, the temperature data was recorded at 3 second intervals

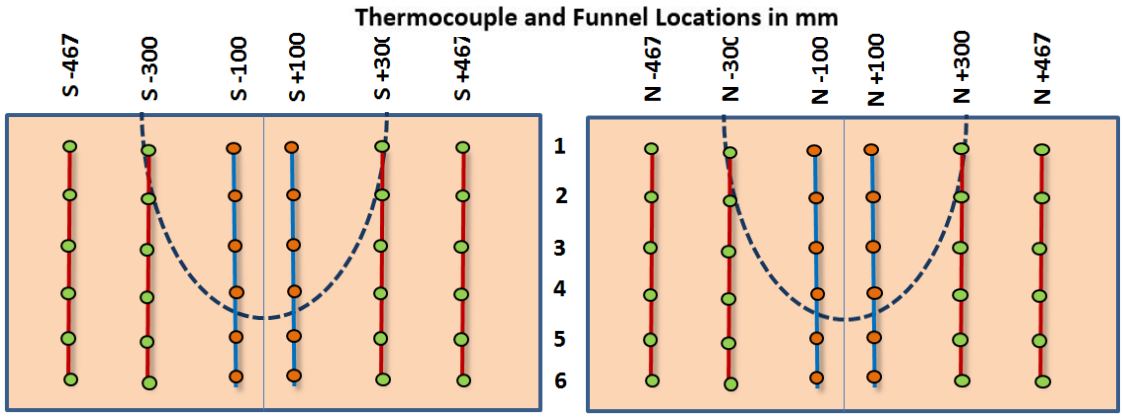

Figure 1: Thermocouple Locations in Funnel Mold at Company G. Vertical distances shown in Figure 4.

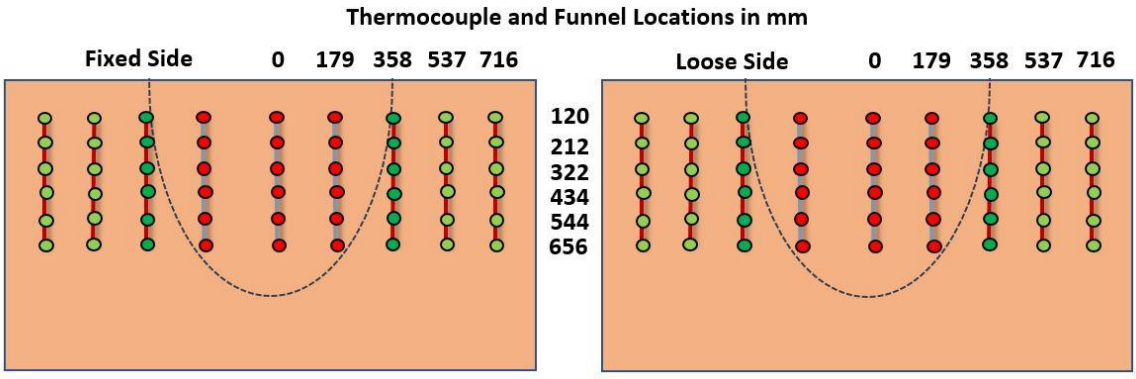

Figure 2: Thermocouple Locations in Funnel Mold at Company D. Distances in mm from center or top of mold.

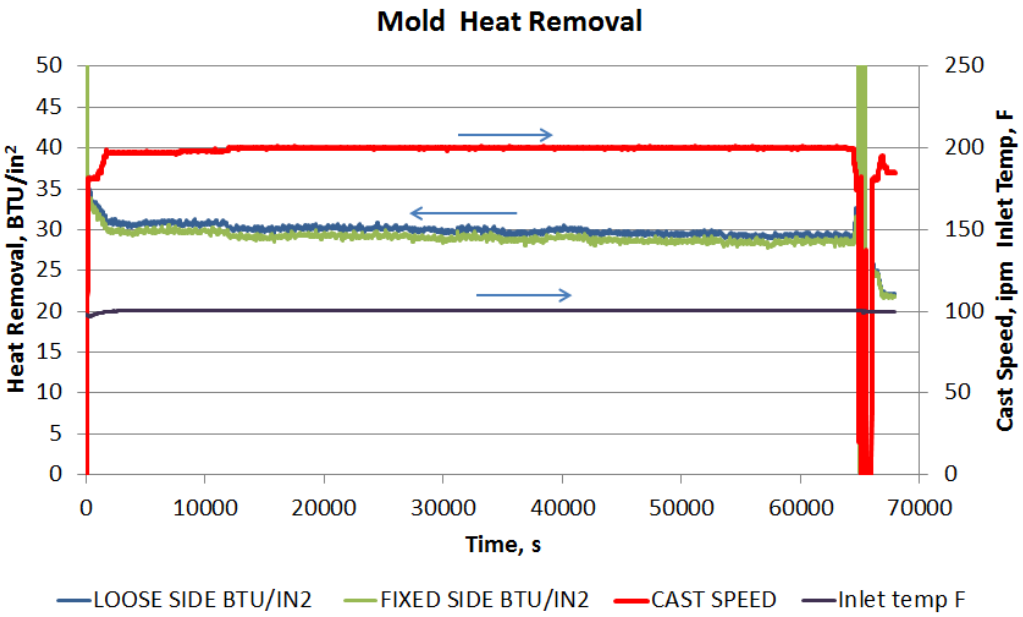

Figure 3: Mold Heat Removal for 1026 steel cast with Flux G2 at Company G. Fixed broad face is south and loose broad face is north.

while company D collected temperature data every 0.5 seconds. Both facilities employed spring loaded type K thermocouples to measure the mold plate temperatures.

The red vertical lines in Figure 4 a and b mark the time at which of the temperature profiles was plotted in Figure 4 c and d. These plots show a snapshot of the temperature profile along the length of the mold for the various thermocouple array positions noted in Figure 1 at the designated time. These profiles were also reviewed as a function of time to observe the dynamic behavior of the mold temperature profiles.

OBSERVATIONS AND DISCUSSION

The sequence presented in Figures 3 and 4 was selected because the caster operated at steady state conditions for a substantial operating period and exhibited relatively stable mold broad face heat removals during the cast. The overall heat flux and mold temperatures look stable at first glance, but they do exhibit some thermal instabilities that were only evident upon reviewing the animated temperature profiles of specific thermocouple arrays and examining the data on an expanded time scale.

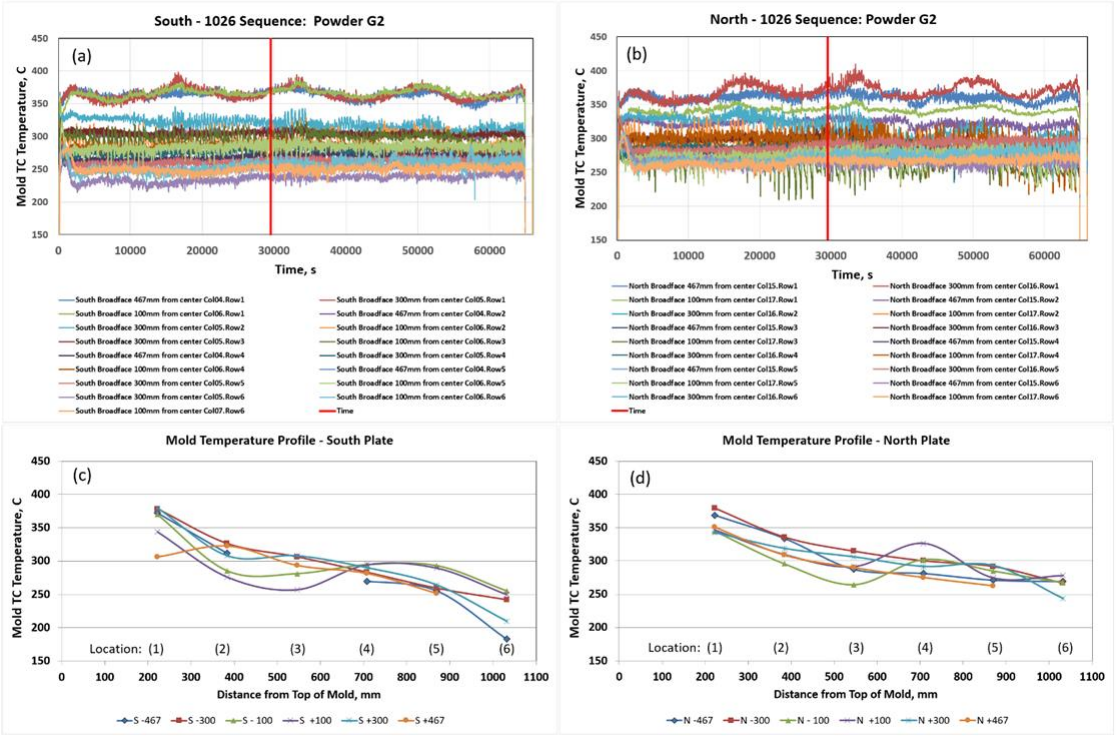

Figure 4: Thermocouple mold broad face temperatures for 1026 with Flux G2 at Company G (a and b) and snapshot of temperature profile on north and south broad face plates at 31000s (c and d) at red vertical line in upper figures.

Figure 5 shows data for two specific thermocouple arrays on the north broad face over a period of 2.7 hours in the middle of the cast sequence. Figure 5a shows the data from a thermocouple array that is within the funnel region of the mold, while Figure 5b shows the data from a thermocouple array that is outside of the funnel region of the mold. It is evident that some specific thermocouple positions within the lower funnel area show strong periodic saw-tooth-like temperature fluctuations, every 600 to 1000 seconds of cast time. It is also interesting to note that while the temperature fluctuations are large (on the order of 50 to 80 C), the observed overall heat removal fluctuations on the broad face plate is barely evident in the heat removal trace in Figure 5. This suggests that the disturbance is localized to the funnel area and not large enough to be detected in the overall broad face heat removal measurements. Outside of the funnel area (Figure 5b), the mold temperatures do not exhibit large fluctuations or saw-tooth-like fluctuations.

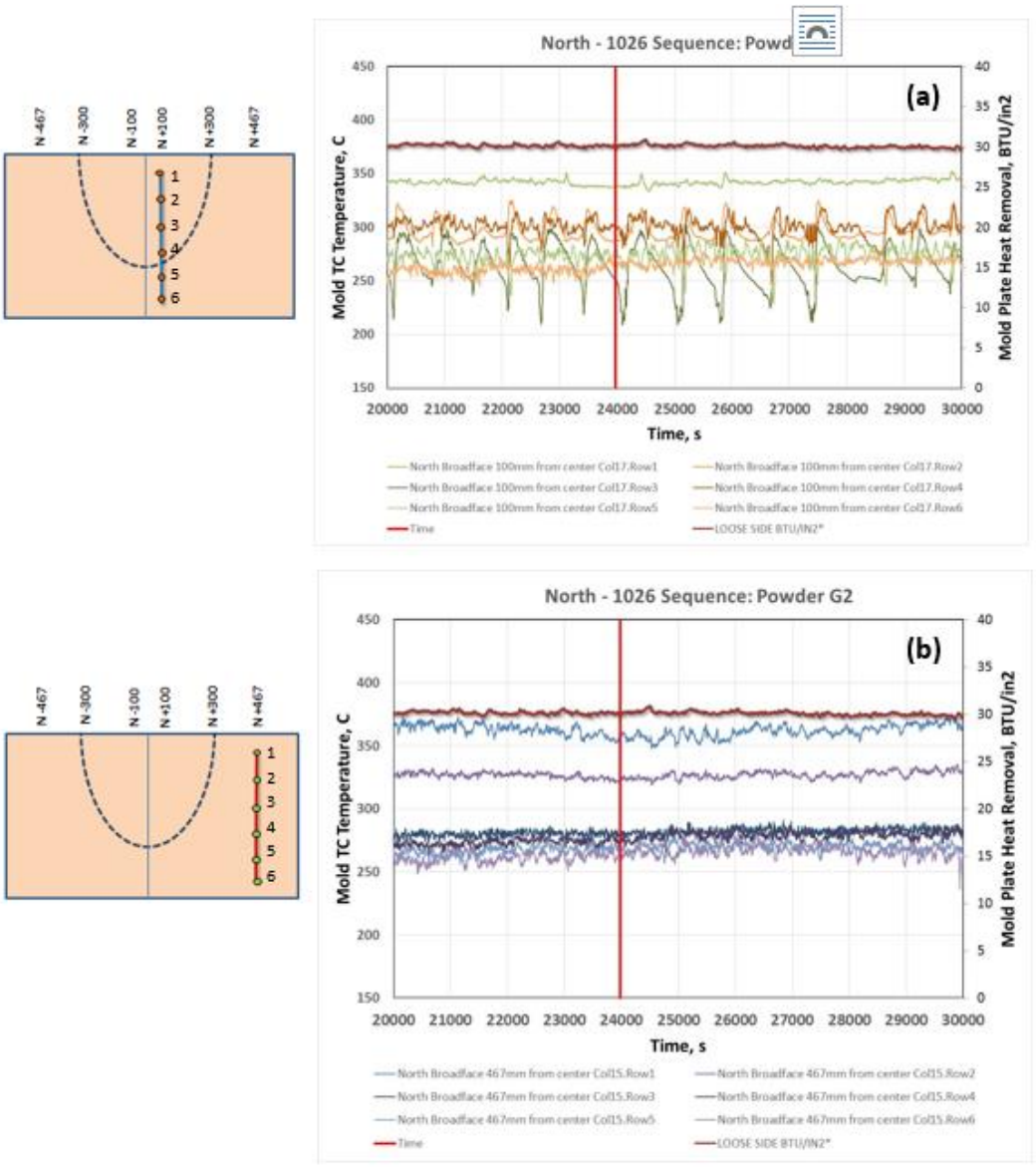

Figure 5: Comparison of isolated thermocouple array temperatures from inside and outside of the funnel area over 2.8 hours of steady state operation.

A snapshot of the temperature profiles for the two thermocouple arrays in Figure 5 at 24,000 seconds (6.7 hours) into the cast sequence is shown in Figure 6. Outside of the funnel area (Figure 6b), the mold temperature decreases uniformly down the length of the mold. However, within the funnel area, the temperature decreases down the length of the funnel area but then increases at the base of the funnel and then decreases again toward the

bottom of the mold. This temperature drop and rebound in the root of the funnel suggests that the solidifying shell is pulling away from the mold and then being compressed as the shell moves through the funnel root area. This behavior is expected because the shell must be formed to accommodate the parallel section at the bottom of the mold.

Similar mold thermal behavior was observed in temperature measurements at Company D. Figure 7 shows the mold temperature trends from thermocouple arrays within (E) and outside (B) of the funnel area during the casting of a 0.25% carbon steel. As observed previously, saw-tooth-like fluctuations are evident in the root area of the funnel and the region outside of the funnel is devoid of the periodic fluctuations.

The saw-tooth thermal behavior is remarkably similar at both mills, despite significant differences in the two thin slab caster designs and the differences in the mold powders employed to produce similar grades of steel. A comparison of the two mold fluxes used in these studies is shown in Table 1. Note that the saw-tooth-like thermal behavior is observed despite the fluxes having very different chemistries and basicity.

An estimate of the rate of propagation of the thermal disturbance was made at Company D by timing a single temperature rise event as it passed successive thermocouples in the funnel area. Data from caster D was used because it had a lower casting speed (2.7 m/min) and a faster (0.5 second) data logging rate. The results, shown in Figure 8, suggest that the thermal disturbance traveled down the mold at about 70% of the casting speed. A similar analysis performed at company G showed a thermal disturbance propagation rate of about 88% of the cast speed at 5 m/min.

The saw-tooth-like temperature fluctuations do appear to be associated with conditions that exist exclusively within the lower funnel area. Figure 9a shows that the timing of the fluctuations is highly correlated within the same funnel but on opposite sides (+100 mm and -100 mm) of the center (0 mm) of the north broad face plate. This suggests that the disturbances within the funnel on an individual mold plate have a common cause. On the other hand, Figure 9b shows that the disturbances within the north face mold plate funnel area and south face mold plate funnel area are out of sync. The thermal disturbances on opposing mold plates were not correlated, despite having very similar average cycle times. This suggests that the disturbances on the loose and fixed side mold plates are not initiated simultaneously by a single event, but instead are initiated within each funnel area

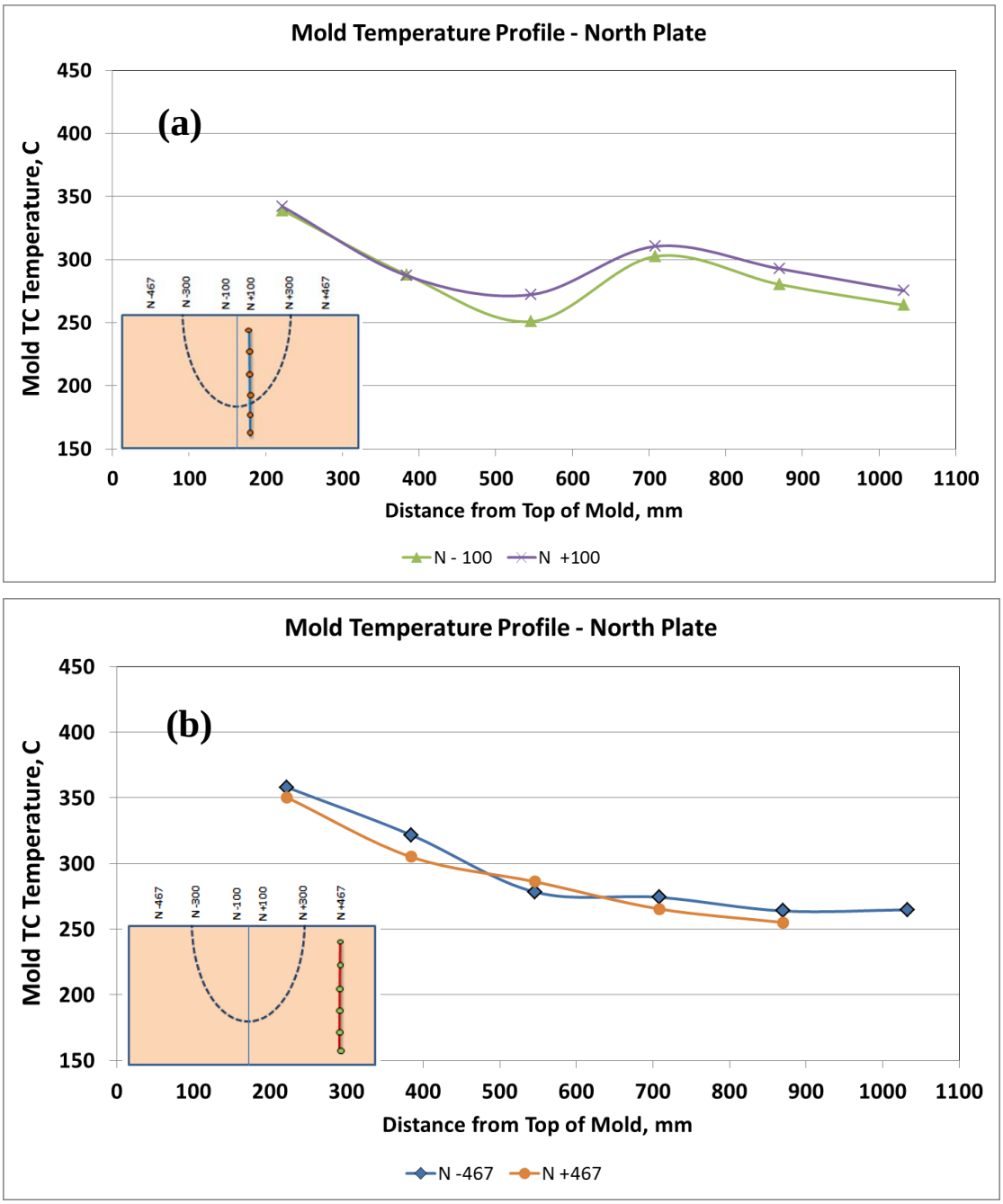

Figure 6: Thermocouple temperature profile snapshot at 24000s (red vertical line in Figure 6) (a) within the mold funnel area and (b) outside the mold funnel area.

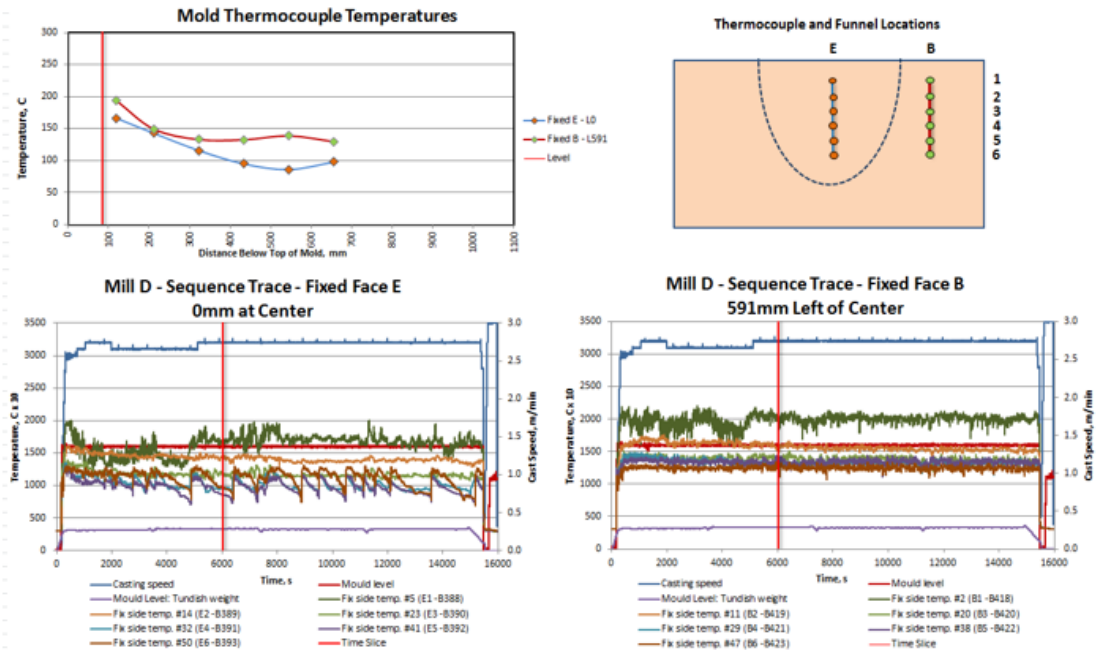

Figure 7: Temperature trends inside and outside of the mold funnel area over 4.5 hours of operation with flux D2 at Company D casting a 0.25 carbon steel.

Table 1: Composition of Mold Fluxes Used – wt.% (R=Na, K, Li)

Flux	Basicity	MgO	Al_2O_3	ΣR_2O	F
G2	0.80	2.6	5.9	16.5	8.6
D2	1.18	1.2	3.5	10.9	8.7

separately, likely due to the local friction conditions on each mold plate. It should also be noted that no catastrophic shell sticking events, severely degraded oscillation marks or other degraded surface conditions on the slab were observed during these sequences at either facility during these tests. This suggests that the disturbance is occurring within the mold gap and not in the solidifying shell.

A G2 mold flux film sample was collected at the end of the cast sequence to investigate the possible cause of these thermal fluctuations in the funnel area. The flux

film was sampled during cap-off at the end of the cast sequence and handled carefully to preserve the approximate position of the flux film within the funnel area. An evaluation of this flux film has been reported on in a previous publication[11]. This work showed that the flux film sample from the upper position in the funnel where the temperature trace was stable shows a continuous, well formed, crystalline layer (Figure 10a). However, the investigation also showed that the flux film sample taken from lower in the funnel area showed evidence of crystalline film fracture and flow lines in the glass that suggest that the observed free floating crystallites originated by fracture and removal from the mold wall (Figure 10b).

The flux film sample, shown in Figure 10b, suggests that fracture and withdrawal of the crystalline film on the mold wall is the primary cause of the observed thermal fluctuations in the root area of the funnel.

The timing of the observed thermal fluctuations in the funnel area is of considerable interest. Even though the solidifying steel shell residence time in the mold is only about 12 seconds on Caster G, we have observed in this investigation that a complete thermal

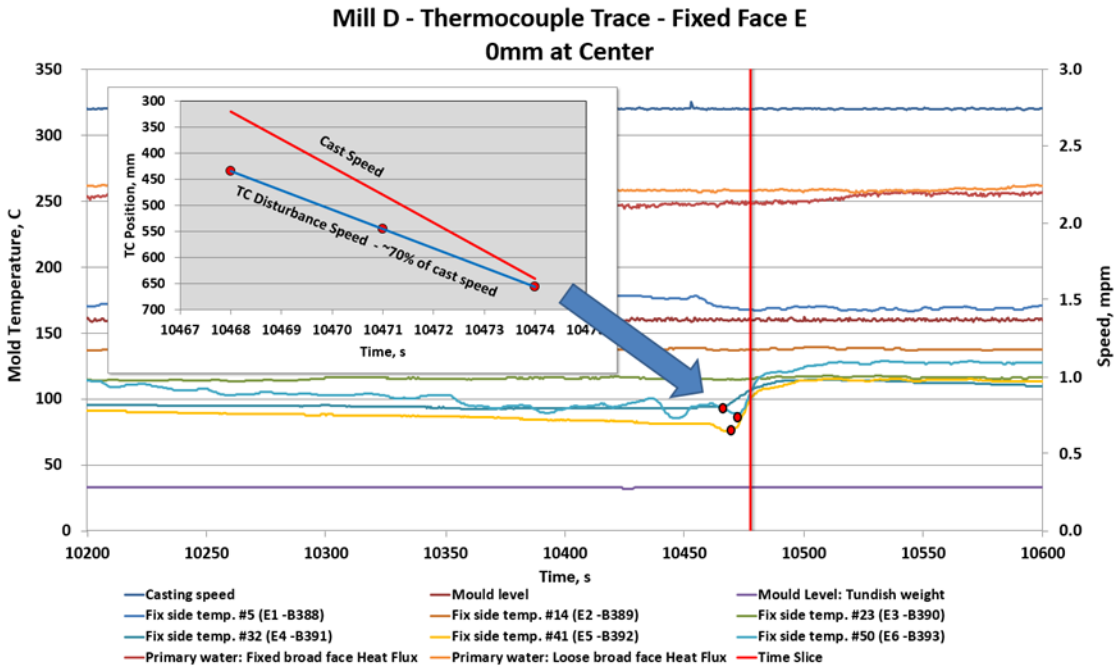

Figure 8: Rate of propagation of thermal disturbance past successive thermocouples in funnel area at Company D compared to casting speed.

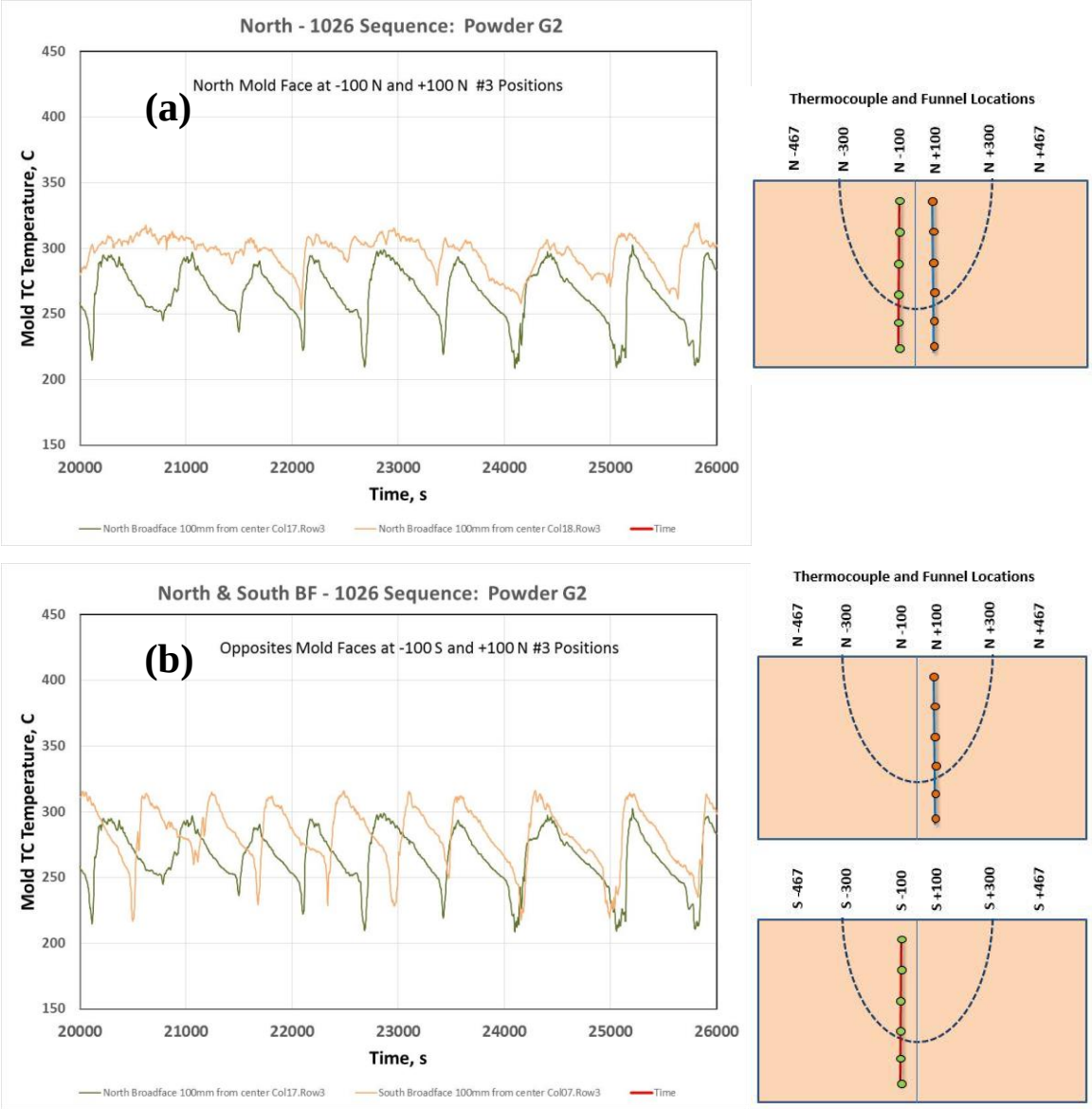

Figure 9: Saw-tooth temperature fluctuations: (a) on north broad face plate at opposite sides of the mold center within the funnel, and (b) on north and south broad face plates within the funnel.

disturbance cycle takes roughly 10 to 20 minutes to complete, with the temperature rise occurring relatively quickly (1-3 minutes) and the temperature decrease occurring very slowly during the remainder of the cycle (7-19 minutes). This slow decrease in temperature is consistent with the time required to form a crystalline layer on the mold wall from a super-cooled glass. Measurements performed by Cramb and others[14-17] have observed comparable crystallization rates when the glass is super-cooled below the nose of the TTT

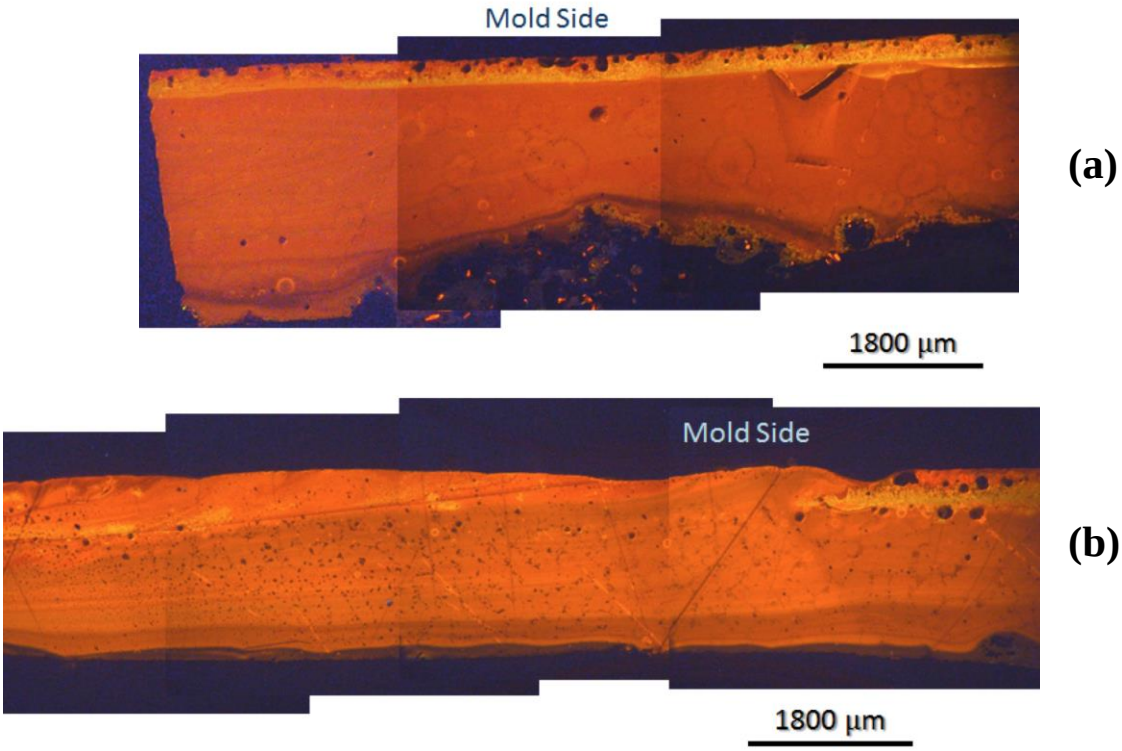

Figure 10: Cathodoluminescence (CL) images of flux film sample G2 taken at cap-off from: (a) stable temperature region (b) region with saw-tooth temperature fluctuations in lower funnel area[11].

curve. Our own laboratory work on flux G2 that has been melted, quenched to 500 C – 800 C and aged shows a similar incubation time for crystal nucleation and growth, as shown in Figure 11[18]. In addition, we have also observed that flux G2 only forms Nepheline crystals when the glass is super-cooled below the nose of the primary Cuspidine crystallization curve and aged, as shown in Figure 12, path 3. The presence of Nepheline in the G2 flux films extracted from the mold at cap-off (Figure 13) supports the claim that the crystallites observed in the mold gap form via devitrification of a super-cooled glass. Based on evidence from the flux film petrography and analysis of the mold thermal data from the two casters investigated, we propose the following mechanism for the occurrence of saw-tooth-like temperature fluctuations in the lower part of a funnel mold: A crystalline film forms by infiltration of molten flux and aging of the glass that resides on the mold wall. As this crystalline layer slowly forms, the rate of heat removal slowly decreases. In regions of higher shear stress local stresses acting on the crystalline film cause it to fracture

and detach from the mold wall. In some cases, the withdrawal of the crystalline layer creates an air gap that causes a sudden additional drop in heat removal. This air gap is rapidly back filled with molten glass, causing the heat removal rate to rise sharply. At this point, the glass begins to age to form a new crystalline layer, repeating the cycle. These

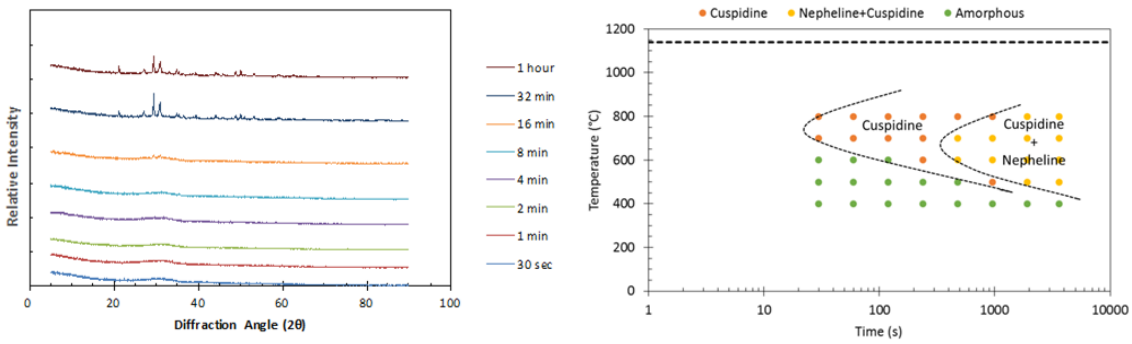

(a) (b)

Figure 11: (a) X-Ray diffraction patterns for G2 flux melted, quenched in molten Sn and aged at 500 C for various times and then water quenched. The appearance of sharp peaks indicates crystallite formation [18]. (b) TTT diagram. Crystal phases consist of Cuspidine and Nepheline.

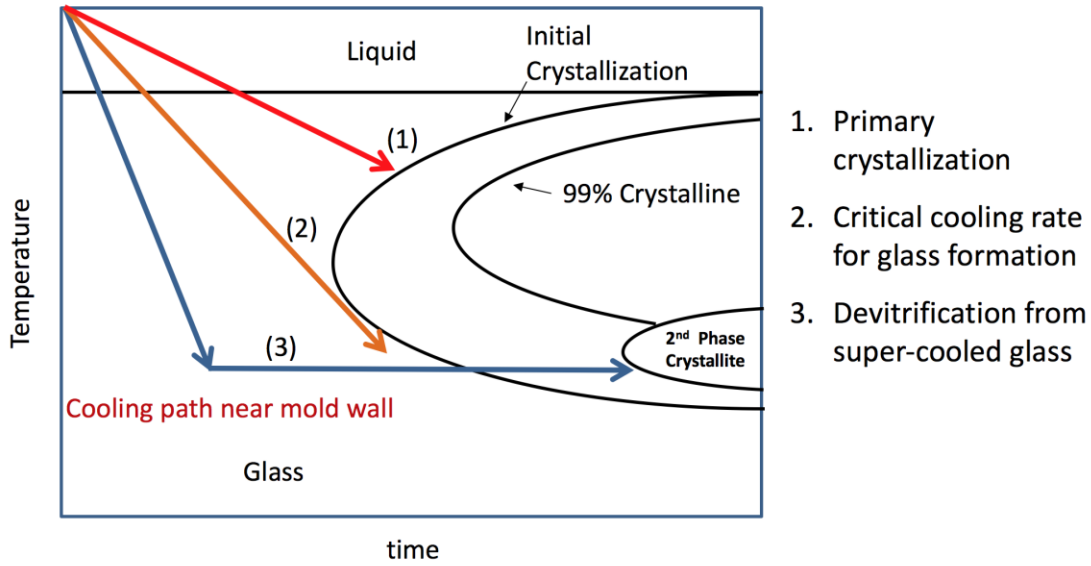

Figure 12: Typical CCT diagram showing alternate paths for crystallization.

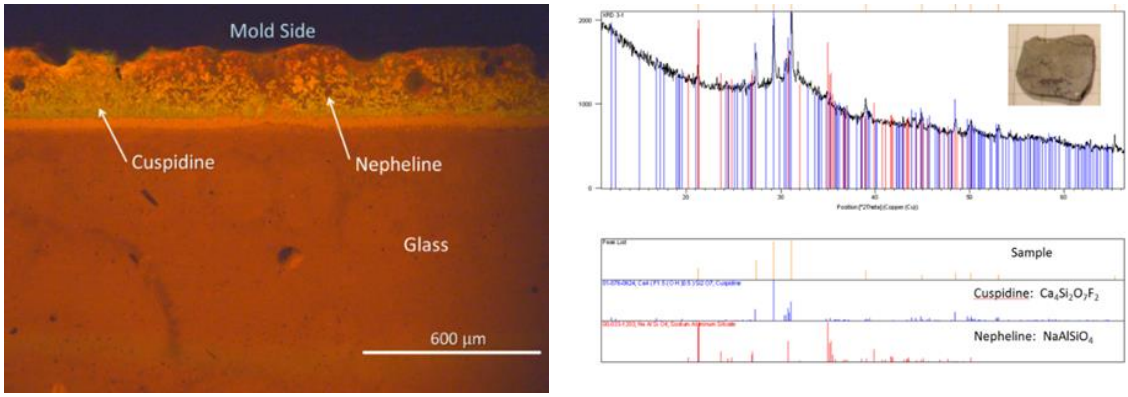

(a) (b)

Figure 13: (a) CL image of crystalline layer in G2 flux film sample showing evidence of Cuspidine and Nepheline phases [11]. (b) Phases confirmed by XRD analysis.

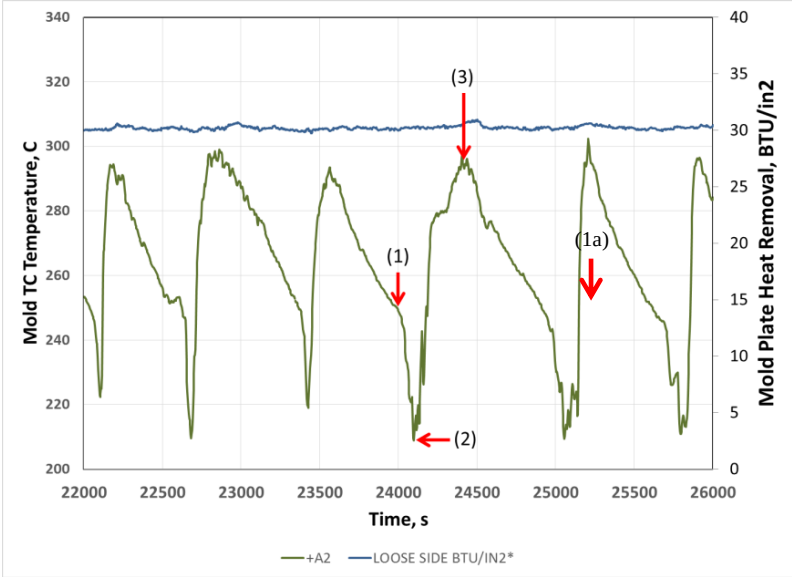

Figure 14: Proposed origin of saw-tooth temperature fluctuations at TC#3 in funnel: (1) fracture of flux crystalline film, (1→2) withdraw of flux crystalline film and air gap formation, (2→3) inflow of glass, (3) complete glass infiltration, (3→1a) aging and crystallization of glass [11].

steps are summarized in Figure 14. Note that not all thermal fluctuations exhibit air gap formation (steps 1-2).

A mold heat flux model was employed to attempt to estimate the magnitude of the local changes in the heat flux profile in the funnel area compared to the body of the mold under the localized crystalline film sheeting conditions. This model was adapted to the operating conditions employed at company G during the time of the casting trial. The details of the model formulation and data fitting procedures are reported elsewhere [7, 19, 20]. In this investigation, the overall heat flux profile was fitted to agree with the thermocouple temperatures measured in the mold plate outside of the funnel and the overall mold plate heat removal. The local heat flux profile for the funnel region was adjusted to force agreement with the local temperatures in the funnel. This approach is justified because the local heat flux changes in the funnel area do not affect the overall mold heat removal of the mold plate significantly, as shown previously in Figure 5.

The temperatures and predicted heat flux profiles at three steps in the thermal cycle of a single saw-tooth-like temperature fluctuation event shown in Figure 14 are summarized in Figures 15 – 17. The predictions suggest that local heat flux varied by approximately 47% locally (1.8 MW/m^2) in the funnel root area when fluctuations were present. Furthermore, the predictions suggest that the local heat flux dropped by about 21% (0.8 MW/m^2) as the infiltrated glass crystallized, with the remaining 26% drop (1.0 MW/m^2) resulting from local flux starvation and air gap formation. The impact of these changes in heat flux on the predicted mold hot face temperature profiles is shown in Figure 18 for the two extreme heat flux conditions presented in Figures 16 and 17. The predictions suggest that the hot face temperatures can fluctuate by more than 160 °C during a flux film shearing event.

It is interesting to note that an animated view of the temperature profiles shown in Figure 15 shows evidence that the thermal disturbance induced by the flux film fracture and withdrawal initiates at or before the TC#2 position (384 mm from the top of the mold), propagates through to the exit of the mold on Caster G and exits at about 88% of the shell withdrawal speed. The largest temperature disturbance is observed at TC#3 (546 mm below the top of the mold). The thermocouples below position #3 show smaller temperature disturbances. The large temperature drop at TC#3 may have several possible

causes. The temperature drop from (1) to (2) appears to be the result of an air gap formed by liquid flux starvation immediately after the withdrawal of the crystalline layer. The sharp drop is not seen at other thermocouple positions, suggesting the intermittent flux starvation is localized to specific regions in the lower funnel area. Another possibility is that at higher positions in the mold, higher temperatures in the mold gap increases the rate of crystal growth from the infiltrating glass, as shown in Figures 11 and 12.

Ultimately, the crystal structures and phases that form in the mold gap define the strength of the film and its ability to resist fracture. The flux crystallite morphology is a strong function of temperature and the cooling path that is experienced by the molten flux. Conditions of high localized stresses found within the funnel area of a thin slab mold can lead to localized flux film fracture where elsewhere in the mold, the flux film had sufficient strength to resist fracture. Currently, we are able to reproduce the phases and structures observed in extracted flux films using commercial mold fluxes in the laboratory[18]. However, we have yet to develop a method for growing crystalline flux films and testing their strength in the lab. More work is still needed to realize the goal of laboratory testing of mold fluxes to confirm how they function in the continuous casting process.

CONCLUSIONS

Localized periodic thermal fluctuations observed in the lower funnel region of the mold on two thin slab casters were investigated using mold thermocouple array data, flux film sampling and laboratory crystallization studies. Analysis of the thermal data and analysis of extracted flux films indicate that the thermal fluctuations are the result of flux film fracture and withdrawal in the funnel area, followed by a brief period of air gap formation at some locations, glass infiltration into the gap and crystallization of the infiltrated glass. The withdrawal rate of the crystalline layer was measured to be between 70% and 88% of the strand withdrawal speed.

The slow drop in heat removal following glass infiltration was found to be consistent with crystallization rates reported in literature and with those measured in the lab for the G2 mold flux. The presence of Nepheline in crystalline phases observed in the extracted flux film was also consistent with a cooling path that produces a supercooled

glass that remains in contact with the mold wall for an extended period of time and slowly ages and devitrifies.

Thermal disturbances appeared to be caused by a single sheeting event within the funnel of an individual broad face plate. The cycle times of the thermal disturbances within the funnel on one mold plate were well correlated. Thermal disturbances in the funnel region on opposing broad face plates were not correlated, but did have similar cycle times. Sheeting events appear to be associated with local conditions on each broad face plate. Conditions of high localized stresses found within the funnel area of a thin slab mold can lead to localized flux film fracture where elsewhere in the mold, the flux film had sufficient strength to resist the fracture of the crystalline layer. Additional work is still needed to characterize the relationship between flux film structures and their resistance to crystalline film fracture.

This investigation also highlights the importance of mold temperature mapping in the development of fluxes for continuous casting. The temperature disturbances observed at both casting operations would likely never have been identified by conventional mold heat removal and breakout detection thermocouple measurements.

ACKNOWLEDGEMENTS

The authors would like to acknowledge the industrial members of the Peaslee Steel Manufacturing Research Center for their support of this project. We would also especially like to thank Mike Frazee, Darrell Sturgill and the laboratory staff at Imerys for their assistance in supply, sampling and analysis of the mold fluxes in this study. Also, special thanks to Todd Sander of Missouri S&T for his assistance in laboratory testing.

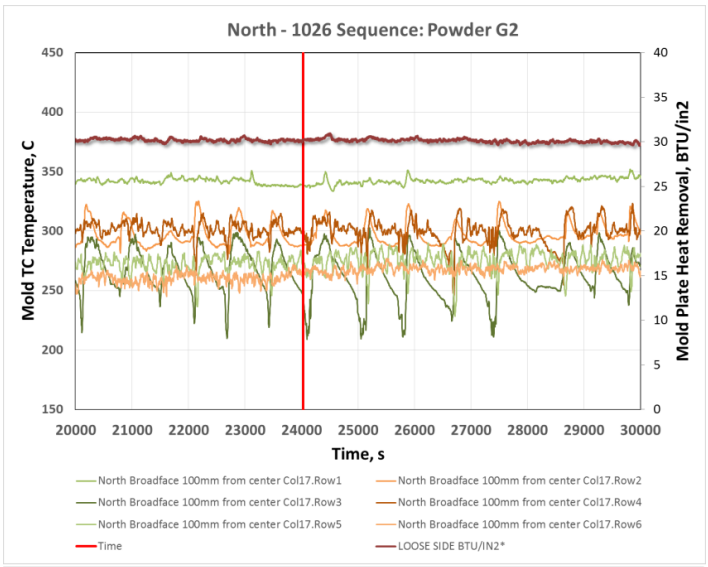

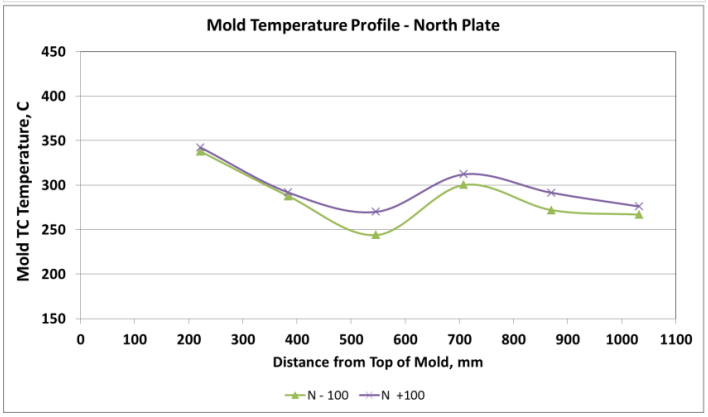

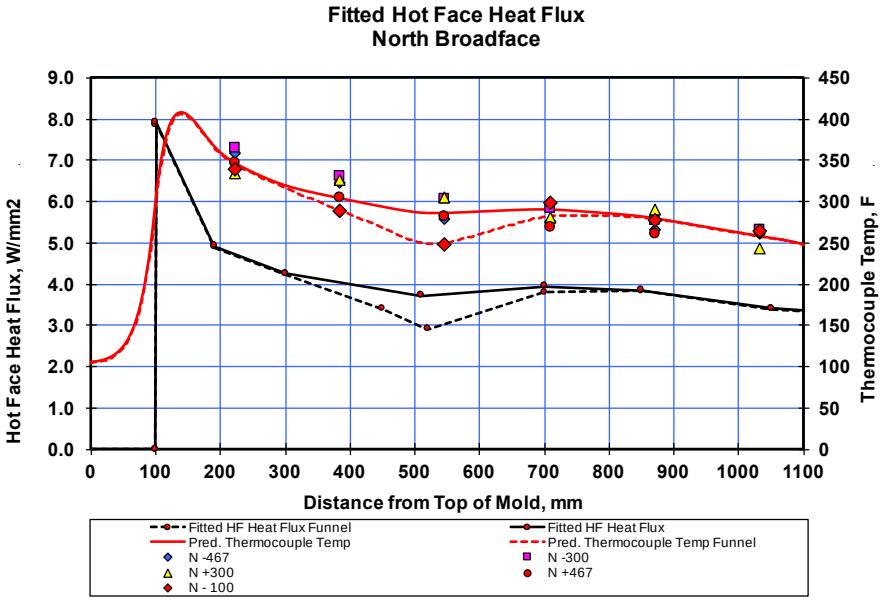

Figure 15: Thermocouple temperature profile snapshot at 24000s and predicted heat flux profile.

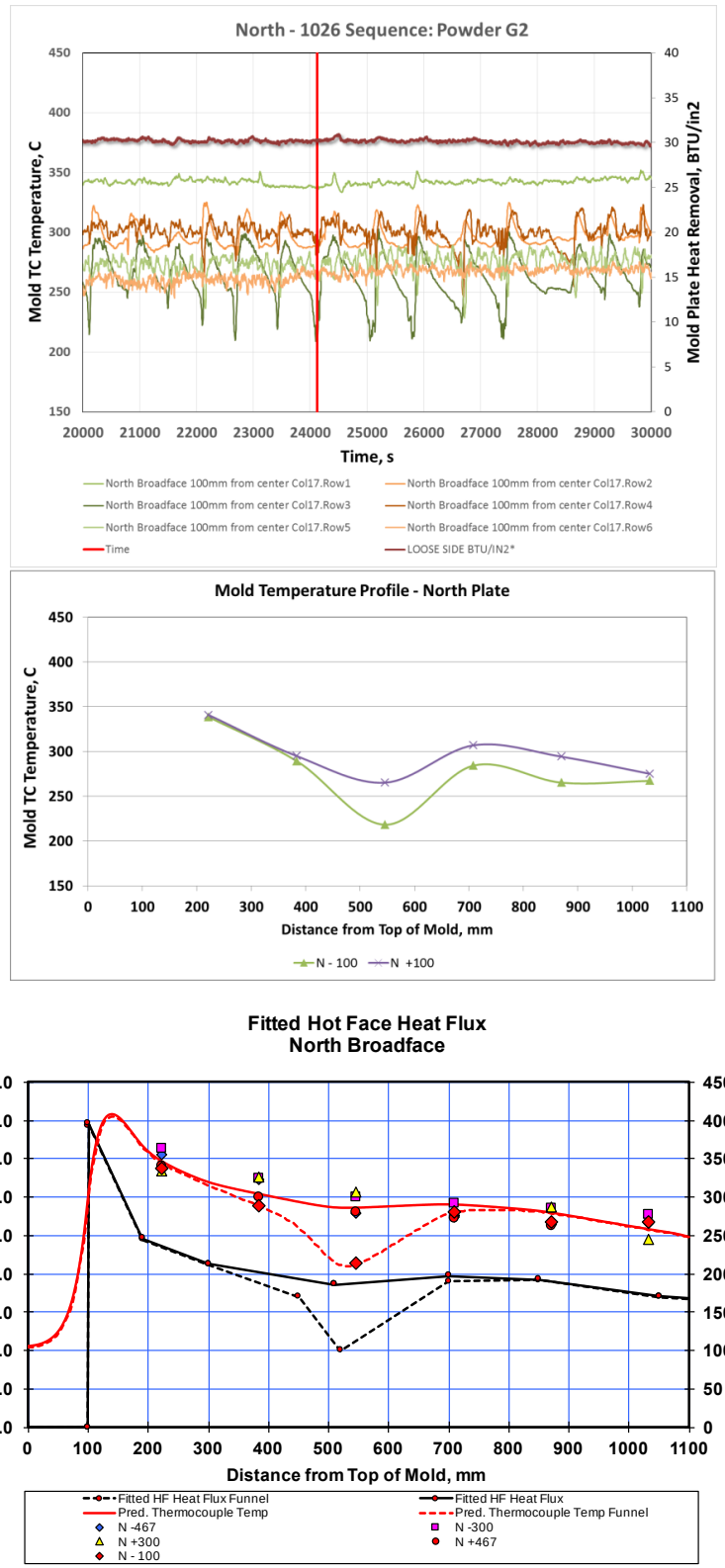

Figure 16: Thermocouple temperature profile snapshot at 24105s (minimum temperature) and predicted heat flux profile.

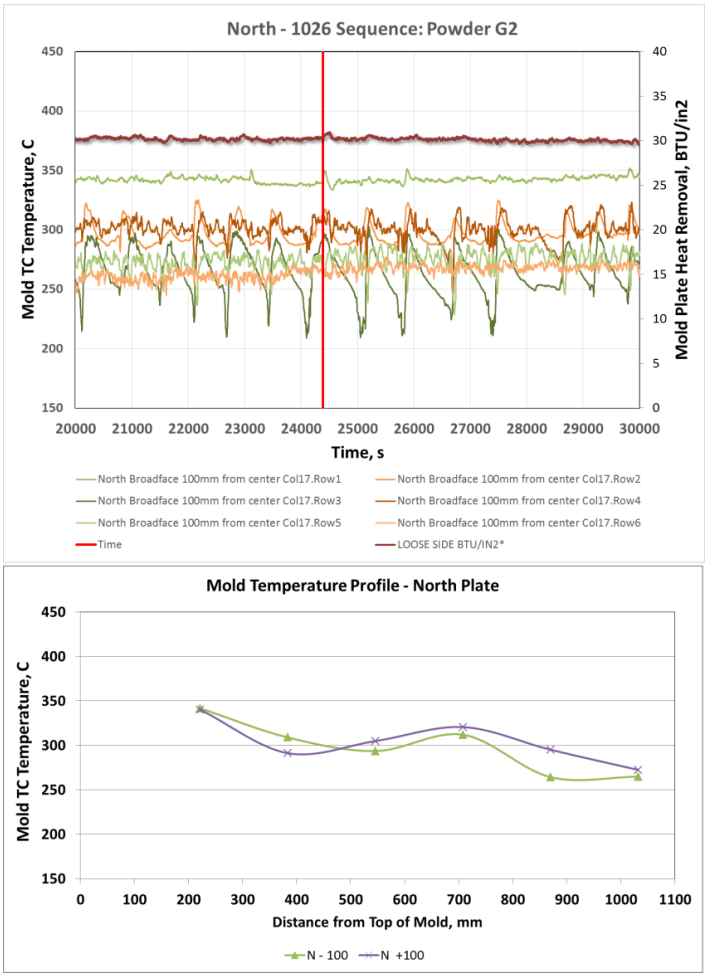

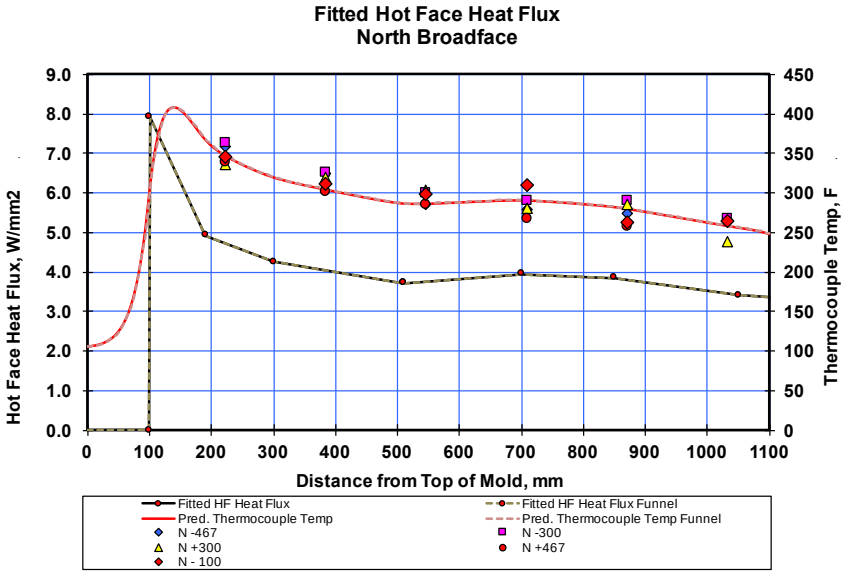

Figure 17: Thermocouple temperature profile snapshot at 24405s (maximum temperature) and predicted heat flux profile.

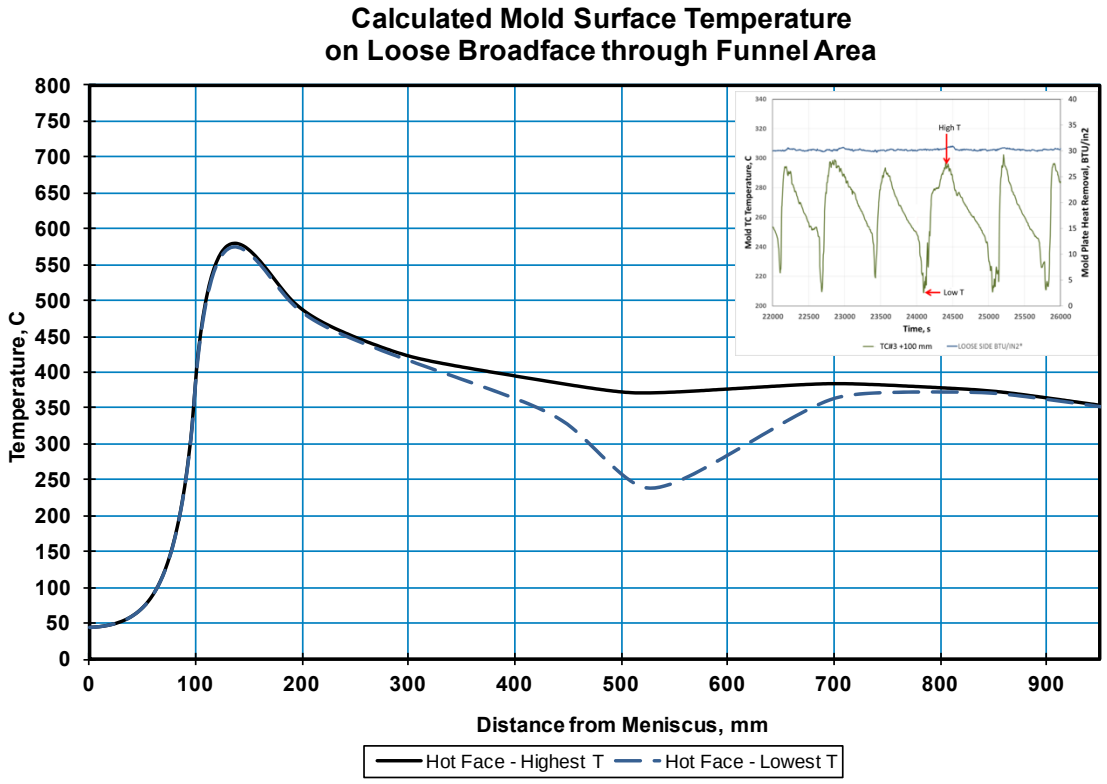

Figure 18: Predicted Mold Plate Surface Temperature Profiles for High and Low Temperature Conditions shown in Figure 14.

REFERENCES

1. Cramb, A.W., *The Making, Shaping and Treating of Steel: Casting Volume*, ed. A.W. Cramb. 2003: AISE Steel Foundation.
2. O'Malley, R. *Observations of various steady state and dynamic thermal behaviors in a continuous casting mold*. in *82nd Steelmaking Conference*. 1999. ISS.
3. Mills, K. *Mould fluxes for continuous casting and their effect on product quality*. in *Alex McLean Symposium: Process Fundamentals, Liquid Metal Processing for Cleanliness, Novel and Conventional Casting, and Novel Process Technologies*. 1998.
4. Mills, K.C. and A.B. Fox, *The role of mould fluxes in continuous casting-so simple yet so complex.* ISIJ international, 2003. **43**(10): p. 1479-1486.
5. H. Yasunaka, H. Matsuda, and K. Matsuo. *Effect of Thermal Properties of Mold Flux on Surface Quality of Continuously Cast Slab*. in *4th International Conference on Molten Slags and Fluxes (Molten Slags & Fluxes '92): 8-11 June, 1992, Sendai International Center, Sendai, Japan : Proceedings*. 1992. Iron and Steel Institute of Japan.

6. Kawamoto, M., et al., *Improvement of the Initial Stage of Solidification by Using Mild Cooling Mold Powder*.* ISIJ international, 1997. **37**(2): p. 134-139.
7. O'Malley, R. and J. Neal. *An Examination of Mold Flux Film Structures and Mold Gap Behavior Using Mold Thermal Monitoring and Petrographic Analysis at Armco's Mansfield Operations*. in *Proc. METEC Congress*. 1999.
8. Hooli, P., *Study on the layers in the film originating from the casting powder between steel shell and mould and associated phenomena in continuous casting of stainless steel*. 2007, Helsinki University of Technology.
9. Hibbeler, L., et al., *Longitudinal face crack prediction with thermo-mechanical models of thin slabs in funnel moulds.* La Metallurgia Italiana, 2009(2).
10. Hibbeler, L.C., *Thermo-mechanical behavior during steel continuous casting in funnel molds*, in *Mechanical Engineering*. 2010, University of Illinois at Urbana-Champaign.
11. Nolte, E., et al. *Application of Cathodoluminescence in Analyzing Mold Flux Films*. in *Advances in Molten Slags, Fluxes, and Salts: Proceedings of the 10th International Conference on Molten Slags, Fluxes and Salts*. Wiley Online Library.
12. Kromhout, J., et al., *Challenge to control mould heat transfer during thin slab casting.* Ironmaking and Steelmaking, 2013. **40**(3): p. 206-215.
13. Meng, Y. and B.G. Thomas, *Modeling transient slag-layer phenomena in the shell/mold gap in continuous casting of steel.* Metallurgical and materials transactions B, 2003. **34**(5): p. 707-725.
14. Cramb, A.W., *The Solidification Behavior of Slags: Phenomena Related to Mold Slags.* ISIJ International, 2014. **54**(12): p. 2665-2671.
15. Orrling, C., S. Sridhar, and A. Cramb, *In situ observations and thermal analysis of crystallization phenomena in mold slags.* High Temperature Materials and Processes, 2001. **20**(3-4): p. 195-200.
16. Kashiwaya, Y., C.E. Cicutti, and A.W. Cramb, *An Investigation of the Crystallization of a Continuous Casting Mold Slag Using the Single Hot Thermocouple Technique.* ISIJ international, 1998. **38**(4): p. 357-365.
17. Petajajarvi, M., et al., *Industrial mould slags for continuous casting of stainless steel–analysis of the crystallisation behaviour using the Single Hot Thermocouple Technique*, in *Ninth International Conference on Molten Slags,Fluxes and Salts (MOLTEN12)*. 2012, The Chinese Society for Metals.
18. Peterson, E., J. Smith, and R. OMalley, *Mold Flux Crystallization*, in *PSMRC Internal Report*. 2016, Missouri University of Science and Technology.
19. Hibbeler, L.C., et al., *Calibration of Thermal Models of Steel Continuous Casting Molds.* AIST Transactions, 2013. **9**(September).
20. Thomas, B.G. and B. Ho, *Spread sheet model of continuous casting.* Journal of engineering for industry, 1996. **118**(1): p. 37-44.

APPENDIX B

UNPUBLISHED WORKS

UNPUBLISHED WORKS

The work contained in this thesis was supported by the Peaslee Steel Manufacturing Research Center (PSMRC). Annual reports and semesterly presentations were given as an update on the project progress and to inform industry members of current results. All of the primary testing as well as some other results are outlined in those PSMRC documents and are listed below:

1. R. O'Malley and E. Nolte, PSMRC Meeting, November 11, 2014, Rolla Missouri.
2. R. O'Malley and E. Nolte, PSMRC Meeting, May 19, 2015, Rolla Missouri.
3. R. O'Malley et al., "Influence of Mold Flux Crystalline Film Morphology and Film Stability on Mold Thermal Behavior," PSMRC Annual Report, Missouri S&T, 2015.
4. E. Nolte, PSMRC Meeting, December 2, 2015, Rolla Missouri.
5. E. Nolte, PSMRC Meeting, May 5, 2016, Rolla Missouri.
6. E. Nolte et al., "Influence of Mold Crystalline Film Morphology and Film Stability on Mold Thermal Behavior," PSMRC Annual Report, Missouri S&T, 2016.
7. E. Peterson, PSMRC Meeting, December 1, 2016, Rolla Missouri.
8. E. Peterson, PSMRC Meeting, May 4, 2017, Rolla Missouri.
9. E. Peterson et al., "Mold Flux Crystallization and Mold Thermal Behavior," PSMRC Annual Report, Missouri S&T, 2017.

BIBLIOGRAPHY

1. K.C. Mills, A.B. Fox, Z. Li, and R.P. Thackray, "The performance and properties of mould fluxes," *Ironmak. Steelmak.*, **32** [1] 26–34 (2005).

2. D.T. Stone and B.G. Thomas, "Measurement and modeling of heat transfer across interfacial mold flux layers," *Can. Metall. Q.*, **38** [5] 363–375 (1999).

3. A. Yamauchi, T. Emi, and S. Seetharaman, "A Mathematical Model for Prediction of Thickness of Mould Flux Film in Continuous Casting Mould.," *ISIJ Int.*, **42** [10] 1084–1093 (2002).

4. M. Degner, *Steel manual*, 1st ed. Verlag Stahleisen, Düsseldorf, 2008.

5. S. Seetharaman, A. McLean, R. Guthrie and S. Sridhar, *Treatise on process metallurgy*.

6. *Production routes for steel*, *sustainable in steel*, (2017).

7. A.K. Bhattacharya and D. Sambasivam, "Optimization of Oscillation Parameters in Continuous Casting Process of Steel Manufacturing: Genetic Algorithms versus Differential Evolution;" pp. 77–102 in *Evol. Comput.* 2009.

8. A. Cramb, *The making, shaping and treating of steel*. AISE, Pittsburgh, 2003.

9. S. Yamashita and M. Iguchi, "Mechanism of Mold Powder Entrapment Caused by Large Argon Bubble in Continuous Casting Mould," **41** [12] 1529–1531 (2001).

10. T. Kajitani, K. Okazawa, W. Yamada, and H. Yamamura, *Cold Model Experiment on Infiltration of Mould Flux in Continuous Casting of Steel: Simple Analysis Neglecting Mould Oscillation*, *ISIJ Int.*, **46** [2] 250–256 (2006).

11. N. Kasai and M. Iguchi, "Water-model Experiment on Melting Powder Trapping by Vortex in the Continuous Casting Mold," *ISIJ Int.*, **47** [7] 982–987 (2007).

12. H. Wang and W. Porter, *Thermal conductivity 27*, 1st ed. DEStech Pub., Lancaster, Pa., 2005.

13. X. Liu and M. Zhu, "Finite Element Analysis of Thermal and Mechanical Behavior in a Slab Continuous Casting Mold," *ISIJ Int.*, **46** [11] 1652–1659 (2006).

14. B.G. Thomas, G. Li, A. Moitra, and D. Habing, "Analysis of Thermal and Mechanical Behavior of Copper Molds during Continuous Casting of Steel Slabs;" pp. 1–19 in *80th Steelmak. Conf.* 1997.

15. J.K. Park, B.G. Thomas, I. V Samarasekera, and U.S. Yoon, "Thermal and mechanical behavior of copper molds during thin-slab casting (II): Mold crack formation," *Metall. Mater. Trans. B*, **33** [3] 437–449 (2002).

16. L.C. Hibbeler, B.G. Thomas, R.C. Schimmel, and G. Abbel, “The thermal distortion of a funnel mold,” *Metall. Mater. Trans. B Process Metall. Mater. Process. Sci.*, **43** [5] 1156–1172 (2012).

17. U.-S. Yoon, J.K. Park, B.G. Thomas, and I. Samarasekera, “MOLD CRACK FORMATION OF THE FUNNEL SHAPED MOLD DURING THIN SLAB CASTING;” pp. 245–257 in *85th Steelmak. Conf. Proceeedings*. 2002.

18. J.-W. Cho and H.-T. Jeong, “Infiltration of Slag Film into the Grooves on a Continuous Casting Mold;” pp. 1–9 in *Metec Insteel Con 2011*. 2011.

19. J. E. Shelby. *Introduction to glass science and technology*. Second Edition. Cambridge Royal Society of Chemistry, 2005.

20. W. Zachariasen, "THE ATOMIC ARRANGEMENT IN GLASS", *Journal of the American Chemical Society*, 54 [10] 3841-3851 (1932).

21. *Glass For Every Room In Your Home Or Office*, *Superiorglassconcord.blogspot.com*, (2017).

22. H. Kim and I. Sohn, “Effect of CaF2 and Li2O Additives on the Viscosity of CaO–SiO2 – Na2O Slags,” *ISIJ Int.*, **51** [1] 1–8 (2011).

23. J.H. Park, D.J. Min, and H.S. Song, “The Effect of CaF 2 on the Viscosities and Structures of CaO-SiO2(-MgO)-CaF2 Slags,” *Met. Mat. Trans. B*, **33B** [October] 723–729 (2002).

24. K.Y. Ko and J.H. Park, “Effect of CaF 2 Addition on the Viscosity and Structure of CaO – SiO 2 – MnO Slags,” *ISIJ Int.*, **53** [6] 958–965 (2013).

25. J.F. Stebbins and Z. Xu, “NMR evidence for excess non-bridging oxygen in an aluminosilicate glass,” *Nature*, **390** [November] 1996–1998 (1997).

26. Z. Wang, Q. Shu, and K. Chou, “Crystallization Kinetics and Structure of Mold Fluxes with SiO2 Being Substituted by TiO2 for Casting of Titanium-Stabilized Stainless Steel,” *Metall. Mater. Trans. B*, **44** [3] 606–613 (2013).

27. M. Persson, M. Görnerup, and S. Seetharaman, “Viscosity Measurements of Some Mould Flux Slags,” ISIJ Int., 47 [10] 1533–1540 (2007).

28. D.T. Mukongo and P.C. Pistorius, “Effects of Titanium Pick-up in Mould Fluxes for Stainless Steel;” pp. 675–682 in ISSTech 2003 Conf. Proc. 2003.

29. K.C. Mills, “Structure and Properties of Slags Used in the Continuous Casting of Steel : Part 1 Conventional Mould Powders,” ISIJ Int., 56 [1] 1–13 (2016).

30. H. Kim, W.H. Kim, J.H. Park, and D.J. Min, “A Study on the Effect of Na2O on the Viscosity for Ironmaking Slags,” Steel Res. Int., 81 [1] 17–24 (2010).

31. D. Wang, M. Jiang, C. Liu, P. Shi, Y. Yao, and H. Wang, Effects of rare earth oxide on viscosity of mold fluxes for continuous casting, J. Rare Earths, 23 [1] 68–72 (2005).

32. M. Hanao, "Influence of Basicity of Mold Flux on its Crystallization Rate," *ISIJ Int.*, **53** [4] 648–654 (2013).

33. D. Kalisz, "Modeling Physicochemical Properties of Mold Slag," *Arch. Metall. Mater.*, **59** [1] 149–155 (2014).

34. Y. Cui, L. Wang, J. Yang, J. Zhang, Y. Sasaki, and O. Ostrovski, "Phase Equilibria of Fluoride-Free Boracic Mould Flux for Steel Continuous Casting," Steel Res. Int., 86 [6] 662–669 (2015).

35. G.A. Bezuidenhout and P.C. Pistorius, "Alumina Pick-up and Mould Flux Crystallization;" pp. 369–376 in Steelmak. Conf. Proc. 2001.

36. Z. Chuan-yun, H. Wen-dian, L. Cheng-jun, and J. Mao-fa, "Crystallization Temperature and Crystallization Ratio of Mold Flux," J. Iron Steel Res., Int., 12 [6] 23–26 (2005).

37. T. Watanabe, H. Hashimoto, M. Hayashi, and K. Nagata, "Effect of Alkali Oxides on Crystallization in CaO – SiO 2 – CaF 2," 48 [7] 925–933 (2008).

38. H. Zhao, X. Wang, and J. Zhang, "Research on mold flux for hypo-peritectic steel at high casting speed," J. Univ. Sci. Technol. Beijing, 14 [3] 219–224 (2007).

39. Q. Shu, Z. Wang, J.L. Klug, K. Chou, and P.R. Scheller, "Effects of B2O3 and TiO2 on crystallization behavior of some slags in Al2O3-CaO-MgO-Na2O-SiO2 system," *Steel Res. Int.*, **84** [11] 1138–1145 (2013).

40. H. Nakada and K. Nagata, *Crystallization of CaO–SiO2–TiO2 Slag as a Candidate for Fluorine Free Mold Flux, ISIJ Int.*, **46** [3] 441–449 (2006).

41. J. Li, Q. Shu, X. Hou, and K. Chou, "Effect of TiO 2 Addition on Crystallization Characteristics of CaO- Al 2 O 3 -based Mould Fluxes for High Al Steel Casting," *ISIJ Int.*, **55** [4] 830–836 (2015).

42. D.T. Mukongo, "Effect of titanium pickup on mould flux viscosity in continuous slab casting;" 2003.

43. H. Shibata, M. Kondo, M. Suzuki, and T. Emi, "Thermal resistance between solidification steel shell and continuous casting mold with intervening flux film," *ISIJ Int.*, 36 179–182 (1996).

44. Y. Liu, W. Wang, F. Ma, and H. Zhang, “Study of Solidification and Heat Transfer Behavior of Mold Flux Through Mold Flux Heat Transfer Simulator Technique: Part I. Development of the Technique,” *Metall. Mater. Trans. B*, 46 [3] 1419–1430 (2015).

45. J.W. Cho, T. Emi, H. Shibata, and M. Suzuki, “Heat Transfer across Mold Flux Film in Mold during Initial Solidification in Continuous Casting of Steel.,” *ISIJ Int.*, 38 [8] 834–842 (1998).

46. J. Cho, H. Shibata, T. Emi, and M. Suzuki, “Thermal Resistance at the Interface between Mold Flux Film and Mold for Continuous Casting of Steels.,” *ISIJ Int.*, 38 [5] 440–446 (1998).

47. W. Wang and A.W. Cramb, “The observation of mold flux crystallization on radiative heat transfer,” *ISIJ Int.*, 45 [12] 1864–1870 (2005).

48. K. Gu, W. Wang, J. Wei, H. Matsuura, F. Tsukihashi, I. Sohn, and D.J. Min, “Heat-Transfer Phenomena Across Mold Flux by Using the Inferred Emitter Technique,” *Metall. Mater. Trans. B Process Metall. Mater. Process. Sci.*, 43 [December] 1–12 (2012).

49. G.H. Wen, P. Tang, B. Yang, and X.B. Zhu, “Simulation and Characterization on Heat Transfer through Mould Slag Film,” *ISIJ Int.*, 52 [7] 1179–1185 (2012).

50. G. Wen, S. Sridhar, P. Tang, X. Qi, and Y. Liu, “Development of Fluoride-free Mold Powders for Peritectic Steel Slab Casting,” *ISIJ Int.*, 47 [8] 1117–1125 (2007).

51. K.L.S. Assis and P.C. Pistorius, “Analyses of Phase Formation and Its Effect on the Thermal Resistance of Mold Flux;” pp. 1451–1459 in *AISTech Proc.* 2013.

52. A. Badri, T.T. Natarajan, C.C. Snyder, K.D. Powers, F.J. Mannion, and a. W. Cramb, “A mold simulator for the continuous casting of steel: Part I. The development of a simulator,” *Metall. Mater. Trans. B*, 36 [June] 355–371 (2005).

53. J. Diao, B. Xie, J. Xiao, and C. Ji, “Radiative Heat Transfer in Transition Metal Oxides contained in Mold Fluxes,” *ISIJ Int.*, 49 [11] 1710–1714 (2009).

54. J. Cho, H. Shibata, T. Emi, and M. Suzuki, “Radiative Heat Transfer through Mold Flux Film during Initial Solidification in Continuous Casting of Steel,” *ISIJ Int.*, 38 [3] 268–275 (1998).

55. H. Shibata, J. W. Cho, T. Emiand M. Suzuki: Proc. of the 5th Int. Conf. on Molten Slags, Fluxes and Salts. ISS, Sydney, (1997), 771.

56. M. Hayashi, R.A. Abas, and S. Seetharaman, “Effect of Crystallinity on Thermal Diffusivities of Mould Fluxes for the Continuous Casting of Steels,” *ISIJ Int.*, **44** [4] 691–697 (2004).

57. Y. Kang and K. Morita, “Thermal conductivity of the CaO-Al2O3-SiO2 system,” *ISIJ Int.*, **46** [3] 420–426 (2006).

58. M. Susa, M. Watanabe, S. Ozawa, and R. Endo, “Thermal conductivity of CaO-SiO2-Al2O3 glassy slags: Its dependence on molar ratios of Al2O3/CaO and SiO2/Al2O3,” *Ironmak. Steelmak.*, **34** [2] 124–130 (2007).

59. S. Ozawa and M. Susa, *Effect of Na2O additions on thermal conductivities of CaO–SiO2 slags, Ironmak. Steelmak.*, **32** [6] 487–493 (2005).

60. Y. Kashiwaya and K. Ishii, “Fundamental Analysis on the Heat Transfer of the Double Hot Thermocouple for the Measurement of Thermal Diffusivity of Molten Slag,” *ISSTech 2003 Conf. Proc.*, 1021–1030 (2003).

61. M. Susa, A. Kushimoto, H. Toyota, M. Hayashi, R. Endo, and Y. Kobayashi, “Effects of Both Crystallisation and Iron Oxides on the Radiative Heat Transfer in Mould Fluxes,” *ISIJ Int.*, **49** [11] 1722–1729 (2009).

62. W. Wang, K. Gu, L. Zhou, F. Ma, I. Sohn, D.J. Min, H. Matsuura, and F. Tsukihashi, “Radiative Heat Transfer Behavior of Mold Fluxes for Casting Low and Medium Carbon Steels,” *ISIJ Int.*, **51** [11] 1838–1845 (2011).

63. J. Shin, S.-H. Kim, B.G. Thomas, G.-G. Lee, J.-M. Park, and J. Sengupta, “Measurement and Prediction of Lubrication, Powder Consumption, and Oscillation Mark Profiles in Ultra-low Carbon Steel Slabs,” *ISIJ Int.*, **46** [11] 1635–1644 (2006).

64. W. Wang and A.W. Cramb, “The Effect of In-Situ Dynamic Mold Flux Crystallization on Radiative Heat Transfer,” *AIST Trans.*, **5** [1] 155–163 (2008).

65. S. Ozawa, M. Susa, T. Goto, R. Endo, and K.C. Mills, “Lattice and radiation conductivities for mould fluxes from the perspective of degree of crystallinity,” *ISIJ Int.*, **46** [3] 413–419 (2006).

66. J.W. Cho and H. Shibata, “Effect of solidification of mold fluxes on the heat transfer in casting mold,” *J. Non. Cryst. Solids*, **282** [1] 110–117 (2001).

67. S. Mineta, T. Kajitani, and H. Yamamura, “Experimental Study on Heat Transfer Behavior through the Mold Flux Film Between the Solidifying Shell and Mold;” pp. 71–80 in *AISTech 2010 Proc.* 2012.

68. A. Prasad and I. Bainbridge, “Experimental Determination of Heat Transfer Across the Metal/Mold Gap in a Direct Chill (DC) Casting Mold—Part I: Effect of Gap Size and Mold Gas Type,” *Metall. Mater. Trans. A*, **44** [1] 456–468 (2013).

69. J. Diao, X. Bing, W. Nanhui, H. Shengping, L. Yugang, and Q. Fei, *Effect of transition metal oxides on radiative heat transfer through mold flux film in continuous casting of steel*, *ISIJ Int.*, **47** [9] 1294–1299 (2007).

70. J.A. (Dries) Bothma, “Heat Transfer Through Mould Flux with Titanium Additions;” 2006.

71. R. Carli and C. Righi, “Mould flux crystallization : A kinetic study,” *VII Int. Conf. Molten Slags Fluxes Salts*, [Mm] 821–826 (2004).

72. A. Cruz, F. Chávez, A. Romero, E. Palacios, and V. Arredondo, “Mineralogical phases formed by flux glasses in continuous casting mould,” *J. Mater. Process. Technol.*, **182** [1–3] 358–362 (2007).

73. M. Dapiaggi, G. Artioli, C. Righi, and R. Carli, “High temperature reactions in mold flux slags: Kinetic versus composition control,” *J. Non. Cryst. Solids*, **353** [30–31] 2852–2860 (2007).

74. E. Divry, Y. Vermeulen, E. Paransky, and M. Rigaud, “Crystallization of Continuous Casting Mold Fluxes;” pp. 735–744 in *Electr. Furn. Conf. Proc.* 2002.

75. M. Hanao, M. Kawamoto, T. Murakami, and H. Kikuchi, “Mold flux for high speed continuous casting of hypoperitectic steel slabs,” *La Rev. Metall.*, 82–88 (2006).

76. P. Hooli and L. Holappa, “Layers in the Film Originating from the Casting Powder Between Steel Shell and Mould and Associated Phenomena in Continuous Casting of Stainless Steel;” in *ECCC 2008*. 2015.

77. M.D. Lanyi and C.J. Rosa, “Viscosity of casting fluxes used during continuous casting of steel,” *Metall. Trans. B*, **12** [2] 287–298 (1981).

78. J. Li, W. Wang, J. Wei, D. Huang, and H. Matsuura, “A Kinetic Study of the Effect of Na2O on the Crystallization Behavior of Mold Fluxes for Casting Medium Carbon Steel,” *ISIJ Int.*, **52** [12] 2220–2225 (2012).

79. K.C. Mills, L. Courtney, A.B. Fox, B. Harris, Z. Idoyaga, and M.J. Richardson, “The use of thermal analysis in the determination of the crystalline fraction of slag films,” *Thermochim. Acta*, **391** [1–2] 175–184 (2002).

80. H. Mizuno, H. Esaka, K. Shinozuka, and M. Tamura, “Analysis of the crystallization of mold flux for continuous casting of steel,” *Isij Int.*, **48** [3] 277–285 (2008).

81. M.D. Seo, C. Bin Shi, J.W. Cho, and S.H. Kim, “Crystallization Behaviors of CaO-SiO2-Al2O3-Na2O-CaF2-(Li2O-B2O3) Mold Fluxes,” *Metall. Mater. Trans. B Process Metall. Mater. Process. Sci.*, **45** [5] 1874–1886 (2014).

82. K.C. Mills, “Physical Properties of Casting Powders Part 2 Mineralogical consititution of slags formed by powders,” *Ironmak. Steelmak.*, **15** [4] 181–186 (1988).

83. M. Adachi, Y. Murakata, M. Hanao, Y. Tsukaguchi, and M. Kawamoto, "Development of Anti- Entrapment Mold Flux with Melilite Crystal for Round Billet Caster;" pp. 1599–1607 in *AISTech 2011 Proc.* 2011.

84. N. Saito, K. Kusada, S. Sukenaga, Y. Ohta, and K. Nakashima, "Effect of Agitation on Crystallization Behavior of CaO – SiO 2 – R 2 O (R = Li , Na , or K) System Characterized by Electrical Capacitance Measurement," *ISIJ Int.*, **52** [12] 2123–2129 (2012).

85. C. Orrling, S. Sridhar, and a. W. Cramb, "In situ Observations and Thermal Analysis of Crystallization Phenomena in Mold Slags," *High Temp. Mater. Process.*, **20** [3–4] (2001).

86. J. Cho, K. Blazek, M. Frazee, H. Yin, and J.H. Park, "Assessment of CaO–Al2O3 Based Mold Flux System for High Aluminum TRIP Casting," *ISIJ Int.*, **53** [1] 62–70 (2013).

87. K. Blazek, H. Yin, G. Skoczylas, M. McClymonds, and M. Frazee, "Evaluation of Lime-Silica and Lime-Alumina Mold Powders Developed for Casting High Aluminum TRIP Steel Grades;" pp. 1–10 in *Metec Insteel Con 2011*. 2011.

88. B. Lu, K. Chen, W. Wang, and B. Jiang, "Effects of Li2O and Na2O on the Crystallization Behavior of Lime-Alumina-Based Mold Flux for Casting High-Al Steels," *Metall. Mater. Trans. B*, **45** [4] 1496–1509 (2014).

89. D. Xiao, W. Wang, and B. Lu, "Effects of B2O3 and BaO on the Crystallization Behavior of CaO-Al2O3-Based Mold Flux for Casting High-Al Steels," *Metall. Mater. Trans. B*, **46** [2] 873–881 (2015).

90. W. Yan, W. Chen, Y. Yang, C. Lippold, and A. Mclean, "Effect of Slag Compositions and Additive on Heat Transfer and Crystallization of Mold Fluxes for High-Al Non-magnetic Steel," *ISIJ Int.*, **55** [5] 1000–1009 (2015).

91. J. Li, Q. Shu, X. Hou, and K. Chou, "Effect of TiO 2 Addition on Crystallization Characteristics of CaO- Al 2 O 3 -based Mould Fluxes for High Al Steel Casting," *ISIJ Int.*, **55** [4] 830–836 (2015).

92. H. Zhao, W. Wang, L. Zhou, B. Lu, and Y.B. Kang, "Effects of MnO on Crystallization, Melting, and Heat Transfer of CaO-Al2O3-Based Mold Flux Used for High Al-TRIP Steel Casting," *Metall. Mater. Trans. B*, **45** [4] 1510–1519 (2014).

93. K. Blazek, H. Yin, G. Skoczylas, M. McClymonds, and M. Frazee, "Evaluation of Lime-Silica and Lime-Alumina Mold Powders Developed for Casting High Aluminum TRIP Steel Grades;" pp. 1–10 in *Metec Insteel Con 2011*. 2011.

94. J. Cho, K. Blazek, M. Frazee, H. Yin, and J.H. Park, “Assessment of CaO–Al2O3 Based Mold Flux System for High Aluminum TRIP Casting,” *ISIJ Int.*, **53** [1] 62–70 (2013).

95. C.-B. Shi, M.-D. Seo, J.-W. Cho, and S.-H. Kim, “Crystallization Characteristics of CaO-Al2O3 -Based Mold Flux and Their Effects on In-Mold Performance during High-Aluminum TRIP Steels Continuous Casting,” *Metall. Mater. Trans. B*, **45B** [June] 1081–1097 (2014).

96. K. Jackson, *Kinetic processes*, 1st ed. Wiley-VCH, Weinheim, 2010.

97. E.D. Zanotto and P.F. James, “Experimental tests of the classical nucleation theory for glasses,” *J. Non. Cryst. Solids*, **74** [2–3] 373–394 (1985).

98. K.A. Jackson, D.R. Uhlmann, and J.D. Hunt, “On the nature of crystal growth from the melt,” *J. Cryst. Growth*, **1** 1–36 (1967).

99. I. Gutzow, “The mechanism of crystal growth in glass forming systems,” *J. Cryst. Growth*, **42** 15–23 (1977).

100. H. Ray, *Kinetics of metallurgical reactions*, 1st ed. International Science Publisher, New York, 1993.

101. G.H. WEN, H. LIU, and P. TANG, “CCT and TTT Diagrams to Characterize Crystallization Behavior of Mold Fluxes,” *J. Iron Steel Res. Int.*, **15** [4] 32–37 (2008).

102. N. Saunders, Z. Guo, a P. Miodownik, and J.-P. Schillé, “The Calculation of TTT and CCT diagrams for General Steels,” 1–12 (2004).

103. E.S. Watson and M.J. O’Neill, “Differential microcalorimeter,” *US Pat. 3,263,484*, 3–12 (1962).

104. Prapakorn, S. Seetharaman, and A.W. Cramb, “A Comparison of Different Techniques for Determining the Crystallization Temperature of Slags,” *Steelmak. Conf. Proc.*, 357–368 (2001).

105. H. Sakai, T. Kawashima, K. Shiomi, K. Watanabe, and T. Iida, “Crystallization behavior of molten fluxes for high-speed continuous casting of middle-carbon steel;” pp. 787–790 in *5th Int. Conf. Molten Slags, Fluxes Salts*. 1997.

106. A. Prasad and H. Henein, “CCT Diagrams for Mold Flux Crystallization Studies,” *ISSTech 2003 Conf. Proc.*, 257–262 (2003).

107. Y.G. Maldonado, F.A. Acosta, A.H. Castillejos, and B.G. Thomas, “Kinetic Study of the Devitrification of Mold Powder Slags,” *AISTech*, 11 (2012).

108. H- Y. Meng, B.G. Thomas, a. a. Polycarpou, a. Prasad, and H. Henein, “Mould Slag Property Measurements To Characterize Cc Mould – Shell Gap Phenomena,” *Can. Metall. Q.*, **45** [1] 79–94 (2006).

109. Y.G. Maldonado, C. Barraza de la P, S. Rodríguez A, A.H. Castillejos E, and B.G. Thomas, “Estimation of Time–Temperature-Transformation Diagrams of Mold Powder Slags from Thermo-analysis of Non-isothermal Crystallization,” *Metall. Mater. Trans. B Process Metall. Mater. Process. Sci.*, **46** [1] 286–303 (2014).

110. Y. Kashiwaya, C.E. Cicutti, A.W. Cramb, and K. Ishii, “Development of Double and Single Hot Thermocouple Technique for in Situ Observation and Measurement of Mold Slag Crystallization.,” *ISIJ Int.*, **38** [4] 348–356 (1998).

111. B. Jiang, W. Wang, I. Sohn, J. Wei, L. Zhou, and B. Lu, “A Kinetic Study of the Effect of ZrO2 and CaO/Al2O3 Ratios on the Crystallization Behavior of a CaO-Al2O3-Based Slag System,” *Metall. Mater. Trans. B*, **45** [June] (2014).

112. H. Liu, G. Wen, and P. Tang, “Crystallization Behaviors of Mold Fluxes Containing Li 2 O Using Single Hot Thermocouple Technique,” *ISIJ Int.*, **49** [6] 843–850 (2009).

113. L. Zhou, W. Wang, F. Ma, J. Li, J. Wei, H. Matsuura, and F. Tsukihashi, “A kinetic study of the effect of basicity on the mold fluxes crystallization,” *Metall. Mater. Trans. B Process Metall. Mater. Process. Sci.*, **43** [2] 354–362 (2012).

114. Y. Kashiwaya, C.E. Cicutti, and A.W. Cramb, “An Investigation of the Crystallization of a Continuous Casting Mold Slag Using the Single Hot Thermocouple Technique.,” *ISIJ Int.*, **38** [4] 357–365 (1998).

115. C.T. Mutale, T. Claudon, and A.W. Cramb, “Observation of the Crystallization Behavior of a Slag Containing 46 Wt Pct CaO, 46 Wt Pct SiO2, 6 Wt Pct Al2O3, and 2 Wt Pct Na2O Using Double Hot Thermocouple Technique,” *Metall. Mater. Trans. B*, **36B** [June] 417–419 (2005).

116. L. Zhou, W. Wang, D. Huang, J. Wei, and J. Li, “In situ observation and investigation of mold flux crystallization by using double hot thermocouple technology,” *Metall. Mater. Trans. B Process Metall. Mater. Process. Sci.*, **43** [4] 925–936 (2012).

117. H.G. Ryu, Z.T. Zhang, J.W. Cho, G.H. Wen, and S. Sridhar, “Crystallization Behaviors of Slags through a Heat Flux Simulator,” *ISIJ Int.*, **50** [8] 1142–1150 (2010).

118. J.-Y. Park, J.W. Ryu, and I. Sohn, “In-situ Crystallization of Highly Volatile Commercial Mold Flux Using an Isolated Observation System in the Confocal Laser Scanning Microscope,” *Metall. Mater. Trans. B*, **45** [4] 1186–1191 (2014).

119. Z. Li, R. Thackray, and K.C. Mills, “A test to determine crystallinity of mould fluxes,” *VII Int. Conf. Molten Slags Fluxes Salts*, 813–820 (2004).

120. Y. LEI, B. XIE, and W. MA, “Analysis of Crystallization Behavior of Mold Fluxes Containing TiO2 Using Single Hot Thermocouple Technique,” *J. Iron Steel Res. Int.*, **23** [4] 322–328 (2016).

121. Yacobi and D. Holt, *Cathodoluminescence microscopy of inorganic solids*, 1st ed. Plenum Press, New York, 1990.

122. J. D. Smith, K. D. Peaslee, M. Karakus, and L. Trueba Jr., "Study of Continuous Casting Nozzle Clogging using Cathodoluminescence Microscopy," Advances in Refractories for the Metallurgical Industries III, (ed. C. Allaire and M. Rigaud), CIM, Montreal, Quebec, Canada, 1999, pp. 187-200.

123. H-M. Karakus and R.E. Moore, “Cathodoluminescence (CL) Microscopy Application to Refractories and Slags,” *J. Miner. Mater. Charact. Eng.*, **1** [1] 11–29 (2002).

124. B- H. Yin and H.T. Tsai, "Application of Cathodoluminescence Microscopy (CLM) in Steel Research," in ISSTech2003 Conference Proceedings, ISS, Warrandale, PA, 2003, 217-226.

125. M. Karakus, J.D. Smith and K.D. Peaslee,"Study of Non-Metallic Inclusions in Continuously Cast Steel Using Cathodoluminescence Microscopy," Proc. of the 38th Annual Meeting of the St. Louis Section of the American Ceramic Society, Chesterfield, MO, March 22, 2002.

126. D-A. Kumar, V. Thapliyal, and J. Smith. (2014), Interaction of BN-ZrO_2-SiC Ceramics with Inclusions in Si-killed Steel. Int. J. Appl. Ceram. Technol., 11: 1001–1011.

127. E. Paransky, E. Divry, and M. Rigaud, “Application of Cathodoluminescence Technique in Light Microscopy to Crystallisation Study of Mold Fluxes,” *Micros. Miroanal.*, [Suppl. 2] (2002).

128. B. Cullity, *Elements of X-ray diffraction*, 2nd ed. Addison-Wesley Publishing Company, 1978.

129. L. Alexander and H.P. Klug, “Basic Aspects of X-ray Absorption in Quantitative Diffraction Analysis of Powder Mixtures,” *Anal. Chem.*, **20** [10] 886–889 (1948).

130. H.M. Rietveld, “A profile refinement method for nuclear and magnetic structures,” *J. Appl. Crystallogr.*, **2** [2] 65–71 (1969).

131. R. Young, *The Reitveld Method*, 1st ed. Oxford University Press, New York, 1995.

VITA

Elizabeth Irene Peterson, nèe Nolte, was born in Elmhurst, Illinois. In August 2011 Elizabeth started her undergraduate degree in ceramic engineering at Missouri University of Science and Technology. During her undergraduate career, Elizabeth was an active member of Material Advantage and Keramos. Elizabeth worked at Georgia Tech as a part of the SURF program in the MSE department, Watlow Electric as an engineering co-op, and at Argonne National Laboratory as a part of the SULI program sponsored by the Department of Energy. Elizabeth was also active in department outreach, spending many afternoons providing department demonstrations to prospective students. Knowing she wanted to continue her education, Elizabeth spent her last semester taking both graduate and undergraduate courses at Missouri S&T. She completed her B.S. degree in Ceramic Engineering from Missouri S&T in May 2015.

Elizabeth began her graduate work at Missouri S&T May 2015 as a Masters Student in Materials Science and Engineering. She was fortunate enough to continue her senior design project and have funding for her research from the Peaslee Steel Manufacturing Research Center (PSMRC). Her research was focused on mold fluxes for continuous casting steel, a bridge between both metallurgy and ceramics. Elizabeth had the opportunity to work with many colleagues in the steel industry, and was able to travel to several plants for sampling. During her time as a Masters student, Elizabeth had the opportunity to work with many undergraduate students through her research and through assisting with Mud Lab (Ceramic Materials Lab I). Elizabeth earned her M.S. degree in Materials Science and Engineering in May 2017 from Missouri University of Science and Technology.